Novel Applications of Static Micro-Scale Interdigitated Electrodes for Energy Harvesting and Biosensing

Duc Hau HUYNH

Submitted in partial fulfillment of the requirements of the degree of

Doctor Of Philosophy

Department of Electrical and Electronic Engineering

School of Engineering

THE UNIVERSITY OF MELBOURNE

March 2017

THE UNIVERSITY OF MELBOURNE

Abstract

Department of Electrical and Electronic Engineering
School of Engineering

Doctor of Philosophy

Novel Applications of Static Micro-Scale Interdigitated Electrodes for Energy Harvesting and Biosensing

by Duc Hau HUYNH

Microsystems or Micro-electromechanical Systems (MEMS) refer to the integration of sensors, actuators and signal-processing electronics on the single unit. Today microsystems technology has grown rapidly due to its advantages compared to the macro scale counterparts. In 2015, the total market for commercial microsystems products has reached US$10 billion and has been forecasted to keep growing. This thesis investigates microsystems for energy harvesting and biological sensing applications.

Interdigital electrode (IDE) capacitor is one of the most widely used structures for both sensing and actuation. In this thesis, it is applied to both biosensing and energy harvesting applications. To optimize the design and fabrication of these devices, the thesis investigates various analytical models of the IDE capacitor structure. Understanding the effect of different parameters of this structure is critical in the design and optimization of the system. The designs are then verified with a commercial microsystems design and simulation tool (CoventorWare). Simulations were carried out for both microscale IDE capacitor structures, which are used for energy harvesting, and nanoscale IDE capacitor structures, which are used for biological sensing.

The thesis contributes advances to microsystems based energy harvesting and biological sensing. In the case of microsystems applied to energy harvesting, a new type of device is proposed. An electrostatic power generator converts mechanical energy to electrical energy by utilizing the principle of variable capacitance. This change in capacitance is usually achieved by varying the gap or the overlap between two parallel metallic plates. This thesis proposes a novel electrostatic micro power generator where the change in capacitance is achieved by the movement of an aqueous solution of NaCl. A significant change in capacitance is achieved due to the higher than air dielectric constant of water and the Helmholtz double layer capacitor formed by ion separation at the electrode interfaces. The proposed device has significant advantages over traditional electrostatic devices which include low bias voltage and low mechanical frequency of operation. This is critical if the proposed device is applied to harvest energy from the environment. A figure of merit exceeding 10000 $\frac{10^8 \mu W}{(mm^2 HzV^2)}$, which is two orders of magnitude greater than previous reported devices, is demonstrated for a prototype operating at a bias voltage of only 1.2 V and a droplet frequency of 6 Hz.

The second contribution of this thesis is in the area of new microsystems based biological sensing. Specifically, this work demonstrates the detection of antigen/antibody. A nanoscale sensing device is implemented to detect glial fibrillary acidic protein (GFAP) antibody for early detection and monitoring of brain tumour. Glioma is the most common primary brain tumour with its early detection remaining a challenge. Autoantibodies against GFAP have shown the highest differential expression compared with the other glioma expressed autoantibodies. Here a prototype of immunosensor to detect GFAP antibody levels is developed using an interdigital coplanar waveguide (ID-CPW). The ID-CPW is fabricated on a SiO_2/Si substrate with the CPW and interdigital electrode conducting layers made using Cr/Au. The sensor is functionalized, and protein extracted from astrocytes is immobilized on the surface. Sensitivity and dynamic range are ascertained using varying the concentrations of a commercial, polyclonal antibody to GFAP. The electrical detection of antigen-antibody binding is performed in both dry and wet environments across the 1–25 GHz range. The results show that the proposed sensor can detect antibodies against GFAP to a minimum concentration of 2.9 picograms per milliliter with a turnaround time of less than 3 hours. The electrical measurements indicate an improved sensitivity compared with the state-of-the-art optical detection methods. The proposed sensor, developed to detect antibody against GFAP, is the first to show the applicability in the detection of glioma using the GFAP antibodies.

Declaration

This is to certify that:

i. the thesis comprises only my original work towards the PhD except where indicated in the Preface,

ii. due acknowledgement has been made in the text to all other materials used,

iii. the thesis is fewer than 100 000 words in length, exclusive of tables, maps, bibliographies and appendices.

Signed:

Duc Hau HUYNH.

Date:

Learn from yesterday, live for today, hope for tomorrow. The important thing is not to stop questioning.

Albert Einstein

Acknowledgements

First and foremost, I would like to express my special appreciation and thanks to my supervisor, Professor Stan Skafidas, for his tremendous supports during the past 4 years of my PhD life. Without his supports and guidance, the completion of this thesis would not be possible. He always inspires me with many new ideas and has always been patient with me when thing goes wrong. I have seen from one of his former PhD student's thesis this statement, "Professor Skafidas is the one supervisor that every PhD student dreams of.", and I am 200% agree with it.

I also would like to thank Professor Rob Evans for being my co-supervisor and my review committee member. He gave me encouragements and many valuable advices during our review meetings. I also would like to express my gratitude to Professor Thas Nirmalathas, who is the chair of my PhD review committee. In every review meeting, he always ensures that I was on track with the timeline of my PhD work.

I would like to thank the Australian Government, the University of Melbourne and the National ICT Australia (NICTA) for supporting my research with an Australian Postgraduate Awards (APA) full scholarship and a NICTA top up scholarship.

I also would like to thank NICTA, the Centre for Neural Engineering (CfNE) and the Department of Electrical and Electronic Engineering for providing me a supportive academic environment that is well equipped with many valuable equipment and facilities to carry out my research.

I would like to thanks Melbourne Centre for Nanofabrication (MCN) for providing me with the state-of-the-art nanofabrication facilities. I also highly appreciate the training and generous supports from the engineers and instrument managers at MCN (Dr. Douglas Mair, Dr. Matteo Altissimo, Dr. Sean Langelier, Dr. Yang Lim, Dr. Lachlan Hyde, Dr. Ricky Tjeung, Dr. Fatima Eftekhari and Mr. Dan Smith. My very special thanks to Mr. Dan Smith, who has given me very useful advices in various fabrication processes that I have developed.

I would like to thank Dr. Thanh Nguyen, Dr. Phuong Nguyen and Dr. Chathurika Abeyrathne, who I have been working with very closely. They have been giving me unlimited supports and advices from the very first day of my PhD to the very last day when I am writing up this thesis. I also would like to thank my friend, Mr. Peter Devlin, for his company during the stressful but very exciting time of our PhD life.

These acknowledgements would not be complete without mentioning other former and current colleagues at the CfNE, who I have been collaborating with in many different

projects: Dr. David Ng, Dr. Gordana Felic, Dr. Faruque Hossain, Dr. Feras Al-Dirini, Mr. Sharafat Hossain, Mr. Liming Jiang, Ms. Ting Ting Lee, Dr. Babak Nasr and Dr. Gursh Chana. It was a great pleasure working with them and I appreciate their ideas and supports.

I also would like to thank the team of “senior friends” at CfNE, Dr. Anh Trong Huynh, Dr. Nhan Tran, Dr. Hoa Thai Duong, Dr. Chien Minh Ta, Dr Hoang Viet Le, for providing many useful advices that guided me through PhD work. Most importantly, they helped me to improve my “coffee appreciation” skill.

I sincerely thank Professor John Devlin at Engineering Department, La Trobe University. Without him, I would not have the opportunity to do an engineering degree and of course will not be able to complete this PhD.

Lastly, I thank my parents, my wife and my little son for always giving me unconditional support. They do not know or understand what I am doing, but always proud of what I have done.

Preface

This thesis presents the works that I carried out during my PhD candidature in the Department of Electrical and Electronic Engineering, School of Engineering, The University of Melbourne.

Majority of device fabrication works in this thesis were performed at the Melbourne Centre for Nanofabrication (MCN) in the Victorian Node of the Australian National Fabrication Facility (ANFF). Major tools used for device fabrication at MCN include the Electron Beam Lithography (EBL) Vistec EBPG5000PlusES, The DRIE Etching System Oxford Plasmalab System 100, the E-beam Evaporator Intlvac Nanochrome II, the FEG-SEM Nova NanoSEM 430, The Fiji F200 Atomic Layer Deposition (ALD) system, the Oxford Plasma Lab100, the ABM UV Flood Light Source and the Wedge Bonder-Kulicke & Soffa Model 4526.

Part of the fabrication works were carried at the Electrical and Electronic Engineering Department, School of Engineering, The University of Melbourne. The equipment used at this Department is the SUSS SLP300 laser ablation system.

The electrical characterizations of devices were performed at the TRL lab of the Electrical and Electronic Engineering Department, School of Engineering, The University of Melbourne. The equipments used include the Anritsu ME7808B Vector Network Analyzer (VNA) and the Agilent E5270B Precision Mainframe.

The biological sample preparation, processing and characterization were carried out at the PC2 Lab of the Centre for Neural Engineering, The University of Melbourne.

The work in chapter 5 was prepared from my publication: Huynh, D.H., Nguyen, T.C., Nguyen, P.D., Abeyrathne, C.D., Hossain, M.S., Evans, R. and Skafidas, E., 2016. Environmentally friendly power generator based on moving liquid dielectric and double layer effect. *Scientific Reports*, 6, p.26708.

The work in chapter 6 was done in collaboration with Dr. C.D Abeyrathne and prepared from our publication: Abeyrathne, C.D., Huynh, D.H., Lee, T.T., Nguyen, T.C., Nasr, B., Chana, G. and Skafidas, E., 2016. GFAP Antibody Detection Using Interdigital Coplanar Waveguide Immunosensor. *IEEE Sensors Journal*, 16(9), pp.2898-2905.

Contents

List of Figures

List of Tables

Abbreviations

1D	**One** **D**imensional
2D	**Two** **D**imensional
3D	**Three** **D**imensional
AFM	**A**tomic **F**orce **M**icroscopy
CMOS	**C**omplementary **M**etal **O**xide **S**emiconductor
CVD	**C**hemical **V**apour **D**eposition
DI	**D**e**I**onized
DNA	**D**eoxyribo**N**ucleic **A**cid
EBL	**E**lectron-**B**eam **L**ithography
ELISA	**E**nzyme-**L**inked **I**mmuno**S**orbent **A**ssay
EMPG	**E**lectrostatic **M**icro **P**ower **G**enerator
FEM	**F**inite **E**lement **M**ethod
FOM	**F**igure **O**f **M**erit
GFAP	**G**lial **F**ibrillary **A**cidic **P**rotein
HF	**H**ydro**F**luoric
HSQ	**H**ydrogen **S**ilses**q**uioxane
IC	**I**ntegrated **C**ircuit
IDE	**I**nterDigital **E**lectrode
ID-CPW	**I**nter**D**igital **C**o**P**lanar **W**aveguide
IPA	**I**so**P**ropyl **A**lcohol
MEMS	**M**icro-**E**lectro-**M**echanical **S**ystems
PDMS	**P**oly**dim**ethyl**s**iloxane
PECVD	**P**lasma **E**nhance **C**hemical **V**apour **D**eposition
PBS	**P**hosphate-**B**uffered **S**aline
PMMA	**P**oly(**m**ethyl **m**eth**a**crylate)

RF	**R**adio **F**requency
SEM	**S**canning **E**lectron **M**icrocscopy
SOLT	**S**hort **O**pen **L**oad **T**hrough
VLSI	**V**ery **L**arge **S**cale **I**ntegration
VNA	**V**ector **N**etwork **A**nalyzer

Dedicated to my family.

Chapter 1

Introduction

1.1 Motivation

Microsystems or micro-electromechanical Systems (MEMS) refer to the integration of sensors, actuators and signal-processing electronics into a single package. The history of microsystems technology can be traced back to the early days of integrated circuit (IC) development. Many fundamental fabrication methods used in microsystems technology are primarily adopted from the IC fabrication processes which involves some forms of lithography and specialized techniques referred to as micromachining. The materials used to fabricate these systems are constrained by microfabrication techniques. Most materials used today are conventional inorganic substance used in IC industry such as silicon, silicon dioxide, silicon nitride, aluminum, tungsten etc. Recently, polymers are also used for several applications of microsystems in the area of biological sensing [10].

In comparison to their macro scale counterparts, microsystems based devices offer many advantages. Firstly, a large amount of microsystems devices can be fabricated easily in the same run using very large scale integration(VLSI) technology, which is adopted from IC industry. Currently, up to thousands of microsystems devices can be produced on a single silicon wafer. Hence, the production cost of microsystems devices could be reduced significantly compared to their macro size counterparts. In addition, the modification and alteration of the design and fabrication of microsystems devices can be carried out quickly and easily with low cost. For macro scale device production, redesigning or modifying a part may involve the whole production line modification; which could require the shutdown of the entire production plant. On the other hand, modification of a microsystems device may only require an adjustment of a single mask, or a few parameters of fabrication process. Another key advantage of microsystems based device is its low power consumption and small form factor in comparison to the traditional devices. Macro scale devices are big and bulky and require high power to operate; on the other hand, microsystems devices consume very low power. In addition, due to their small size and IC fabrication compatibility, microsystems devices can be integrated with the necessary electronic circuitry to lower the production cost of final system as well as to reduce the overall form factor.

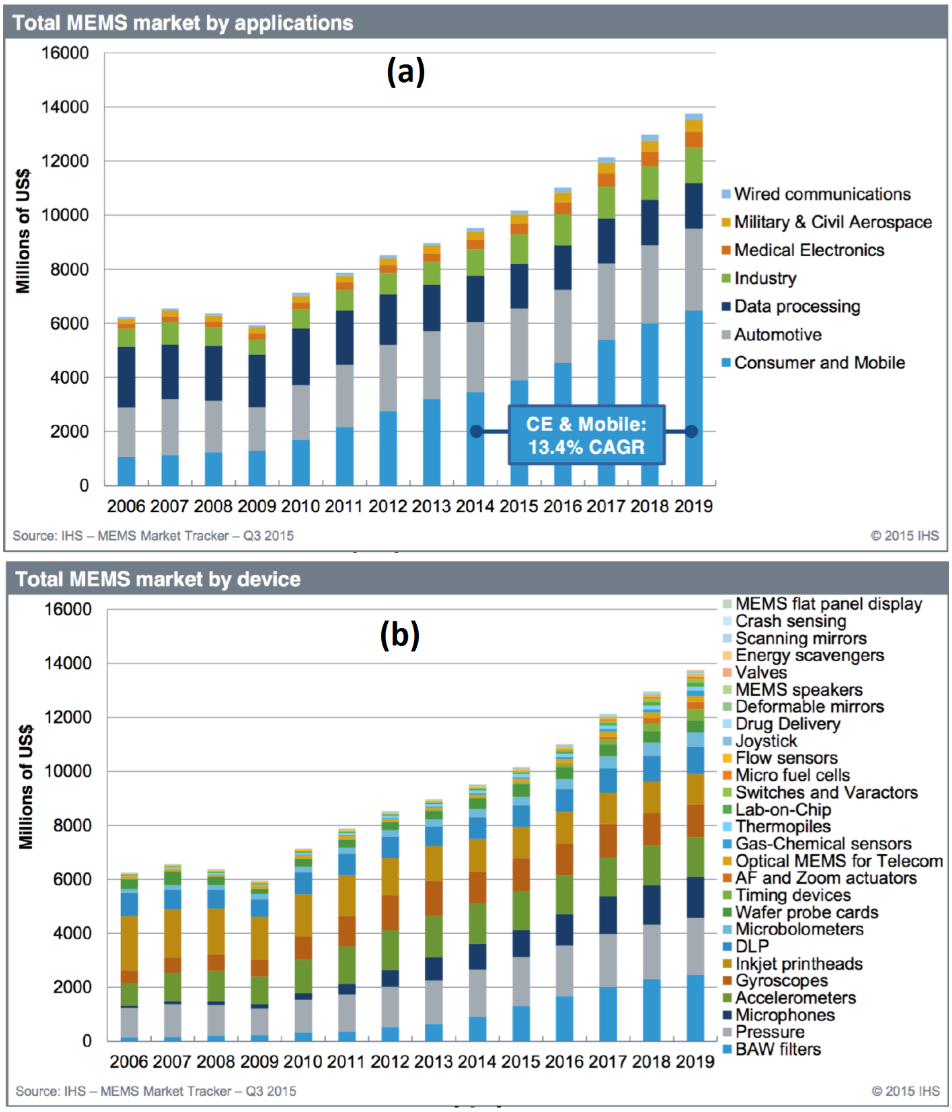

FIGURE 1.1: Microsystems market projection by IHS Inc., (a) market projection by application and (b) market projection by device types. Copied from [1].

Since the very first demonstration of microsystems device in the late-60s (MOS-photodiode arrays for visible imaging) [10] there has been a significant growth in both academic research and commercial development of microsystems devices worldwide. Today, the application of microsystems devices are ubiquitous, ranging from wired and wireless communication, military and civil aerospace, medical electronics, industry, data processing, automotive and consumer electronic and mobile devices. Figure 1.1 illustrates the market of microsystems by application (a) and by device type (b) conducted by IHS Inc. In 2015, the microsystems market has reached the total of US$10 billion and is predicted to grow up to US$14 billion in the next 4 years [1].

This thesis investigates the current fabrication process of microsystems devices and further utilizes them in energy harvesting and biological sensing applications.

Application of microsystems in energy harvesting application

Today, wireless sensor devices, bio-implants or microscale biosensor devices can operate with very low power consumption, in microwatts. However, for many of these applications, it is not suitable to have power source that comes from battery or external supplier. This challenge has prompted a significant amount of research into the development of micro-scale power generators that can autonomously convert various forms of ambient energy to electrical energy to produce self powering devices. Among various ambient energy sources such as mechanical, thermal, radiant, and biochemical, mechanical energy due to stress/strain or vibration is one of the most widely available sources. The causes for this vibration or stress/strain are ubiquitous. It can be due to wind, sea water wave, body movement, engine vibration, blood flow, heartbeat, respiration and air-conditioning etc [2].

So far, to convert mechanical energy to electrical energy, there are three popular transducer methods being used, namely piezoelectric, electromagnetic, and electrostatic. Piezoelectric is the most widely used technique due to the simplicity of device fabrication and the required control circuitry. This method does not usually require any external power sources to operate. These devices exploit piezoelectric property of materials to generate charge under stress or strain. However, piezoelectric materials can be rare and expensive to synthesis. Electromagnetic power generators are based on electromagnetic induction. They are widely used at the macro scale. At micro scale electromagnetic transducer devices are difficult to fabricate and integrate. Moreover, the magnetic materials required for device fabrication are expensive. In addition, the efficiency of electromagnetic transducer device is frequency dependent. They are less efficient at low frequency where most of the mechanical energy sources are available [2].

An electrostatic micro power generators (EMPG) operate based on the principle of variable capacitor. The materials used to fabricate these devices are conventional materials which are widely used in complementary metal-oxide-semiconductor (CMOS) process such as Si and standard metals. In addition, the fabrication steps to produce this type of device are simple and based on standard microfabrication processes. Therefore this type of device has a great potential to be integrated into current low cost CMOS devices.

However, there are still several drawbacks that hinder researchers to widely adopt EMPG devices. Since the first demonstration by Meninger et al. in 2001 [11], there has not been much progress in the development of this type of device. By far, most of the demonstrated prototypes utilize some forms of parallel plate capacitor with moving metal electrodes. The capacitance change is achieved by changing the gap between the electrodes. This change in gap is limited due to the nature of the solid electrodes used to construct the devices. Hence it usually results in small capacitance change. To achieve both high power output and efficiency, this type of device has to operate at very high vibrational frequency, up to kilohertz and requires high bias voltages, into thousands of volts. In addition, such device can only be designed to operate at a specific vibration frequency, which is the natural resonant frequency of the solid electrodes.

The first part of this thesis addresses these drawbacks by introducing a novel design for electrostatic micro power generator. In the proposed design, the change in capacitance is obtained by utilizing the movement of a liquid ionic solution (NaCl solution). A significant change in capacitance is achieved due to the high dielectric constant of water and the Helmholtz double layer capacitor formed by ion separation at the electrode interfaces. The proposed device has significant advantages over traditional electrostatic devices which include low bias voltage and low mechanical frequency of operation. This is critical if the proposed device is used in harvesting energy from the environment. A figure of merit exceeding 10000 $\frac{10^8 \mu W}{(mm^2 Hz V^2)}$, which is two orders of magnitude greater than previous devices, is demonstrated for a prototype operating at a bias voltage of 1.2 V and a droplet frequency of 6 Hz.

Application of microsystems in biological sensing

The second part of this thesis investigates a special class of microsystems devices used in biological application, which is referred as BioMEMS. Currently, the application of microsystems in this field is growing rapidly due to multiple advantages that microsystems technology has to offer. Firstly, microsystems technology has enabled multiple medical platforms to handle very small volume of biological sample, which can be in the microliters range. Secondly, due to the high level of integration of microsystems, sample preparation units (such as mixer, heater and micro-pump etc.), microfluidic components and sensing system can be included in a single unit. Hence, the overall cost to perform an analysis can be reduced significantly. In addition, microsystems devices have surpassed the traditional testing methods in terms of sensitivity, specificity and testing time [12]. For this reason, microsystems has been demonstrated in various biological applications, including miniaturized biosensors [13–16], diagnostics [17–19], tissue engineering [20–24], medical implants and surgery [25, 25–30].

This thesis focuses on the application of a particular microsystem – an IDE structure based biosensor – for molecular diagnostics of a specific biomarker. Generally, a biosensor can be defined as a device that consists of a biological recognition system and a transducer [3]. The biological recognition system is referred as bioreceptor. This bioreceptor is selected to be match with a specific analyte of interest. The interaction between the bioreceptor and the analyte causes an effect that can be picked up by a transducer method. Typical bioreceptors are antibody, enzyme, protein, nucleic acid or living cell [3]. In term of transduced technique, popular methods include optical detection, electrochemical detection, mass-sensitive detection, and impedance detection.

In this thesis, an impedance based detection method is chosen to implement a nanoscale biosensor that is used to assist in the early detection of brain tumours. The most common primary brain tumour is the glioma which arises from glial cell. Currently, imaging-based methods are widely used for detection of glioma [31]. However, these methods are time-consuming, costly and not suitable for large scale screening to support early stage detection or for management of patients receiving treatment. Hence an alternative method which can offer a low cost, easy-to-use and fast response testing is indispensable. Recent research [32–34] has shown that glial fibrillary acidic protein (GFAP) has been widely detected in glioma patients and GFAP antibody is a good candidate of biomarker for early detection. Therefore, GFAP antibody is employed as a bioreceptor for GFAP. In this application, since both the receptor and the analyte are in nanoscale dimension, the geometric structure chosen is a nanoscale interdigital coplanar waveguide (ID-CPW) with both electrodes width and gap to be in nanometre range. The advantages of planar ID-CPW structure compared to other techniques are its simplicity of fabrication process and the ability to be integrated into a single system with low manufacturing cost. In addition, this method has been proven to be outperformed others in term of sensitivity [35]. The prototype device proposed in this thesis, when measured using vector network analyser (VNA) probe station, can detect antibodies to GFAP to a minimum concentration of 2.9 pg/mL. This result shows an improvement in sensitivity compared to other state of art optical detection methods. The technique proposed in this study also provides the possibility of an integrated on-chip system for GFAP antibody or any similar bioreceptors.

1.2 Thesis organization

This thesis is organized into 7 chapters.

Chapter 1 provides a brief introduction to microsystems technology and its applications. It also articulates the motivations that usher the author to pursuit the research in the directions of microsystems technology for biosensing and energy harvesting applications.

Chapter 2 reviews recent research and development of microsystems in two specific areas: energy harvesting and biological sensing. The chapter begins with a discussion of different techniques used to generate microwatts power from mechanical energy sources, which are available in the ambient. Then the microsystems based electrostatic micro power generator is emphasized. The second part of this chapter discusses on various methods used to implement microsystems devices for biological sensing applications. The operational principle of the impedemetric (dielectric) sensor based on planar IDE capacitor structure will be discussed throughly.

Chapter 3 discusses on a micro structure that is used to implement both actuator and sensor in many micro-systems: the interdigital electrode (IDE) structure. Various analytical models of the IDE structure are analyzed to understand the key factors that affect the performance of the devices. These models are used as an initial guide for designing of various prototypes demonstrated in this thesis. The second part of this chapter presents simulation of both micro-scale energy harvesting and nano-scale biological sensing devices. The results obtained from these simulations buttress the potential for practical implementation of these devices.

Chapter 4 considers many aspects related to microsystems fabrication process. In the first part of the chapter, the fundamental concepts of microfabrication such as photo mask, photo resists and photolithography are briefly introduced. In addition, the advanced technique used to fabricate nanoscale structure using electron beam lithography (EBL) is also included. Various methods used for thin film deposition are also discussed. The second part of this chapter presents in detail several fabrication processes used to fabricate microscale IDE device, nanoscale IDE device and nanoscale resonator device.

Chapter 5 demonstrates the first contribution of this thesis, the application of microsystems for energy harvesting. This chapter discusses in detail the principle of a novel electrostatic micro power generator that utilizes the liquid droplet to achieve significant change in capacitance of a variable capacitor. The measurement results from various experiments are analysed and compared with relevant previous works to highlight the advantages of this device. The chapter ends with discussion on potential improvements of the proposed device.

Chapter 6 describes an application of microsystems in biological sensing. A fully functional system that utilizes nanoscale sensor to detect GFAP antibody is demonstrated. The fundamental of this sensor is the interdigital coplanar waveguide (ID-CPW) structure fabricated on a Si substrate. This proof of concept highlights many advantages of using microsystems based nanoscale sensors for bimolecular detection, both in cost, sensitivity and time.

Chapter 7 summarizes the works done in this thesis. It also proposes future directions to further advance the concepts of the prototype devices.

1.3 Contribution of this thesis

The thesis contributes to the area of microsystems technology and its applications in the areas of energy harvesting and biological sensing. The contributions include:

- A new class of electrostatic micro power generator which is based on the moving of ionic liquid. This type of device has been demonstrated to be able to operate at low bias voltage and vibrational frequency, which result in an order of magnitude improvement in term of figure-of-merit (FOM) compared to previous works.
- A nanoscale sensor system that is able to detect picograms per mililitre of molecules in a sample. This has been applied to detect antibody against GFAP which is a relevant bio-marker for the detection and management of glioma.
- Techniques to build and optimize various IDE structures, both at micro and nano scale, which can be used in a wide range of applications.

1.4 Author's publication

Journal publications

- **Huynh, D.H.**, Nguyen, T.C., Nguyen, P.D., Abeyrathne, C.D., Hossain, M.S., Evans, R. and Skafidas, E., 2016. Environmentally friendly power generator based on moving liquid dielectric and double layer effect. *Scientific Reports*, 6, p.26708.
- Abeyrathne, C., **Huynh, D.H.**, Mcintire, T.W., Nguyen, T., Nasr, B., Zantomio, D., Chana, G., Abbott, I., Choong, P., Catton, M. and Skafidas, S., 2016. Lab on a Chip Sensor for Rapid Detection and Antibiotic Resistance Determination of Staphylococcus Aureus. *Analyst*
- Abeyrathne, C.D., **Huynh, D.H.**, Lee, T.T., Nguyen, T.C., Nasr, B., Chana, G. and Skafidas, E., 2016. GFAP Antibody Detection Using Interdigital Coplanar Waveguide Immunosensor. *IEEE Sensors Journal*, 16(9), pp.2898-2905.
- Hossain, M.S., **Huynh, D.H.**, Nguyen, P.D., Jiang, L., Nguyen, T.C., Al-Dirini, F., Hossain, F.M. and Skafidas, E., 2016. Enhanced thermoelectric performance of graphene nanoribbon-based devices. *Journal of Applied Physics*, 119(12), p.125106.
- Nguyen, P.D., Nguyen, T.C., Hossain, F.M., **Huynh, D.H.**, Evans, R. and Skafidas, E., 2015. Negative differential resistance effect in planar graphene nanoribbon break junctions. *Nanoscale*, 7(1), pp.289-293.

Conference publication

- **Huynh, D.H.**, Nguyen, P.D., Nguyen, T.C., Skafidas, S. and Evans, R., 2015, December. CMOS compatible fabrication process of MEMS resonator for timing reference and sensing application. *In SPIE Micro+ Nano Materials, Devices, and Applications* (pp. 96684W-96684W). International Society for Optics and Photonics.

Chapter 2

Literature Review

2.1 Introduction

This chapter provides a literature review on the applications of microsystems in the areas of energy harvesting and biological sensing. The fundamental concepts necessary for understanding these fields are included. The first part of this chapter looks at various techniques used to harvest available mechanical energy from ambient. Among many different transducer methods, microsystem based electrostatic micro power generator (EMPG) is thoroughly covered. The second part of this chapter discusses the usage of microsystems in different biological applications. The microsystems based impedimetric miniaturized biosensors is intensively discussed.

2.2 Microsystems for energy harvesting

This section reviews the application of microsystems devices in energy harvesting. it starts with discussions on various available ambient energy sources and the need for energy harvesting at microscale. Different methods to convert ambient mechanical energy into usable electrical energy are introduced. The key structures and conversion methods used in microsystems based EMPG are then discussed in detail. This section ends with a summary of the state-of-the-art demonstrations of these devices.

2.2.1 Background

Current wireless sensor, bio-implant, and microscale biosensor devices can operate at very low power, in orders of microwatts. This has prompted many research into the field of micro power generator that can harvest the available ambient energy sources to autonomously supply or extend the life of the sensing system. Current advances in micro fabrication techniques have further boosted this trend. In our surrounding environment, there are many available energy sources that can be harvested. These include mechanical, thermal, radiant, and biochemical sources. Figure 2.1 summarizes the power density of the four main types of mentioned energy sources. Radiant energy source, in form of solar radiation, has highest power density, which is up to 100 000 µWcm^{-2} . It has become the mainstream alternative power source to fossil fuels. However, solar energy is only available during the day and is reduced in dark areas or on rainy days. In some applications such as indoor sensing or body implanted devices, this source is not accessible. Thermal and biochemical sources have comparatively low power density; usually not exceeding 10 µWcm^{-2}. Ambient mechanical energy power density is moderately high, ranging from 100 to 1000 µWcm^{-2} [2]. These mechanical sources are mainly due to vibration or stress/strain and they are widely available. The causes for these vibration or stress/strain are ubiquitous. They can be wind, sea water wave, body movement, car/engine vibration, blood flow and heartbeat, respiration and air-conditioning.

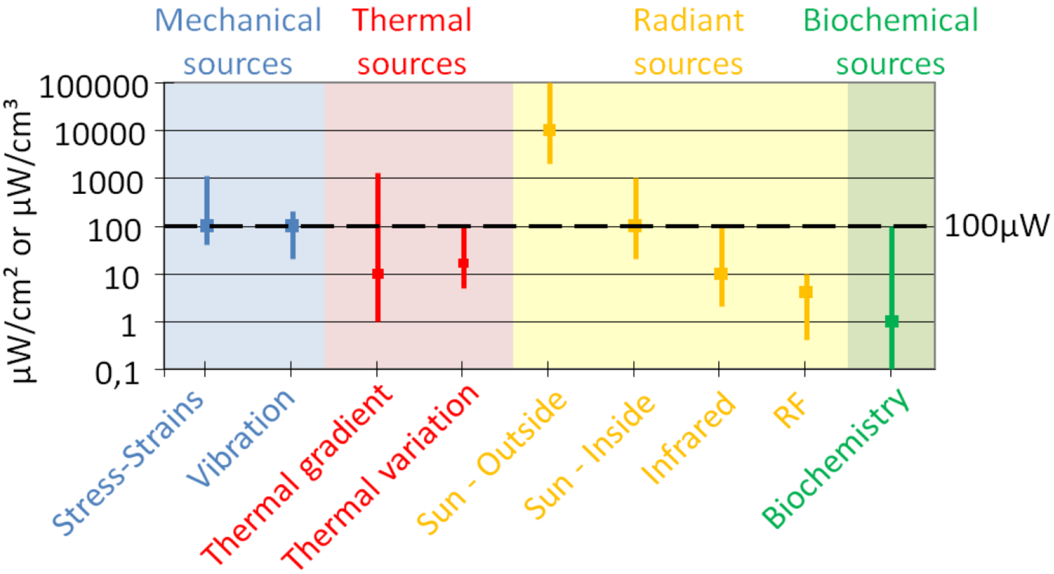

Figure 2.1: Power density of popular ambient energy sources before conversion. Copied from [2].

To convert a mechanical energy source to electrical energy, there are three popular transducer methods being used, namely piezoelectric, electromagnetic, and electrostatic. Figure 2.1 shows the fundamental concept of these methods. Piezoelectric is the most widely used technique due to its simplicity in device fabrication and control circuitry, which usually does not require any external power sources to operate. These devices exploit the piezoelectric property of materials to generate charge under stress or strain. However, piezoelectric materials are rare and/or expensive to synthesis. Electromagnetic power generators are based on electromagnetic induction. They are widely used at macro scale. However, at micro scale electromagnetic transducer devices are difficult to fabricate and integrate. Moreover, the magnetic materials required for device fabrication are expensive. In addition, the efficiency of electromagnetic transducer device is frequency dependent. They are less efficient at low frequency where most of the mechanical energy sources are available [2].

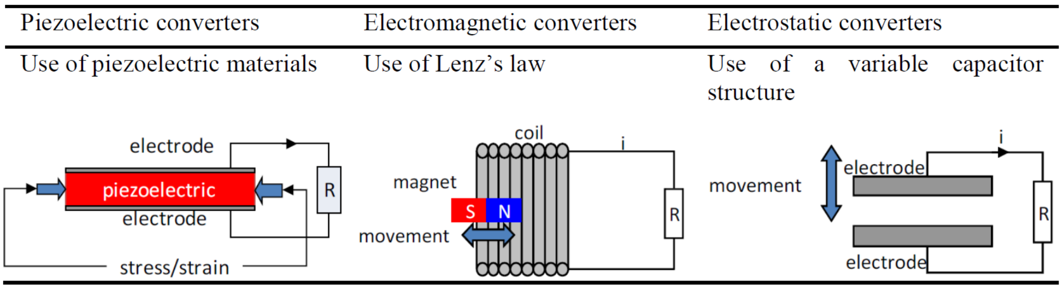

Piezoelectric converters	Electromagnetic converters	Electrostatic converters
Use of piezoelectric materials	Use of Lenz's law	Use of a variable capacitor structure

FIGURE 2.2: Schematic concept of three main transducer methods to convert mechanical to electrical energy: piezoelectric, electromagnetic and electrostatic. Copied from [2].

An EMPG operates based on the principle of a variable capacitor. The materials used to fabricate these devices are conventional materials which are widely used in CMOS process such as Si and common metals. Furthermore, the fabrication steps to produce this type of device is simple and based on established microfabrication process. This type of device has a great potential to be integrated into the current low cost CMOS devices. This section provides some fundamental concepts related to the EMPG devices. In addition, some previous works on EMPG are also included.

2.2.2 Fundamental of microsystems based EMPG

Electrostatic generators operate based on the principle of a variable capacitor. Suppose a capacitor is modeled with a typical parallel plates structure, its capacitance is defined as:

$$C = \varepsilon_r \frac{A}{d} \tag{2.1}$$

where $A(m^2)$ is the overlap area between two plates and $d(m)$ is the gap between them, $\varepsilon_r(F/m)$ is the permittivity of the material between the two metal plates. This permittivity relates to the material dielectric constant and permittivity of free space as $\varepsilon_r = k.\varepsilon_0$ and therefore the equation 2.1 can be rewritten as:

$$C = k.\varepsilon_0 \frac{A}{d} \tag{2.2}$$

Suppose the potential different between the two plates is V($volts$) and the charge on the plate is Q ($coulomb$), then the energy stored on the capacitor is calculated as:

$$E = \frac{1}{2}QV = \frac{1}{2}CV^2 = \frac{1}{2}\frac{Q^2}{C} \tag{2.3}$$

The electrostatic force (N) which is perpendicular to the plates of the capacitor can be defined as follows:

For constant charge Q on the plates:

$$F = \frac{1}{2}\frac{2Qd}{\epsilon_r A} \tag{2.4}$$

For constant voltage V between two plates:

$$F = \frac{1}{2}\frac{\epsilon_r A V^2}{d^2} \tag{2.5}$$

The work done against this electrostatic force will be translated to energy to be harvested. The origin of the work done is the changing capacitance of the device under external mechanical vibration while other conditions are maintained [36].

2.2.3 Variable capacitor structures for electrostatic generator

Nowadays, there are fours fundamental micro structures that are widely used to implement the variable capacitor for electrostatic micro power generator: in-plane overlaps varying, in-plane gap closing, in-plane variable surface and out-of-plane gap closing [2]. Details of these structures are described as below.

In-plane overlap varying

Figure 2.3 shows a top view schematic of a typical in-plane overlap varying variable capacitor. In this structure, the two interdigital electrodes (in blue color) are fixed and the center part (in red color) is movable in the forward-backward direction which will change the overlap area between them. Hence, the capacitance between the center part and the electrodes will vary accordingly. This structure can produce two out-of-phase variable capacitors at the same time, which can be very useful in some power conversion topology.

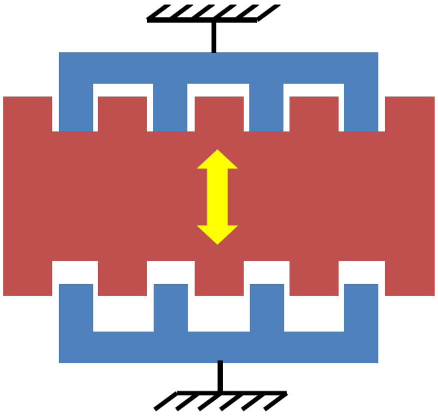

FIGURE 2.3: Top view schematic of a typical in-plane overlap varying capacitor: center part is movable and hence changing the overlap area with the fixed electrodes. Copied from [2].

In-plane gap closing

Figure 2.4 shows a top view schematic of a typical in-plane gap closing variable capacitor. In this structure, the two interdigital electrodes (in blue color) are fixed and the center part (in red color) is movable in the left-right direction which will change the gap between them. Hence, the capacitances between the center part and the electrodes will vary accordingly.

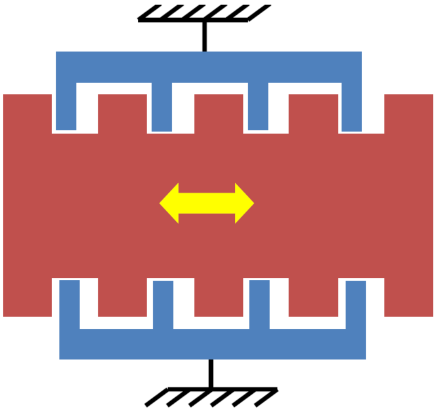

FIGURE 2.4: Top view schematic of a typical in-plane gap closing variable capacitor: the center part (red color) is movable and the two interdigital electrodes (blue color) are fixed, hence the gap between them is changed. Copied from [2].

In-plane variable surface areas

Figure 2.5 shows a cross-section view schematic of a typical in-plane variable surface areas variable capacitor. In this structure, both the fixed electrode (in blue color) and the movable electrode (in red color) are patterned to achieve periodically deep surface roughness. The movement of the top electrode will change the surface areas between it and the fixed electrode and hence the variable capacitor will be formed.

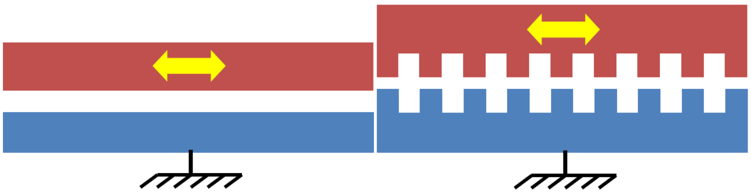

FIGURE 2.5: Cross-section view schematic of a typical in-plane variable surface areas variable capacitor: the top electrode is movable in left-right direction, hence the surface areas between the two electrode is changed. Copied from [2].

Out-of-plane gap closing

Figure 2.6 shows a cross-section view schematic of a typical out-of-plane gap closing variable capacitor. In this structure, an electrode (in blue color) is fixed and the other electrode (in red color) is movable in direction which is perpendicular to their surfaces.

This movement will change the gap between the two electrodes and therefore a variable capacitor will be formed.

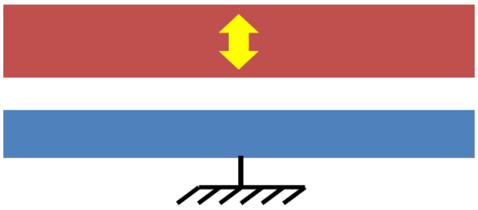

FIGURE 2.6: Cross-section view schematic of a typical out-of-plane gap closing variable capacitor: the top electrode is movable in up-down direction, hence the gap between the two electrodes is changed. Copied from [2].

2.2.4 Energy conversion principle of electrostatic generator

An electrostatic generator converts mechanical energy (from vibration or rotation) to electrical energy by utilizing the variable capacitor structure. There are two main methods used to perform this conversion, namely charge constraint conversion and voltage constraint conversion.

Charge constraint conversion cycle

Figure 2.7 summarizes a charge constraint conversion cycle [2]. The cycle starts with the capacitance of the variable capacitor is at its maximum value C_{max} (Q_1). The capacitor is then charged by an external source to the value of Q_{cst} at the voltage level of U_{min} and it is disconnected to the voltage source (Q_2). Under an external mechanical effect, the capacitance of the variable capacitor changes to its minimum value C_{min}. Since the charge Q_{cst} is kept constant while the value of capacitance is reduced to its minimum value C_{min}, the voltage across the variable capacitor will increase to a value of U_{max} (Q_3). At this stage the charge can be removed from the system to the load R (Q_4).

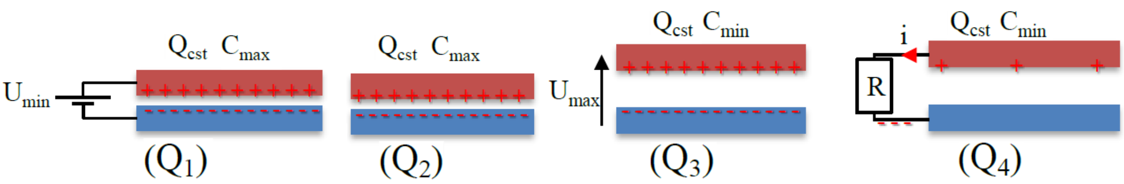

FIGURE 2.7: Charge constraint conversion cycle. Copied from [2].

The total energy gained per charge constraint conversion cycle is defined as [2] [11]

$$E_Q = \frac{1}{2}Q_{cst}^2(\frac{1}{C_{min}} - \frac{1}{C_{max}}) \tag{2.6}$$

Voltage constrained conversion

Figure 2.8 summarizes the voltage constraint conversion cycle [2]. The cycle starts with the variable capacitance at its maximum value C_{max} (V_1). The capacitor is biased at a voltage U_{cst} under an external supply source, such as battery or charged super capacitor. The biased voltage will be maintained over the entire conversion cycle. The external mechanical force does the work to change the capacitance of the variable capacitor to its minimum value C_{min} (V_2). The change in capacitance, while the biased voltage is kept constant, generates current which flows back to the charge reservoir (V_3).

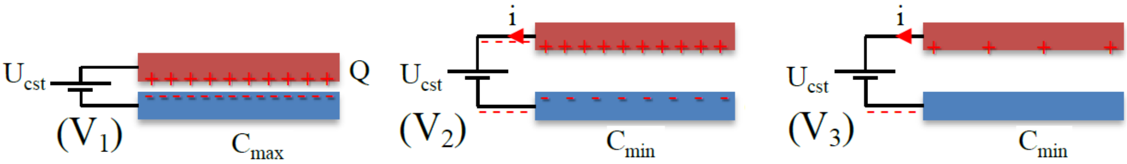

FIGURE 2.8: Voltage constrained conversion cycle. Copied from [2].

The total energy gained per voltage constraint conversion cycle is define as [2] [11]

$$E_U = \frac{1}{2}U_{cst}^2(C_{max} - C_{min}) \tag{2.7}$$

2.2.5 Source of biased voltage for conversion

Typically, an EMPG requires a power source to operate. This power source is employed to provide charge (for charge constraint conversion cycle) or provide bias voltage (for voltage constraint conversion cycle). There are two main types of power sources used for this purpose: pre-charged electret and conventional voltage source.

Precharge Electrets

Electrets are dielectric materials that can store charge permanently or over a very long period of time. They are also referred to as electrostatic dipoles. Generally, an electret can be achieved by dipole orientation or by charge injection. An electret that is created by dipole orientation is called oriented-dipole electret. On the other hand, an electret that is created from charge injection is called a real-charge electret. Today most electrets are real-charge electret since they can be produced with a standard fabrication process. The base of a real-charge electret is a dielectric layer, then an amount of excess charge is injected into this layer using processes such as corona discharge, electron beam, or ion/electron guns. Currently, the typical materials used for dielectric layers are Teflon, SiO_2 and CYTOP. The life time of an electret can be as long as 3 years [2].

An EMPG that operates based on the principle of electret is referred to as an electret-based EMPG. Due to its long term stability, electret-based EMPG generator is targeted for using in medium and long term applications.

Conventional voltage sources

An alternative method to provide bias voltage source to an EMPG is to utilize conventional voltage sources such as a battery or a charged super capacitor. An EMPG that utilises this conventional biased sources rather than electret is referred as an electret-free EMPG.

2.2.6 State-of-the-art research on microsystems based EMPG

The state-of-the-art works on electret-based EMPG devices are summarized in Table 2.1 and electret-free EMPG devices are summarised in Table 2.2.

Reference (Year)	Power	Size (surface/volume)	Electret Voltage	Condition
Jefimenko [37] (1978)	$25mW$	$730cm^2$	$500V$	$6000rpm$
Tada [38] (1992)	$1.02mW$	$90cm^2$	$363V$	$5000rpm$
Boland [39] (2003)	$25\mu W$	$0.8cm^2$	$150V$	$4170rpm$
Boland [40] (2005)	$6\mu W$	$0.12cm^2$	$850V$	$7.1G@60Hz$
Tsutsumino [41] (2006)	$38\mu W$	$4cm^2$	$1100V$	$1.58G@20Hz$
Lo [42] (2007)	$2.26\mu W$	$4.48cm^2$	$300V$	$14.2G@60Hz$
Sakane [43] (2008)	$0.7mW$	$4cm^2$	$640V$	$0.94G@20Hz$
Edamoto [44] (2009)	$12\mu W$	$3cm^2$	$600V$	$0.87G@21Hz$
Boisseau [45] (2011)	$50\mu W$	$4.16cm^2$	$1400V$	$0.1G@50Hz$

Table 2.1: The state-of-the-art works on electret-based EMPG devices

Reference (Year)	Power	Size (surface/volume)	Bias Voltage	Condition
Tashiro [46] (2002)	$36\mu W$	$15000mm^3$	$45V$	$1.2G@6Hz$
Mitcheson [47] (2004)	$24\mu W$	$1568mm^3$	$2300V$	$0.4G@10Hz$
Despesse [48] (2005)	$1050\mu W$	$18000mm^3$	$3V$	$0.3G@50Hz$
Yen [49] (2006)	$1.8\mu W$	$21780mm^3$	$6V$	$1560Hz$
Hoffmann [50] (2009)	$3.5\mu W$	$30mm^2$	$50V$	$13G@1300Hz$
Basset [51] (2009)	$0.5\mu W$	$61.5mm^3$	$8V$	$0.25G@250Hz$

Table 2.2: The state-of-the-art works on electret-free EMPG devices

2.3 Microsystems for biological sensing

2.3.1 Background

This section reviews a special class of microsystems devices used in biological applications which is referred to as BioMEMS. Currently, the application of microsystems in this field is growing rapidly due to the multiple advantages that microsystems technology has offered. Firstly, microsystems technology has enabled many medical platforms to handle very small volumes of biological samples, which can be in microlitres range. Secondly, fabrication of microsystems devices can be highly integrated, therefore many sample processing steps (such as filtering, separating, mixing, heating, pumping) can be included in a single device. Hence, the overall cost to perform an analysis can be significantly reduced. In addition, microsystems devices have surpassed the traditional testing methods in terms of sensitivity, specificity and testing time [12]. For this reason, microsystems has been demonstrated in many biological applications, including miniaturized biosensors [13] [14] [15] [16], diagnostics [17] [18] [19], tissue engineering [20] [21] [22] [23] [24], medical implants and surgery [25] [26] [25] [27] [28] [29] [30].

This section provides a brief introduction to microsystems based biosensor concepts.

2.3.2 Fundamental concepts of biosensors

Generally, a biosensor can be defined as a device that consists of a biological recognition system and a transducer [3]. The biological recognition system is referred as bioreceptor. This bioreceptor is selected to match with a specific analyte of interest. The interaction between the bioreceptor and the analyte causes an effect that can be picked up by a transducer method. A system level diagram which shows the principle of biosensing system is presented in Figure 2.9.

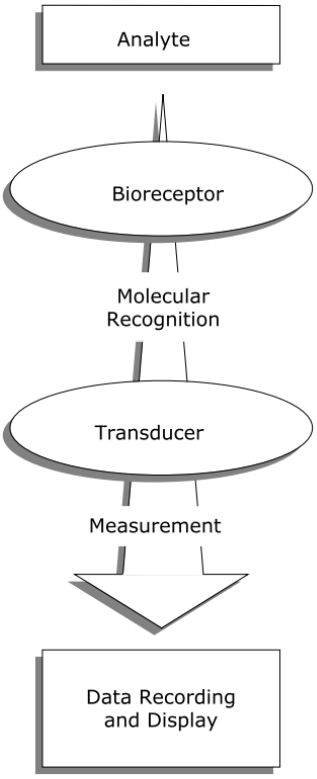

FIGURE 2.9: Schematic description of a biosensing system. Copied from [3].

A biosensor can be classified either based on the type of bioreceptor used or by the transducer methods used. Figure 2.10 shows a diagram of biosensor classification. So far, well established bioreceptors used are antibody, enzyme, DNA, living cell and biomimetic [3]. In terms of transducers, the popular methods used are optical, electrochemical, mass-sensitive, and other methods of detection. From a microsystems technology perspective, the classification using a transducer method is preferred.

2.3.3 Popular transducer techniques used in biosensors

Optical technique

Optical based detection technique is one of the most widely used techniques in biosensing applications. In this method, spectrochemical properties such as amplitude, energy, polarization, decay time and phase are utilized as the key of detection [3]. Biosensors which are developed based on optical detection can be categorized by the technology platform used to implement the devices as proposed by Fan et al. [52]. The main types in this

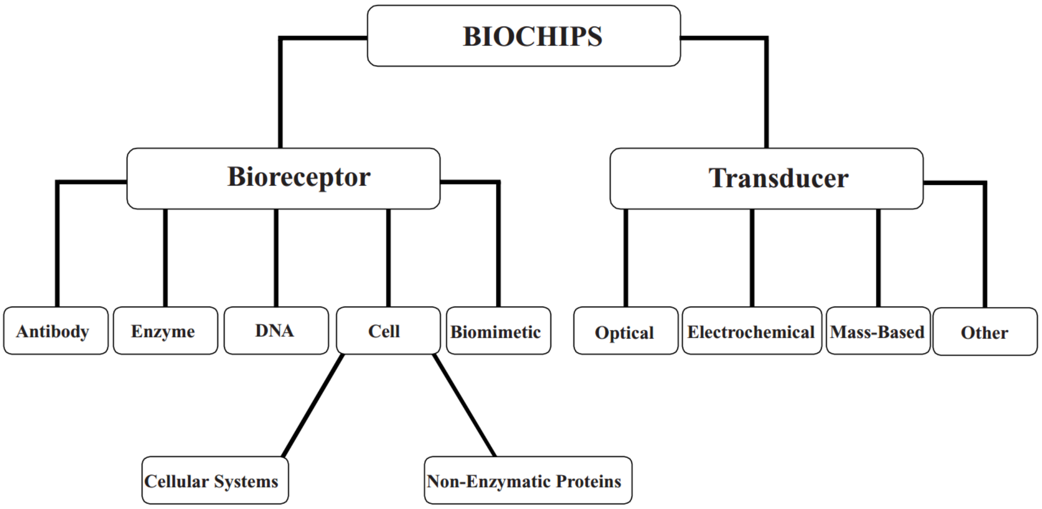

FIGURE 2.10: Biosensors classification. Copied from [3].

category include surface plasmon resonance biosensor [53] [54] [55] [56], interferometer-based biosensors [57] [58] [59], optical waveguide based biosensors [60] [61] [62], optical ring resonator based biosensors [63] [64] [65], optical fiber based biosensors [66] [67] [68] and photonic crystal based sensors [69] [70] [71].

Electrochemical technique

The second technique that is widely used in biosensors is the electrochemical detection method. Sensor devices that are implemented using this technique contain a bioreceptor that selectively undergoes a chemical reaction with a target analyte. This reaction produces an electrical signal that is correlated to the concentration of analyte [72]. Generally, this electrochemical reaction can produce an electrical signal in the form of current (amperometric), charge accumulation or electric potential (potentiometric) or it can modify the conductivity of the medium (conductometric) [73]. Examples of potentiometric detection biosensors are reported in [74] [75] [76]. Examples of amperometric detection biosensors are reported in [77] [78] [79]. Examples of conductometric detection biosensors are reported in [80] [81] [82].

Mass-sensitive technique

Mass-sensitive technique has recently gained great interest in the biosensing research community due to its high sensitivity. The principle operation of this method is based on the changing mass of a micro or nano cantilever, after a biological analyte binds on its surface. The additional mass can cause change in surface stress of the cantilever, in the bulk cantilever material or change the natural resonant frequency of the cantilever [83]. This type of sensor can be categorized using the readout methods, which includes optical [84] [85] [86] [87] [88], capacitive [89] [90] [91], piezoelectric [92] [93] [94] and piezoresistive readout [95] [96] [97] [98].

2.3.4 Planar structure impedemetric technique

Among other detection methods mentioned in Figure 2.10, the planar structure impedemetric detection technique is one of the most widely used method due to its simplicity in sensor fabrication and ease in system integration. Many previous works based on this technique [4] [5] [99] [100] [101] [102] [103] [104] [105] [106] [107] have been successfully demonstrated to be able to detect various analytes such as proteins, antigens/antibodies, cells and bacteria.

The principle operation of this technique is based on the variation of impedance of the medium, above planar electrodes, when a specific analyte is presented. Figure 2.11 shows a schematic concept of a typical impedimetric sensor with interdigital electrode (IDE) capacitor structure. The device includes two thin metal electrode arrays on top of a thick substrate, as can be seen in Figure 2.11(a). A top view section of this structure can be seen in Figure 2.11(b), which also includes the indication of electric field lines between the two electrodes under an applied voltage when there is no affinity binding of any analyte. The sensing surface (either metal or oxide) can be functionalized to capture a specific analyte. Suppose there is affinity binding on the sensing surface, the electric field between the two metal electrodes will be modified. This can be detected as in impedance change between the two electrodes.

Geometric structure and size of the electrodes are the most critical parameters that effect the performance of this sensing technique. To date, IDE is the most widely used structure. Depending on the size and dielectric property of the target analyte and the medium above the sensing area, appropriate dimensions can be selected. For an IDE capacitor structure with the finger width of w_{el} and space between the fingers of w_{sp}, the effective length is defined as $L = w_{el} + w_{sp}$. This length is critical for designing an optimal sensor since it dictates the effectiveness of the medium above the sensing

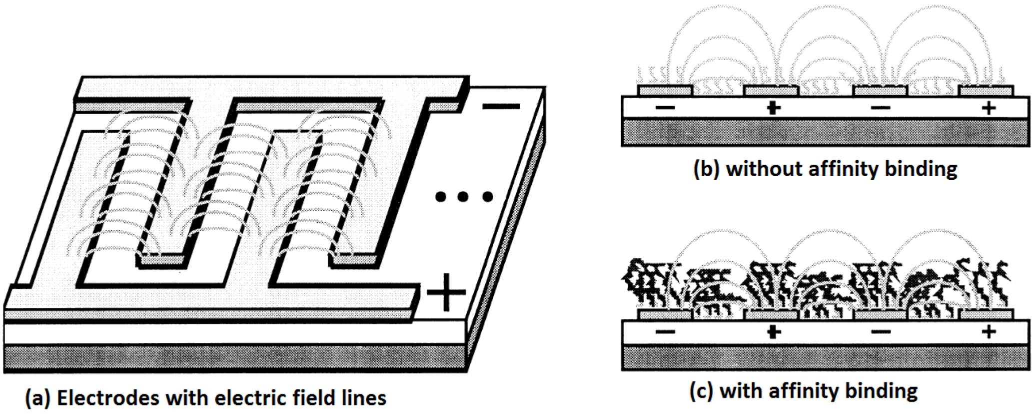

FIGURE 2.11: Schematic concept of planar impedimetric, (a) topview of sensor showing electrodes and electric field lines, (b) sideview of sensor showing the electric field without affinity binding, (c) sideview of sensor showing affinity binding of analyte and electric field lines. Copied from [4, 5].

area. Generally, only the medium below two multiples of the effective length L would contribute to the change in capacitance. This can be visualized from Figure 2.12

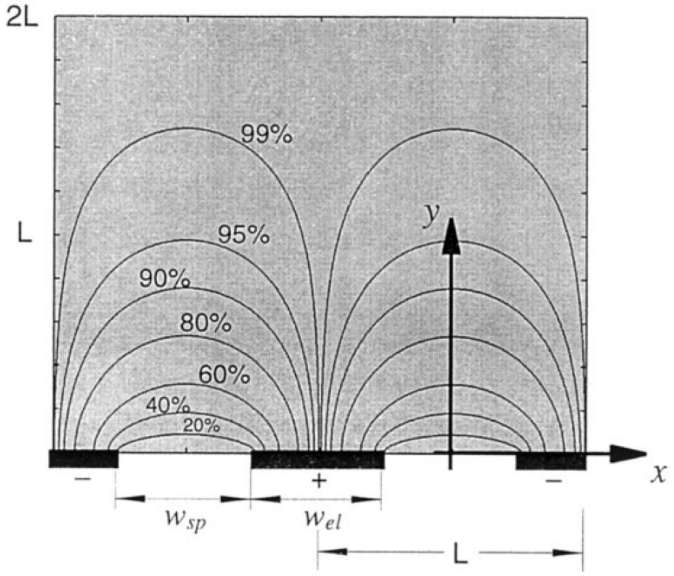

FIGURE 2.12: Coverage of electric field above electrode with respect to the effective length L, 99% coverage is below $1.5L$. Copied from [4].

Since the majority of biological sensing measurement are performed in some form of buffer solution such as phosphate-buffered saline (PBS), an electrical model of this sensing system should also take into account the effect of this solution. Figure 2.13(a) shows the equivalent electrical model of the sensor in an ionic solution. In this model, C_{di}

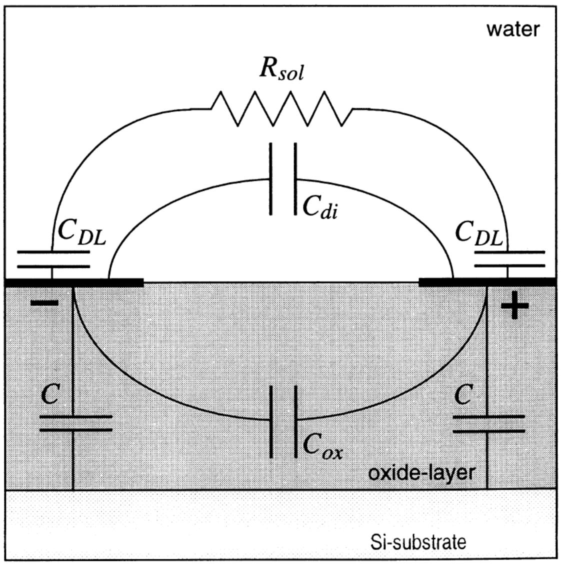

(a) Complete model of IDE sensor in ionic solution

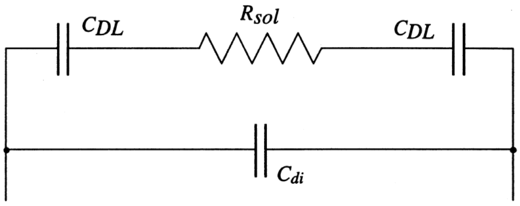

(b) Simplified model of IDE sensor in ionic solution

FIGURE 2.13: Electrical model of impedimetric biosensor based on IDE capacitor, (a) a complete model of IDE sensor in a ionic solution, (b) a simplified model without parasitic effects of the substrate. Adapted from [4, 5].

represent the IDE capacitance, which only depends on the geometric dimensions of electrodes and dielectric constant of the medium on upper half plane. C_{DL} is the double layer capacitance produced from the interface between the liquid ionic solution and the surfaces of electrodes. R_{sol} is the equivalent series resistance which depends on the concentration of the ionic solution and the surface areas of the electrodes. According to Van Gerwen et al. [4] these quantities can be estimated as following:

$$R_{sol} = \frac{1}{nl}\frac{1}{k}\frac{2K(sin(\frac{\pi w_{sp}}{2L}))}{K(cos(\frac{\pi w_{sp}}{2L}))} \tag{2.8}$$

$$C_{di} = nl\varepsilon_r \frac{K(cos(\frac{\pi w_{sp}}{2L}))}{2K(sin(\frac{\pi w_{sp}}{2L}))} \tag{2.9}$$

where K is the complete elliptic integral of the first kind, l is the length of the fingers and n is the total number fingers, k is the conductivity of the ionic solution and ε_r is the permittivity of solvent of the ionic solution.

The elements of the model which are only due to the effect of the lower half of the sensor, including C and C_{ox}, are fixed and common to all measurements. Therefore, they can be ignored, and hence a simplified model can be used, shown in Figure 2.13(b).

In realistic, the targeted binding creates an inhomogeneous dielectric medium. So far, there has not been any general model proposed for this inhomogeneous medium. However, due to the nature of the very low concentration of target analyte, the effect of this inhomogeneous medium is minimal and therefore can be ignored during initial stage of sensor design and planning of measurement. In general, the sensitivity of this type of sensor is primarily dictated by the geometry of the IDE structure and the quality of surface functionalization.

2.4 Conclusion

In conclusion, this chapter provides a literature review on the applications of microsystems technology in the micro scale energy harvesting and biological applications. The fundamental concepts of microsystems based EMPG are explained both in terms of their geometric structures and their operational principles. The current state-of-the-art works in this field are also summarized. This chapter also discusses applications of microsystems technology in biological sensing with highlights on miniaturized biosensors. Principle operation of impedance based spectroscopy technique is explained thoroughly.

Chapter 3

Modeling and Simulation of IDE Capacitor

3.1 Introduction

Interdigital electrode (IDE) is one of the most widely used structures in microsystems applications. Its popularity is firstly due to its planar structure, which can be easily fabricated using the current microsystems techniques. Secondly, this structure offers high capacitance density; therefore, it can provide high sensitive capacitive sensing device with a small form factor. The first application of IDE structure can be tracked back to 1970 when it was implemented as a lump element for microwave circuit [108]. Since then, this structure has been intensively utilized in a wide ranges of applications. In mainstream CMOS IC design, IDE structure is chosen to implement on-chip capacitors. In emerging microsystems technology, it has been used in almost every application. In their review paper in 2004, Mamishev et al. have listed a great number of applications based on IDE structure. These include humidity and moisture sensing, electrical insulation properties sensing, monitoring of curing process, chemical sensing, biological sensing and other transducers applications [109]. Recently, IDE structure is also utilized in energy harvesting applications [110–112].

In this thesis, IDE devices are fabricated and utilized in various applications, including microscale energy harvesting devices and nanoscale biological sensors to detect antigen/antibody. This chapter investigates relevant analytical models used in IDE calculation and conducts a finite element method (FEM) simulation study on various IDE structures using CoventorWare, a commercial microsystems simulation tool. The simulation is carried out to support and verify the design concepts of IDE devices for the two mentioned applications.

3.2 Analytical model of IDE capacitor structure

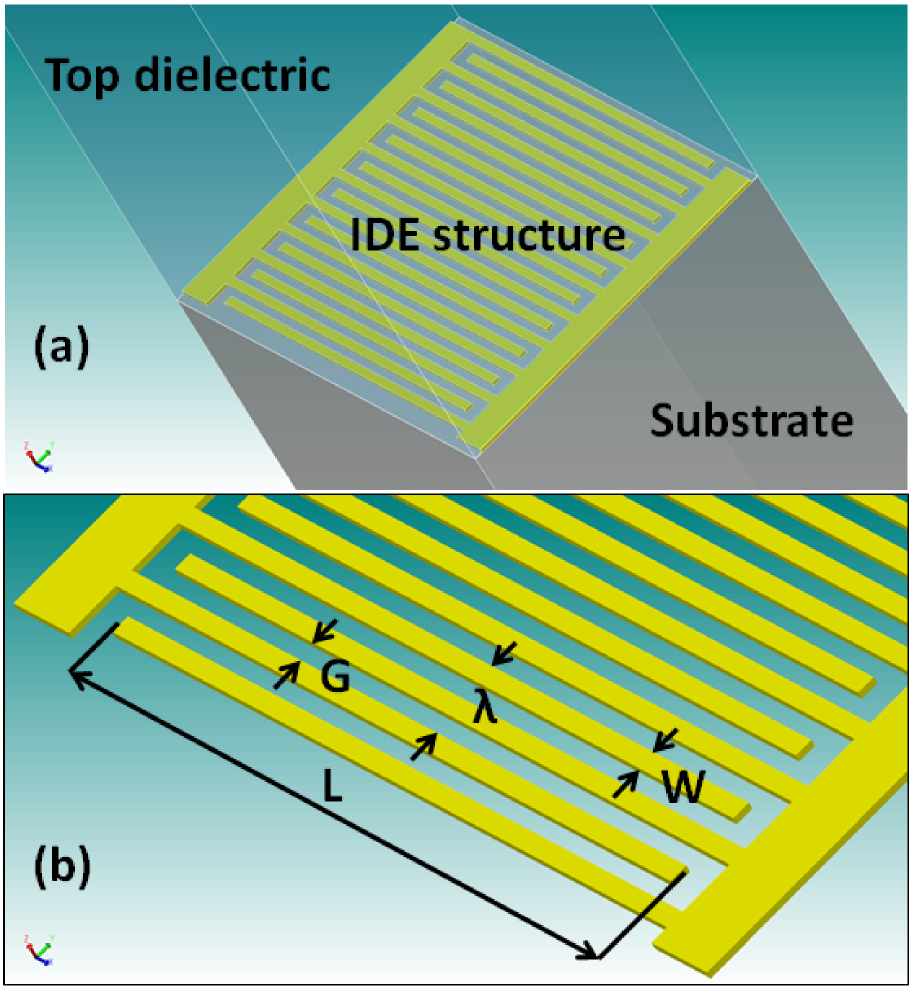

Figure 3.1: Schematic layout of a typical IDE capacitor:(a) overall 3D structure with substrate and top dielectric, (b) critical dimensions used in analytical modeling, where L and W are finger length and width respectively, G is the gap between finger and $\lambda = 2(G + W)$.

A typical IDE capacitor structure can be described as in Figure 3.1. It includes a thick substrate layer, a top dielectric layer and an array of multiple metal fingers, which are combined to form 2 metal electrodes. Various models have been proposed to estimate the capacitance of this IDE structure. The first model of IDE capacitor can be attributed to Alley in 1970 [108]. The model was constructed based on lossless coupled microstrip line theory. This model estimates the capacitance value for IDE capacitor with the same finger width and the gap between fingers. It assumes that the top dielectric layer is only air and its thickness is infinite. In 1983, Esfandiari et al. introduced an improved model which also included the effect of the thickness of metal electrodes [113].

The limitation of these proposed models is that it only performs well for structure with infinite thickness of the top layer dielectric. This is not practical for most of chemical and biological sensing applications. In 1996, Gevorgian et al. proposed a model that considers multiple top dielectric layers [114]. However, this model still gives significant discrepancy with the result obtained by either FEM simulation or experiments.

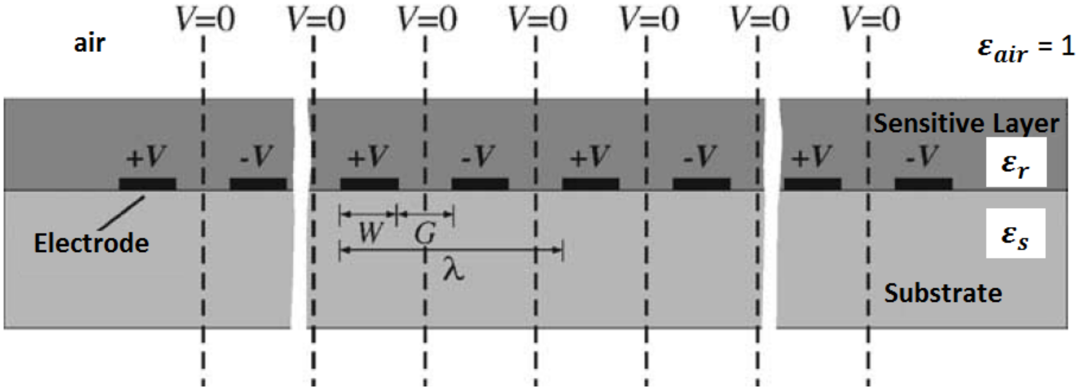

FIGURE 3.2: Schematic description of IDE model proposed by Igreja and Dias, which includes a substrate layer and multiple top dielectric layer. Copied from [6].

In 2004, Igreja and Dias introduced a new model which took into account multiple sensitive top layers [6], as shown in Figure 3.2. This model has proven to be in good agreement with FEM simulation and experimental results. The formula used in this model is defined as:

$$C_{IDC} = (N-3)\frac{C_{I,IDC}}{2} + 2\frac{C_{I,IDC}C_{E,IDC}}{C_{I,IDC}+C_{E,IDC}} \tag{3.1}$$

where N is number of fingers, $C_{I,IDC}$ is capacitance between the internal fingers, $C_{E,IDC}$ is the fringing capacitance due to the outer fingers and C_{IDC} is the overall capacitance of the interdigital capacitor. Figure 3.3 shows detail annotation of these quantities with a typical 6 fingers arrangement.

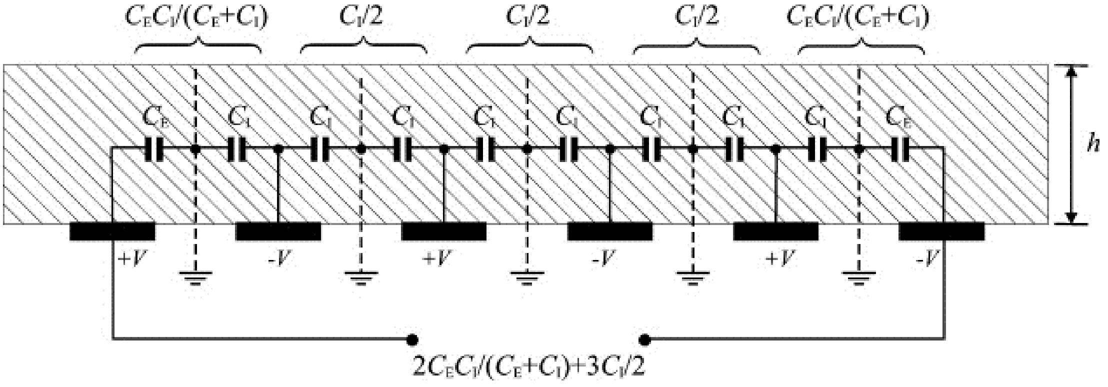

FIGURE 3.3: Schematic description of IDE model proposed by Igreja and Dias, which shows both the capacitance due to inner fingers and the fringing capacitance due to the outer fingers, h is the height of the top dielectric. Copied from [7].

For a typical IDE arrangement which comprises a thick substrate (with a permittivity of ε_s), a single sensitive layer (with a permittivity of ε_r) and an infinite air layer on the top, the value of $C_{I,IDC}$ and $C_{E,IDC}$ is calculated as

$$C_{I,IDC} = C_{I,air} + C_{I,1} + C_{I,S} = \varepsilon_0 L \left(\frac{K(k_{I\infty})}{K(k'_{I\infty})} + (\varepsilon_1 - 1)\frac{K(k_{I,1})}{K(k'_{I,1})} + \varepsilon_S \frac{K(k_{I\infty})}{K(k'_{I\infty})} \right) \quad (3.2)$$

and

$$C_{E,IDC} = C_{E,air} + C_{E,1} + C_{E,S} = \varepsilon_0 L \left(\frac{K(k_{E\infty})}{K(k'_{E\infty})} + (\varepsilon_1 - 1)\frac{K(k_{E,1})}{K(k'_{E,1})} + \varepsilon_S \frac{K(k_{E\infty})}{K(k'_{E\infty})} \right) \quad (3.3)$$

In these equations, $C_{I,air}$, $C_{I,1}$ and $C_{I,S}$ represent the capacitances due to the internal finger electrode with respect to air, sensitive layer and substrate. $C_{E,air}$, $C_{E,1}$ and $C_{E,S}$ represent the capacitances due to the fringing effect of external electrodes with respect to air, sensitive layer and substrate. Quantity $K(k)$ is the complete elliptic integral of first kind with the modulus $k = \frac{h}{\lambda}$ and $k' = \sqrt{1-k^2}$ is complementary modulus. Detail calculation for these terms can be referred to Igreja and Dias.

This thesis utilizes this model as a starting point for designing relevant devices since it only involves in simple numerical calculations yet it gives a good agreement with experimental results and FEM simulations.

3.3 IDE capacitor simulation using CoventorWare

CoverntorWare is a commercial available integrated software tool that supports design and simulation of various microsystems devices. It is capable of performing simulation with multiple physics, including electrostatic, coupled electro-machanics, thermal electric, piezoelectric, piezoresistive, and damping effects. In this section, CoventorWare is utilized to assist the design and simulation of various IDE based devices for various applications, ranging from microscale devices to nanoscale devices. The process to set up a simulation study involved following steps:

- Defining fabrication process for the devices and selecting appropriate material.
- Drawing layout for the device with appropriate structures and dimensions.
- Building 3D model of the device using previously defined process and layout.
- Performing mesh study to appropriately set up mesh for simulation.
- Setting up simulation using appropriate physics and boundary conditions.

For these studies, the main solver used to perform all simulations is the electrostatic solver. There are two different set of devices to be investigated, a microscale device, which is targeted for EMPG, and a nanoscale device, which is targeted for biological sensor to detect antigen/antibody.

3.3.1 Microscale IDE capacitor for energy harvesting device

One of the aims of this thesis is to demonstrate the concept of a novel EMPG device. The principle of this device is the use of movable liquid dielectric to achieve the capacitance change rather than the use of movable solid conductors. This simulation aims to verify capacitance change with respect to the change in relative dielectric constant of the material on top of the IDE structure. In practical application, water droplet is utilized to initiate this change. The value of dielectric constant of the medium above the surface of IDE device will be greatest when water droplet is presented and will be smallest when the water droplet is disappeared, as can be seen in Figure 5.3 and Figure 5.8.

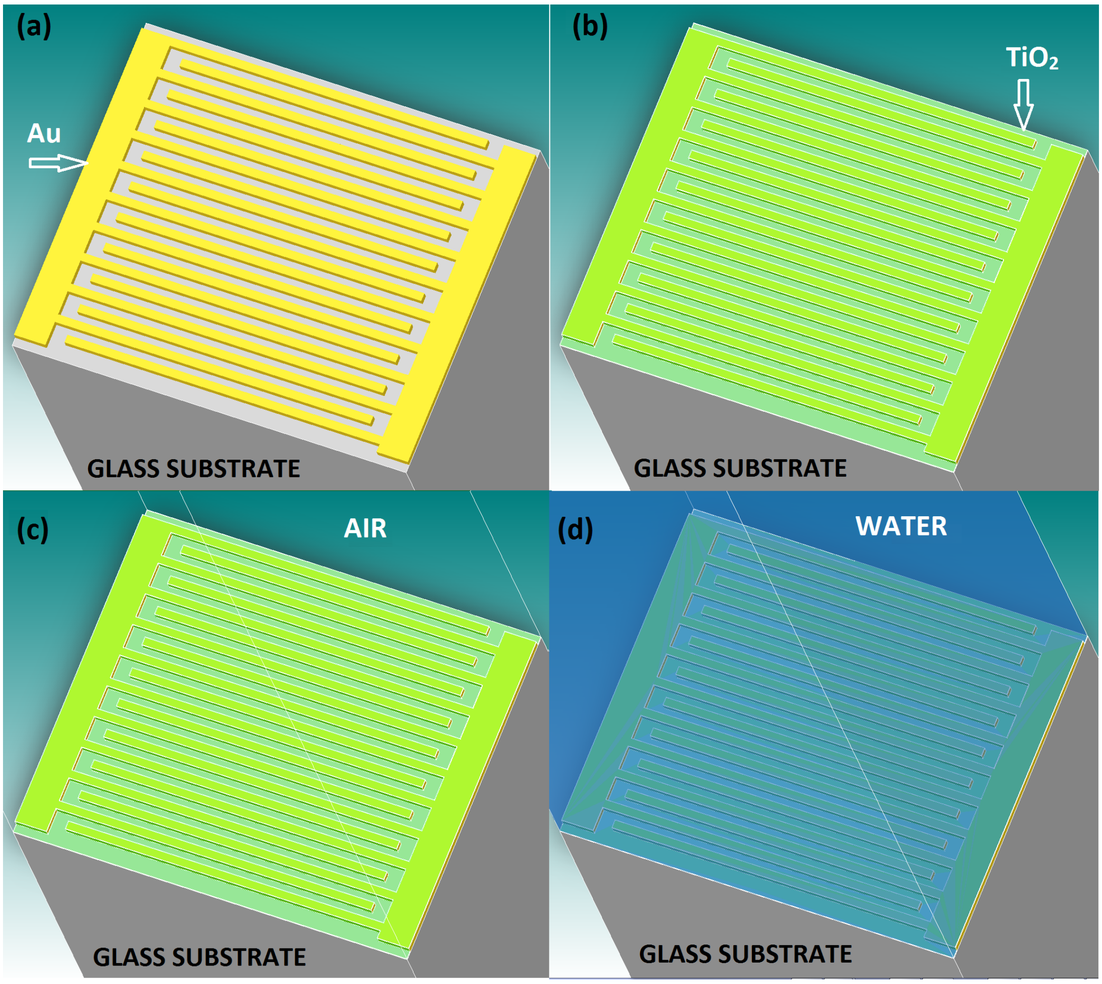

FIGURE 3.4: 3D model of micro-scale IDE capacitor structure used for simulation:(a) the initial device with only metal electrode on substrate,(b) the inclusion of 20 nm TiO_2 layer, (c) device with 20 nm TiO_2 and only air top dielectric and (d) the device with 20 nm TiO_2 and covered with liquid dielectric (H_2O).

Figure 3.4 shows a 3D model of the device used in this study. The model includes a thick glass substrate and two arrays of Au metal fingers which form two terminals of the device, shown in Figure 3.4(a). To facilitate the moving of liquid dielectric on top of the surface of IDE structure, this surface requires to be treated to become hydrophobic. A very thin layer (20 nm) of TiO_2 is used for this purpose. Figure 3.4(b) shows the inclusion of this thin hydrophobic layer. The two extreme conditions of dielectric to be investigated are represented in Figure 3.4(c) and (d), which are corresponding to a top air dielectric coverage and a top liquid (H_2O) dielectric coverage. Typically, the choice of the material and the dimensions of device should be as closed as possible to the real fabricated device. However, the size of an actual measurable device can be greater than 20 mm^2, which would require a long period of time to complete a simulation.

Therefore, the size of the device chosen for this simulation is only 200 μm x 200 μm. However, the relative change in capacitance due to the change in relative dielectric of the coverage medium is still held regardless to the dimensions of the device. The finger width and spacing between them are chosen to be 5 μm, which is a conservative number for practical fabrication of the device with large areas (greater than 20 mm^2). This dimension corresponds to an effective length of 10 μm. Hence, the thickness of the substrate and the top dielectric layer are chosen to be 20 μm, which is two times of effective length, to ensure total coverage of the dielectric effect on the capacitance, as suggested in Figure 2.12. Details of materials used and dimensions of the devices are summarized in table 3.1.

Parameter	**Value**	**Unit**
Finger width	5	μm
Finger length	200	μm
Gap between fingers	5	μm
Electrode material	Au	NA
Electrode thickness	100	nm
Number of finger	20	NA
Thin dielectric material	TiO_2	NA
Thin dielectric thickness	20	nm
Substrate material	Glass	NA
Substrate thickness	20	μm
Top dielectric thickness	20	μm

TABLE 3.1: Materials and device dimensions used for study of capacitance change in microscale IDE capacitor study.

For this simulation, the key point to investigate is the change in capacitance of the device with the movable liquid dielectric. The movement frequency of this liquid droplet should be very low and can be considered as DC. Hence, the MemElectro module of CoventorWare is used for this simulation. Electrostatic solver of MemElectro module is selected to calculate the capacitance between the two metal electrodes. The electrostatic solver performs this calculation with the assumptions that conductors used are perfect conductor, which have a high enough conductivity that polarization can be neglected, and dielectrics used are lossless dielectric, which have zero conductivity. This assumption is reasonable considering the material used for electrode is Au and dielectric materials in the 3D model are glass, air, TiO_2. The electrostatic solver of MemElectro module calculates the capacitance using the following equation:

$$Q = C(V_1 - V_2) \tag{3.4}$$

where Q is the charge on the electrode, C is capacitance between the two electrodes, V_1 and V_2 are the voltages on the two electrodes.

A series of simulations are performed for various relative dielectric constant values of the top dielectric material. The optimized mesh setting for this study is summarized in Table 3.2 and capacitance of the device, which is corresponding to different relative dielectric constant of top layer material, is summarized in Table 3.3.

Layer	**x**(μm)	**y**(μm)	**z**(μm)
Substrate	1	1	1
Metal Electrode	1	1	0.05
Thin Oxide	1	1	0.02
Top dielectric	1	1	1

Table 3.2: Summary of mesh setting for micro power generator study, mesh type is Manhattan bricks and element order is parabolic.

Condition	**Cap(pF)**
A - top layer $\varepsilon_r = 1$	0.489
B - top layer $\varepsilon_r = 40$	1.231
C - top layer $\varepsilon_r = 80$	2.067
D - top layer $\varepsilon_r = 160$	3.023
E - top layer $\varepsilon_r = 240$	4.772

Table 3.3: Total capacitance variation of the device with air as top dielectric and with different top dielectric materials. For $\varepsilon_r = 80$, which is a typical value of water, it is more than 4 times increment in the capacitance.

Figure 3.5 shows the plot of capacitance values of the device with different relative dielectric constant of the top dielectric materials. As expected, the device capacitance is increased as the relative dielectric constant of material is increased. For this proposed structure, glass is chosen as a substrate with the relative dielectric constant of 5. This is relatively low compared to the value chosen for relative dielectric constant of top liquid dielectric, which is ranging from 40 to 240. Therefore, the effect of top layer dielectric is dominant. As a result, the capacitance between the two electrodes is almost linearly dependent on the top layer dielectric constant. Water, which has relative dielectric constant of 80, is supposed to be used in the proposed device. This simulation result indicates that if water is employed as moving dielectric, almost 5 times increase in capacitance can be achieved. This change is significant in comparison to conventional variable capacitor structures.

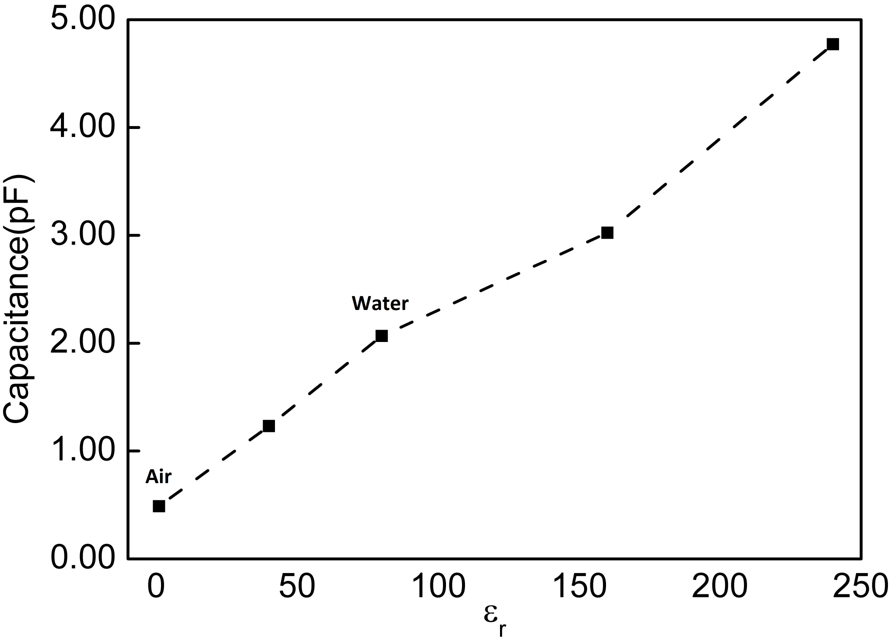

FIGURE 3.5: Changing of device capacitance with respect to top layer dielectric constant. H_2O, with $\varepsilon_r = 80$, will increase the device capacitance by more than 4 times compared to the air, with with $\varepsilon_r = 1$.

3.3.2 Nano-scale IDE capacitor for biological sensing application

This thesis also aims to demonstrate the application of IDE structure in biological sensing, specifically, the detection of nanoscale analyte such as antigen/antibody. In this section, a simulation is set up to study the feasibility of this system. Due to the nanometer size of analyte of interest, the dimensions of IDE capacitor used for this study are chosen to be in nanometers range. The materials used for this study are selected to be closely matched with the available substrate and processes used to fabricate real device. Figure 3.6(a) shows a 3D model of this device. It includes a nanoscale IDE metal structure located on top of a thin layer of SiO_2. The substrate material used here is Si. The dimensions of the device and materials used are summarized in Table 3.4.

The IDE structure presented here is for impedimtric detection of antigen/antibody, which is in order of nanometers. To represent this analyte, a thin layer (20 nm) of polymer (PDMS) is chosen. This layer is considered as the sensitive layer of the sensor system, shown in Figure 3.6(b). Simulation is conducted to investigate the change in impedance between the two terminals of the device. Again, the MemElectro module of CoventorWare is chosen to run this simulation. In this case, the quasielectrostatic solver

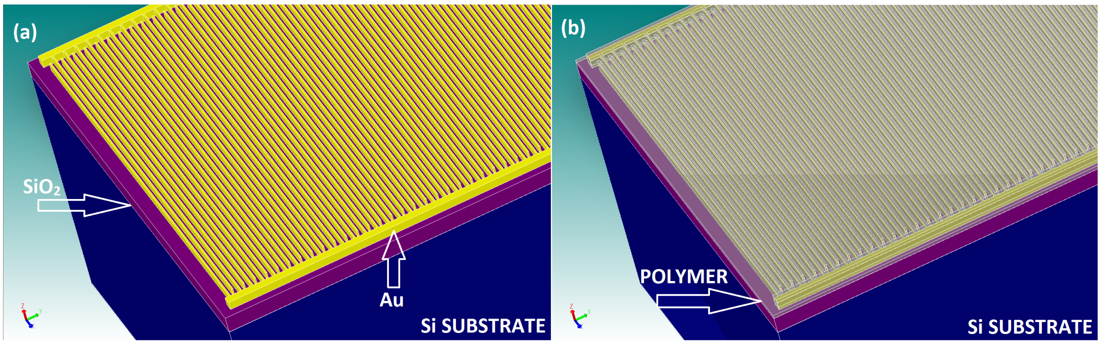

FIGURE 3.6: Model of IDE sensor for nanoscale analyte detection. (a) the 3D model of a device with only metal layer on top of SiO_2 layer, (b) the sensor with 20 nm of sensitive layer.

Parameter	**Value**	**Unit**
Finger length	50	μm
Finger width	200	nm
Gap between finger	500	nm
Electrode material	Au	NA
Electrode thickness	50	nm
Number of finger	100	NA
Oxide material	SiO_2	NA
Oxide thickness	100	nm
Substrate material	Si	NA
Substrate thickness	1.5	μm

TABLE 3.4: Parameters of nanoscale IDE capacitor used in biological sensing study.

is applied to solve for the admittance between the two electrodes. The quasielectrostatic solver is selected because biomolecular layer is considered as lossy dielectric, which has some finite conductivity. This lossy dielectric is not only described by permittivity but also the conductivity, which is frequency dependent. The quasielectrostatic solver calculates the conductance and the capacitance between two terminals of the sensor using the following equation:

$$I = YV = (G + j\omega C)V \tag{3.5}$$

where I,V are current and voltage difference between two terminals, $Y = G + j\omega C$ is the complex admittance between two electrodes of the sensor, G and C are conductance and capacitance respectively. From this admittance, the impedance can be obtained if desired.

The simulation is carried out over the frequency range from 1 to 20 GHz. The mesh setting for this simulation is shown in Table 3.5. At the end of simulation process, the MEMELECTRO module of CoventorWare outputs the values of complex admittance at different frequencies. From this data, conductance G and capacitance C are extracted from real and imaginary parts respectively. The result is summarized in Table 3.6

Layer	**x**(nm)	**y**(nm)	**z**(nm)
Substrate	250	250	125
Metal Electrode	250	250	50
Thin Oxide	250	250	50
Top dielectric	250	250	20

TABLE 3.5: Summary of mesh setting for nanoscale biological sensing study, mesh type is Manhattan bricks and element order is linear.

Freq(Hz)	$C_s(fF)$	$C_{ws}(fF)$	$G_s(nS)$	$G_{ws}(nS)$
10^0	64.99	53.29	0.0001	0.0000
10^2	64.99	52.56	0.0001	0.0000
10^4	64.99	52.56	0.0001	0.0000
10^6	64.99	52.56	0.0008	0.0003
10^8	64.99	52.56	0.0608	0.0263
10^{10}	64.99	52.56	4.9052	3.1640
2×10^{10}	64.99	52.56	12.5795	6.5512

TABLE 3.6: Frequency dependence of nanoscale IDE device: C_s and C_{ws} are capacitances of the sensor with and without sensitive layer and G_s and G_{ws} are conductances of the sensor with and without sensitive layer.

Figure 3.7 shows the plot of capacitance and conductance between the two terminals of the sensor for two different conditions: sensor is covered with 20 nm sensitive layer and sensor is with only air atop. For both cases, the sensor capacitance is almost constant over the entire frequency range. The capacitance of the sensor with sensitive layer is 10 fF higher than the capacitance of sensor without sensitive layer. This is equivalent to more than 20% increase in capacitance. Theoretically, this is a significant change, and therefore can be detectable with many available electronic systems. In practice, the parasitic effect of metal contacts and wiring may hinder the measurement. Nevertheless, this indicates a possibility of this sensor system to detect nanoscale analyte with the size in order of 20 nm.

While capacitance of the sensor is almost constant over the whole frequency range, for both investigated conditions, the conductivity of the sensor is dramatically changed when the frequency is higher than 100 MHz. The difference in conductance becomes more profound as the frequency increases to GHz range. When covered with 20 nm sensitive layer, the conductance of the sensor increases by 1.5 times at 10 GHz and by 2 times at 20 GHz. At these GHz frequencies, the change in conductance become more significant and hence greatly contributes to the overall admittance (or impedance) change of the sensor.

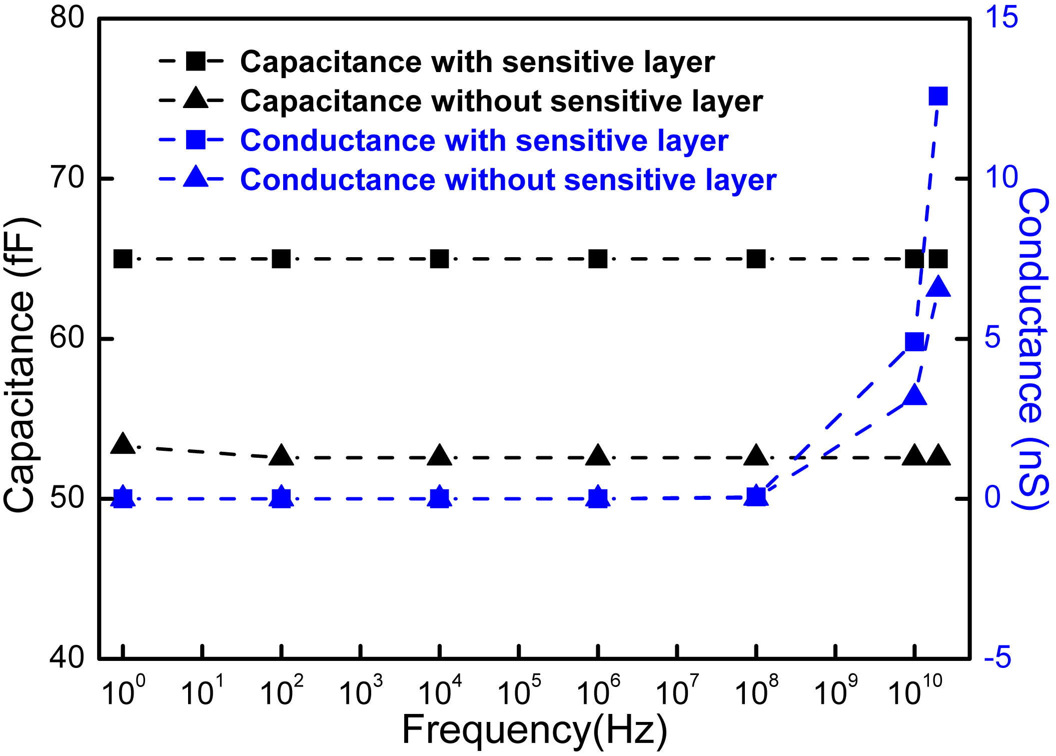

FIGURE 3.7: Capacitance and conductance of the sensor versus frequency. With a sensitive layer, capacitance increases more than 20% increase over the entire frequency range. The change in conductance is profound when frequency is above 100 MHz.

3.4 Conclusion

In conclusion, this chapter highlights various analytical models used to support the design of IDE capacitor structures which can be used in different applications. In addition, simulations are carried out using a commercial microsystems simulation package, CoventorWare, to demonstrate the potential application of IDE structure in energy harvesting and biosensing. For the energy harvesting application, a simulation conducted on a microscale IDE structure (area of 200 μm x 200 μm, finger width and gap between finger are 5 μm) indicates an approximately 5 times increase in capacitance of a variable capacitor when liquid dielctric (H_2O) is applied. In term of the sensing application, a simulation is performed on a nanoscale IDE structure (finger length is 50 μm, finger width is 200 nm, gap between fingers is 500 nm and the number of finger is 100). The result shows a 20% change in capacitance of the device over the entire frequency range (1 to 20 GHz) when a 20 nm sensitive layer is presented. Furthermore, as the frequency increases over 100 MHz, the change in conductance of the device also becomes more profound. The change in both capacitance and conductance indicates a potential for applying this sensing systems for nanoscale biomolecules detection when measurement is carried out at frequency higher than 100 MHz.

Chapter 4

Fabrication of Microsystems Devices

4.1 Introduction

The development of microsystems technology is highly related to the development of the IC technology. Therefore, majority of microsystems fabrication techniques are derived from IC fabrication processes, for example, photolithography and thin-film deposition. However, due to recent expansion in applications of microsystem, there are new methods and materials that are not common to the traditional IC foundries. The choice of the fabrication process and necessary equipments are dictated by the materials being used, the device geometry and the applications. Therefore, the processes to fabricate micro generator (used in Chapter 5) and nanoscale biosensor devices (used in Chapter 6) may be different even if they share the same IDE structure.

The first part of this chapter discusses briefly various fabrication techniques that are generally employed in microsystems fabrication processes. These include photolithography, electron beam lithography, electron beam evaporation, and etching. The rest of the chapter presents fabrication processes that are applied to build microsystems devices, including generator, sensor and resonator devices.

4.2 Microsystems based device fabrication techniques

Photolithography

Photolithography involves exposing a sample under ultraviolet (UV) light using a mask. Generally, the sample is first coated with a photoresist. There are two types of photoresists: positive and negative, as shown in Figure 4.1. For positive resists, the areas which are exposed to UV light will be removed after development. Meanwhile for negative resists, the areas which are not exposed to UV light will be removed after the development step. The coated sample is then exposed under UV light with appropriate dosage, which is determined based on the power of the UV source and the exposure time. Choosing the right exposure dosage is essential for obtaining desired patterns and usually requires optimization. After the exposure, the sample is then developed using a developer. The choice of developer depends on the resist type.

Typically, wavelengths of UV light sources are higher than 350 nm. Therefore, UV photolithography method cannot achieve patterns with small feature size. The smallest achievable feature size obtained from photolithography is generally higher than 1 μm. The advantage of photolithography process is the ability to achieve high throughput at low cost.

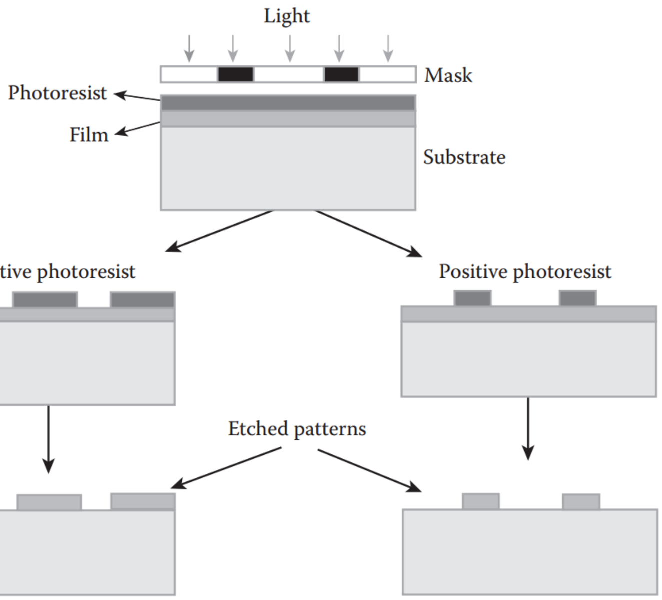

FIGURE 4.1: Photolithography with two different type of resists. Copied from [8].

Electron beam lithography

Electron beam lithography (EBL) is a direct lithography method in which a sample is exposed under a focused electron beam. To define a feature, which is smaller than a few hundreds of nanometers, it is not possible to use photolithography technique due to the large wavelength of UV light passing through the mask. In contrast to photolithography, EBL lithography does not require a mask. Instead, the sample is coated with an EBL resist, an electron-sensitive material whose solubility property changes according to the energy deposited by the electron beam, and then exposed directly under the focused electron beam. After exposure, the sample is also required to undergo a developing process. Commonly used EBL resists are Poly (methyl methacrylate) (PMMA) or Hydrogen silsesquioxane (HSQ), and ZEP. Similar to photolithography, an EBL lithography process also requires optimal dosage to achieve the best outcome. The parameters are critical in EBL process are beam current, beam spot size, beam step size and lens aperture size.

The EBL lithography technique, while it can overcome the limitation of photolithography in achieving nanoscale feature size, is still expensive. In addition, it is a low throughput exposure system due to the direct sequential scanning of an electron beam to obtain a defined pattern.

Electron beam evaporator

Thin film deposition is an essential step in microsystems fabrication process. Electron beam evaporator is one of the most widely used equipment to perform thin film deposition. It can be used to deposit various metals and oxides, such as gold, chromium, silicon dioxide, etc. It is a physical vapor deposition technique in which the deposition process is carried out within a vacuum chamber. The key components of a typical electron beam evaporator chamber is shown in Figure 4.2. Under an applied of high DC voltage, the tungsten filament will discharge electron. This electron beam is controlled by a magnetic field to hit the target material, which is placed in a crucible. The target material is then turned into a vapor phase and moved upward. If the shutter is released, the vapour will reach the sample surface and condense to form a thin film. Accurate deposition rate and thickness can be controlled and monitor by a quartz sensor inside the chamber. For metals such as gold and platinum, an adhesive layer (using titanium or chromium) should be deposited first to enhance the adhesion.

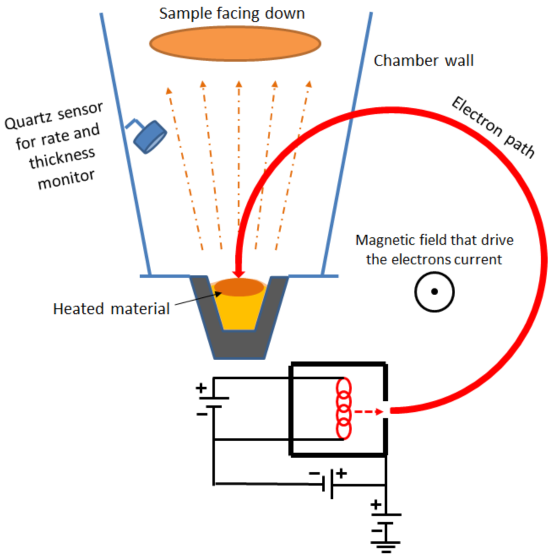

FIGURE 4.2: Schematic of a typical electron beam evaporating system.

Etching

Contrary to the material deposition process, which is used to deposit material on a substrate, etching process is utilized to remove a material so that a certain pattern can be formed. In microsystems fabrication, there are two types of etching: wet etch and dry etch. Wet etch involves using a chemical, such as sulphuric acid, hydrofluoric acid or metal etchants, to remove some parts of the target material. In a wet etch process, the sample is immersed directly in the etchant. The etch rate depends on the type of the etchant, concentration of the etchant and the material being etched. In a dry etch process, i.e. deep reactive ion etching (DRIE), the sample is placed in a high vacuum chamber and gas etchants are introduced. Factors affecting the dry etching process including the type of gases and their flow rates, chamber pressure, temperature, power and etch time.

4.3 Microscale IDE devices fabrication process

This section describes the fabrication process used to fabricate micrometre size IDE capacitors. These devices are used to implement the EMPG, which is thoroughly discussed in Chapter 5.

The fabrication process of these microscale IDE devices involves the creation of chromium mask using a laser ablation system followed by IDE patterning using photolithography process.

Chronium mask creation with laser ablation system

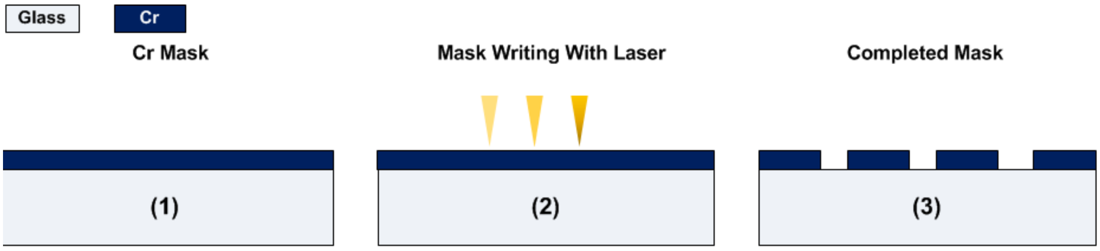

FIGURE 4.3: Process step for mask fabrication from laser ablation system.

Figure 4.3 outlines the mask creation procedure. Firstly, a glass slide is cleaned with acetone, isopropanol (IPA) and dried with a nitrogen gun. It is then placed in oxygen/argon plasma with 100 W power for 30 minutes to minimize contaminations. Electron beam evaporator (Intevac Nanochrome II model) is used to deposit a thin layer of chromium (100 nm). The lithographic features on the Cr coated slide are produced using a laser ablation system (SUSS SLP300 model). The areas without Cr allow UV light passing through while the areas covered with Cr prevent the substrate from being exposed. The opening areas define the structure of the IDE devices. This mask is used in the subsequent lithography step.

UV lithography process

Figure 4.3 summarizes the UV lithography process to create microscale IDE devices. The process starts with a cleaned glass slide. A thin layer of Cr (100 nm) is deposited on the slide using electron beam evaporator (step (2)), followed by photoresist coating (step (3)). Here, a low cost positive resist (AZ1512HS) is used. The resist-coated sample is spun at 3000 RPM (revolution per minute) for 1 minute to achieve a thickness of approximately 1.5 μm followed by soft-bake at 110^{o}C. The Cr mask is used in the next step (step (4)) to expose the resist-coated sample under UV light. A light source with 356 nm wavelength is exposed for 15 seconds at power density of 30 mW/cm^2. After the exposure, the sample is developed using AZ712 : H_2O (3 : 2) developer for 90 seconds then rinsed with deionized water and dried under a nitrogen stream (step (5)). Next, the sample, with the patterned resist as the mask, is undergone wet etching to remove the exposed Cr areas to form the IDE structures (step (6)). After all exposed Cr is etched, the sample is cleaned using acetone in an ultrasonic bath (step (7)). In order to isolate metal fingers and liquid dielectric, a layer of insulator is required. Here, TiO_2 is used instead of conventional SiO_2 due to its native hydrophobicity, which is highly desired for this type of device. Prior to the deposition of TiO_2, Kapton tape is used to cover metal electrodes (step (8)). An ALD system (Fiji F200 Cambridge Nanotech) is used to deposit 10 nm of TiO_2 (step (9)). Prior to measurement, the protective tape is removed.

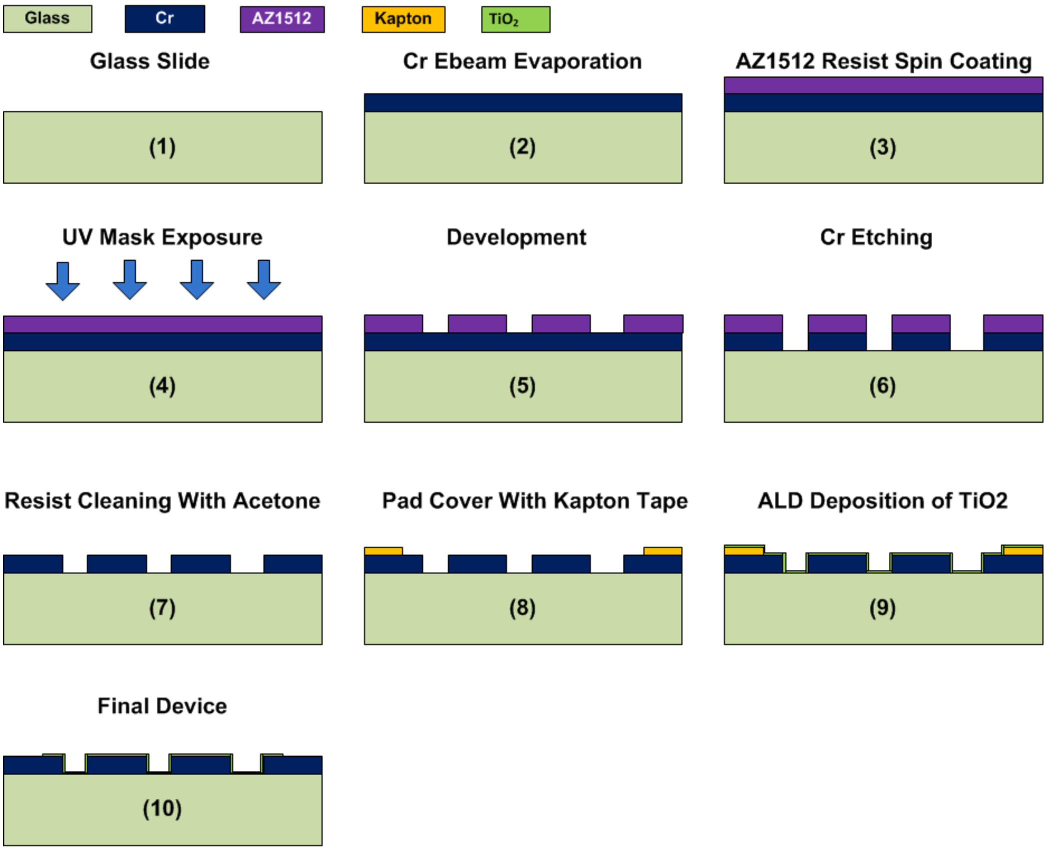

FIGURE 4.4: UV lithography based fabrication process for microscale IDE device, which is used in EMPG.

A typical device fabricated from this process is shown in Figure 4.5.

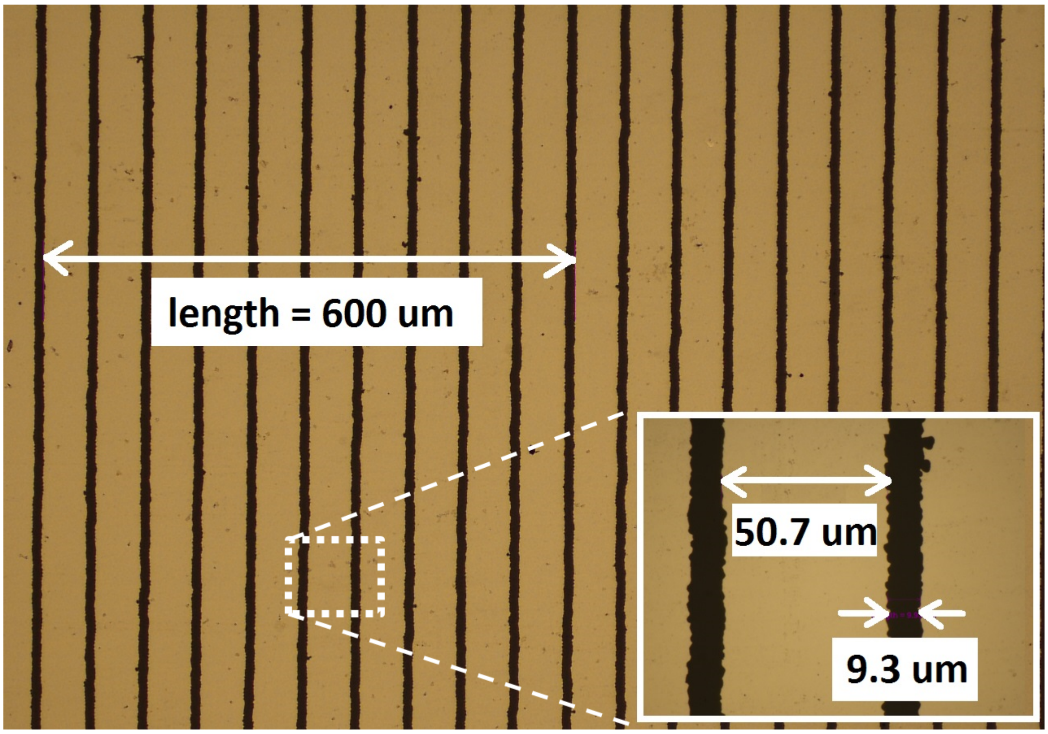

Figure 4.5: A typical microscale IDE capacitor fabricated with UV lithography and wet etch process.

4.4 Nanoscale IDE devices fabrication process

This section describes the fabrication process used to fabricate nanoscale IDE capacitors. These devices are used to implement an impedimetric biosensor system for detection of nanometre size biomolecule. A demonstration of such system is included in Chapter 6.

The choice of IDE geometry is highly dependent on the requirement of the sensors. These requirements might include sensor resolution, analyte concentration, physical size of analyte, measurement technique, etc. Therefore, the resolution of IDE structure can be as small as hundreds of nanometres or can be as large as tens of micrometres. Conventional IDE impedance based spectroscopy sensors have their finger size in micrometres range. These devices usually work well for large scale biological species or a large amount of sample with higher concentration range. However, in order to detect nanoscale biological agents such as antibody, protein or virus with low concentration and low sample volume, the dimensions of the IDE finger should be in nanoscale range. Conventional photolithography (such as the one discussed earlier in previous section) cannot achieve this target. To overcome this challenge, an alternative fabrication process is proposed, which is based on EBL lithography.

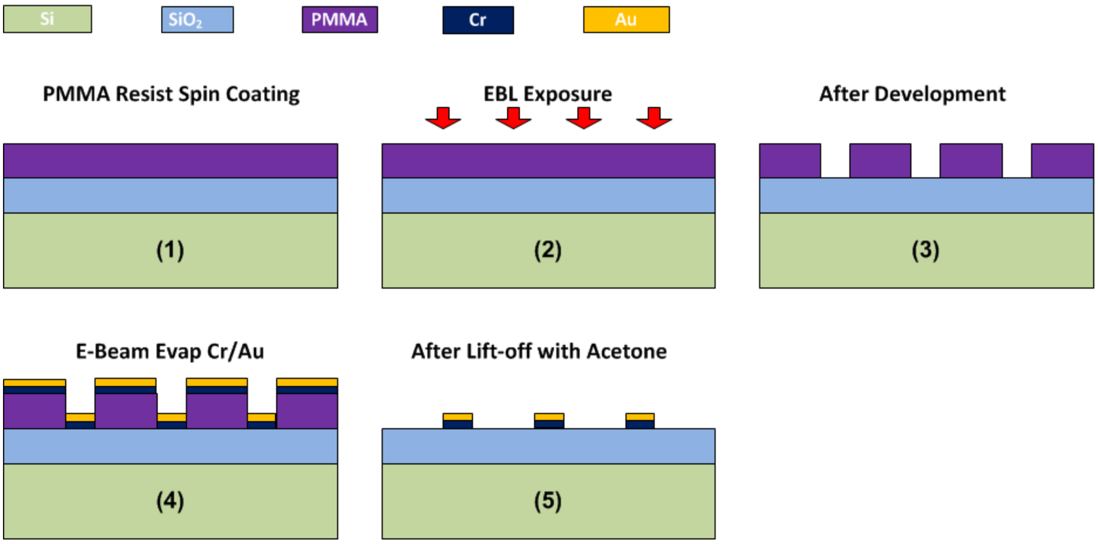

Figure 4.6: Fabrication process of nanoscale IDE devices using EBL lithography.

Figure 4.6 describes the fabrication process flow to fabricate nanoscale IDE structure using an EBL system. The process starts with a silicon substrate with thickness of 1 mm. This substrate serves as a support for the sensor platform. An appropriate choice of material is important to achieve good performance of the sensing system. Ideally, the substrate should have low dielectric constant to minimize its parasitic effect and the surface should be smooth to facilitate the fabrication of nanoscale features. Here silicon wafer is chosen mainly due to its readily available and low cost.

Prior to fabrication, the substrate is undergone a standard cleaning process to remove any contamination. After cleaning, a layer of 100 nm SiO_2 is deposited using Plasma-enhanced chemical vapour deposition(PECVD) system (Oxford PlasmaLab System 100 model). For patterning the nanoscale IDE structure, a lift-off process is preferred to a wet etch process due to its repeatability and hence a positive resist is used. Typically, positive EBL resists, which can achieve nanoscale resolution, include PMMA and ZEP. These resists have similar performance for the feature in order of hundreds of nanometre. Among them, PMMA has lower cost and hence it is preferred to ZEP. Giving the desirable finger's thickness of 50 nm, a layer of PMMA with thickness of 150 nm is deposited using a spin coater. The resist-coated sample is then baked at 170^{o}C for 5 minutes before being exposed using EBL system (Vistec EBPG5000PlusES).

After the exposure, the sample is developed using mixture of MIBK:IPA (3:1) for 60 seconds. The sample is then rinsed with IPA then dried under a nitrogen stream. E-beam evaporator is then used to deposit 5 nm of chromium (Cr) and 45 nm of gold (Au). The Cr layer is used to promote the adhesive of Au on SiO_2 surface. A lift-off process using acetone in ultrasonic bath is carried out to form IDE structures. The IDE devices are checked under optical microscope and scanning electron microscope (SEM) prior to performing electrical measurement.

A typical nanoscale IDE structure fabricated from this process is shown in Figure 4.7.

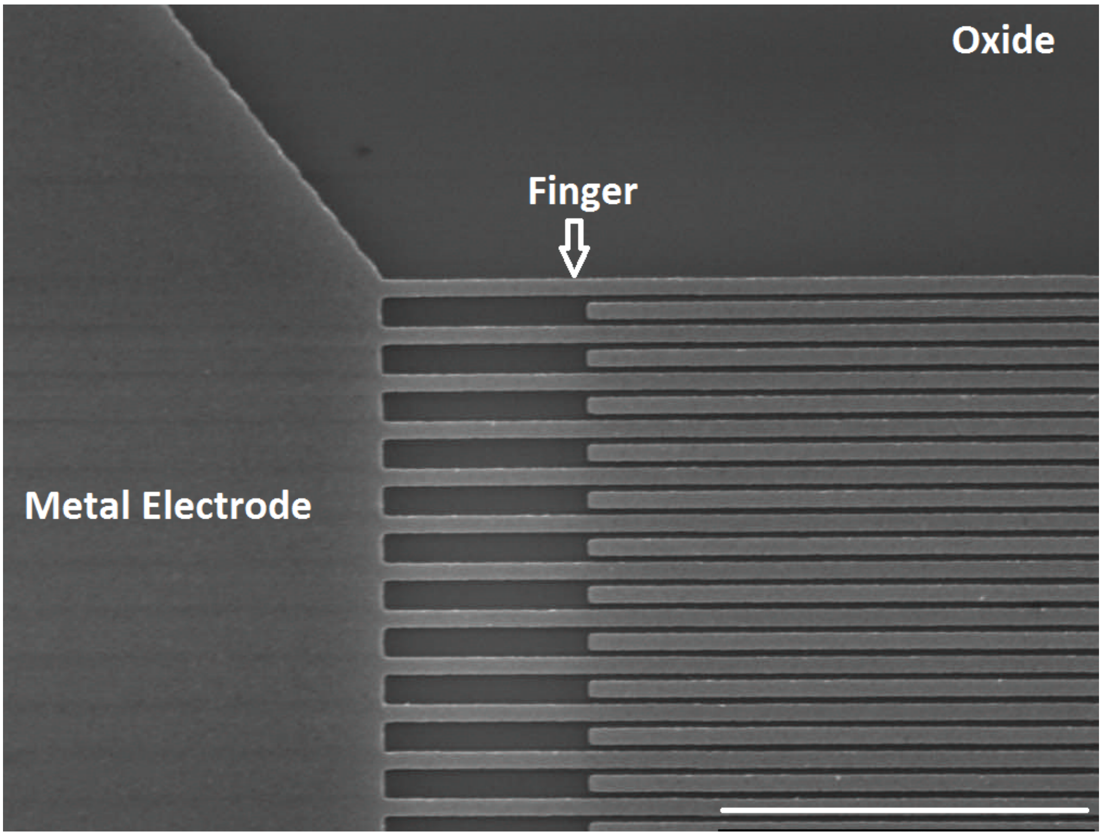

Figure 4.7: A typical IDE device after fabrication, the gap between finger is approximately 100 nm and the finger width is 200 nm, scale bar is 4 μm.

4.5 CMOS compatible fabrication process of nanoscale resonator

This section describes a CMOS compatible fabrication process of nanoscale resonator devices, which can be applied in various applications, including frequency reference and very high sensitivity mass sensing for single molecule detection. The target device is a free-free beam resonator structure. It is fabricated based on a Silicon-on-Insulator (SOI) wafer with the device and buried oxide thickness of 270 nm and 220 nm respectively.

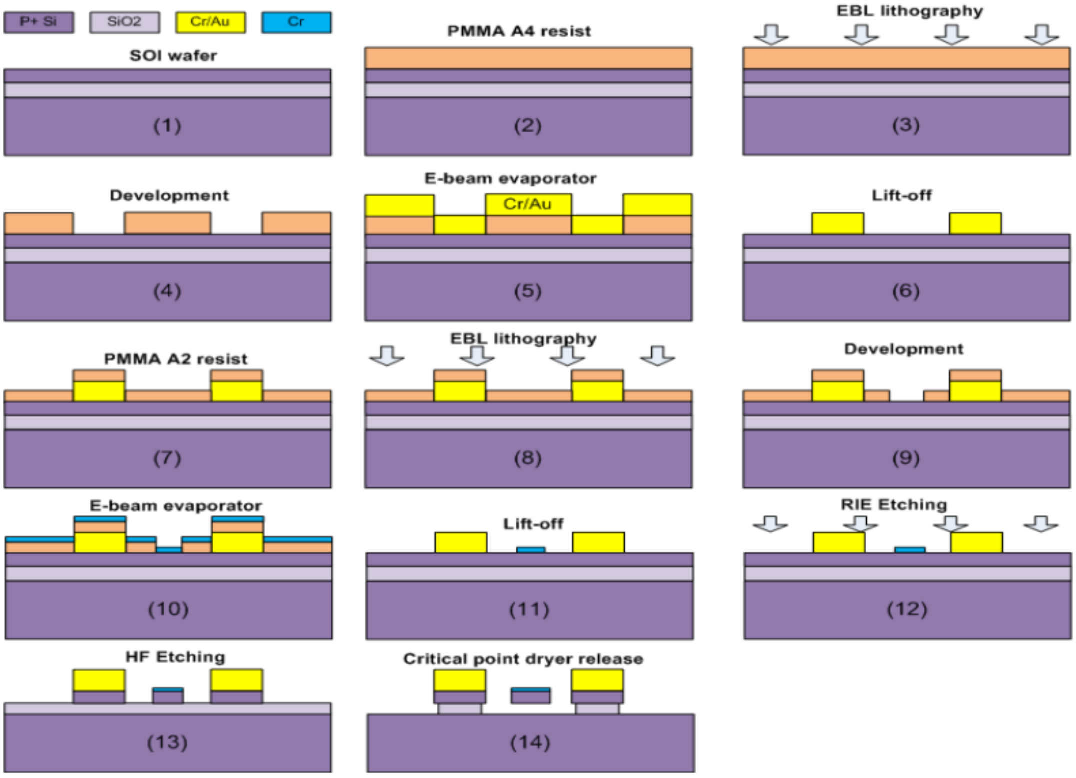

FIGURE 4.8: An overview of nanoscale resonator fabrication process.

Figure 4.8 shows an overview description of the process. It is a two masks post-CMOS process, which involves two EBL steps to defined masks. Following is the detail descriptions of critical steps of the process.

EBL lithography

The first step in the fabrication process flow is defining metal pads and interconnection. In addition, a set of markers need to be created for alignment of the next mask. The smallest feature size of marker and pads is 20 μm and the required thickness is at least 100 nm of metal (Cr/Au). To ensure a good lift-off, the resist should be at least 3 times thicker than the metal film. PMMA A4 resist with thickness of 330 nm is chosen for this step. After spin coating of the resist, the sample is undergone EBL exposure and developing. The metal layer (5 nm/95 nm of Cr/Au) is deposited using an e-beam evaporator. Finally, the sample is undergone lift-off to form metal markers and pads.

After the deposition of metal pads and marker, another EBL exposure is required to create the mask for the nanoscale device structure. The target device is expected to have its width of 250 nm and the gap of less than 100 nm. For a structure with this small feature size, a thin resist is required. PMMA A2 with thickness of 100 nm is chosen for this EBL step. A thorough study to determine optimal beam step size, beam current and dosage is carried out. A layer of 20 nm of Cr is deposited after EBL exposure to act as a mask for etching of silicon in the following step. Figure 4.9 shows the outcome of this fine feature EBL study. Figure 4.9(a) indicates the outcome of EBL exposure when non-optimal parameters are used. In contrast, when optimal parameters are employed, the feature and a gap that is smaller than 30 nm can be achieved.

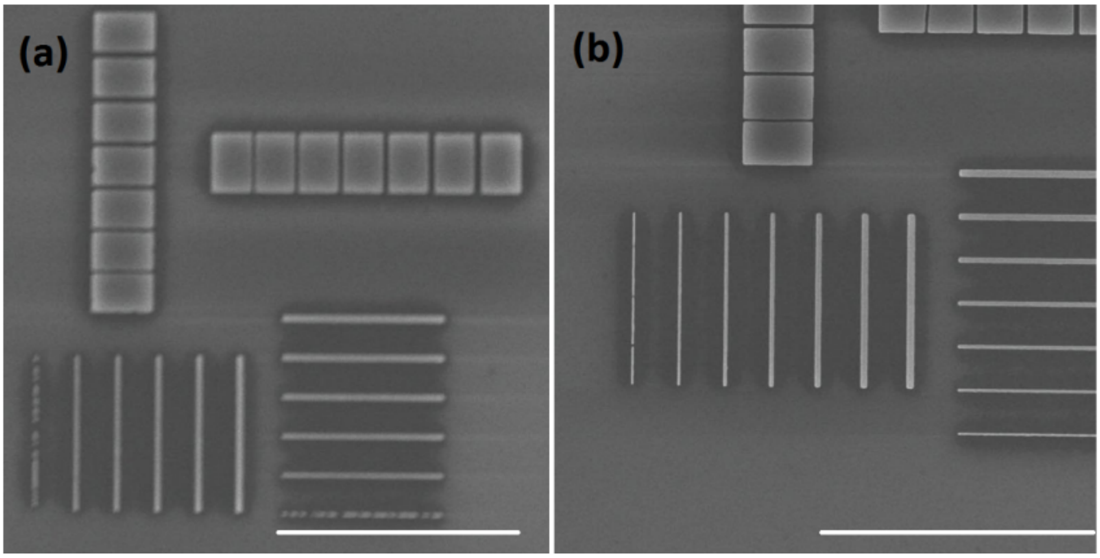

Figure 4.9: Outcome of a dose matrix study of sample, (a) shows outcome of non optimal parameter and (b) shows the outcome when optimal parameter is used, scale bar is 3 μm for both (a) and (b).

Reactive ion etching (RIE) of Si

After EBL exposure and Cr deposition to define the mask for fine feature beam resonator, sample is undergone etching to form Si beam structure. For this device, it is critical to achieve a smooth vertical sidewall structure with small gap; hence a pseudo Bosch with SF_6/C_4F_8 chemical was preferred to standard Bosch process. This etching process is also referred as mixed mode process in which etching and passivation are happening simultaneously. The key parameters for achieving ideal result are gas flow rates, ICP power, RF power, pressure, temperature of the chamber and etching time. Multiple iterations of etching experiments are carried out to obtain the ideal result. Figure 4.10 shows various results from these experiments.

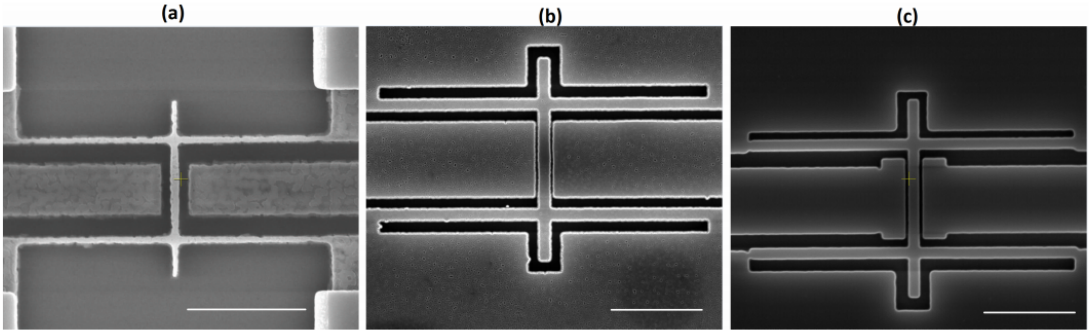

FIGURE 4.10: Study of reactive ion etching of Si, (a) shows a very bad result due to high flow gas and long etching time, (b) shows a better result and (c) shows the optimal outcome, scale bar is 2 μm for all (a,b,c).

SiO_2 wet etching and critical point dry

One of the most critical step of this fabrication process is etching of SiO_2 to release a suspended structure. Ideally, vapour hydrofluoric acid (HF) should be used. However, this capability is not available at local fabrication facility (MCN). Therefore, an alternative wet-etching using HF solution is employed. Typically the etching rate of SiO_2 depends on concentration of HF solution. Higher concentration of HF would increase etching rate but it is also difficult to control the stopping time. Figure 4.11(a) represents an example of some structures that are over etched. In this case, the entire structure is collapsed. On the other hand, very low concentration of HF would require a very long time to completely etch away SiO_2 under the structure. After multiple studies, 1% HF solution is chosen. Since the dimension of the device is very small, it would not be suspended if it is rinsed in DI water and dried with air directly. The strong surface tension of water would bend the structure down and permanently attach it to the substrate as shown in Figure 4.11(b). To resolve this issue, a critical point dryer is used. After performing HF etching, sample is rinsed with DI water and then quickly transferred to methanol. Following, sample is placed in critical point dryer to be critically dried. During this process, methanol is gradually replaced with liquid CO_2 before temperature is slowly raised to release CO_2. An example of suspended small structure after HF etching and critical point dry is shown in Figure 4.11(c).

Results

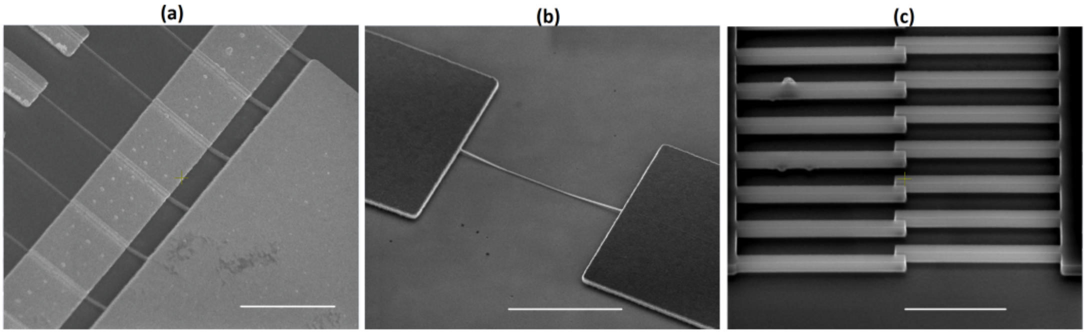

FIGURE 4.11: HF etching of SiO_2, scale bar (a) 2 μm, (b)(c) 3 μm.

After defining all optimal parameters for the entire process, a batch of free-free beam resonators is fabricated with thickness of 270 nm, width of approximately 225 nm and the length varies from 5 to 15 μm. Figure 4.12(a) shows a SEM image of a typical 5 μm length free-free beam resonator. A small gap of 50 nm with smooth and vertical sidewall is consistently achieved across most of the devices. Figure 4.12(a, b) shows a top view and a tilted view of an example of the devices.

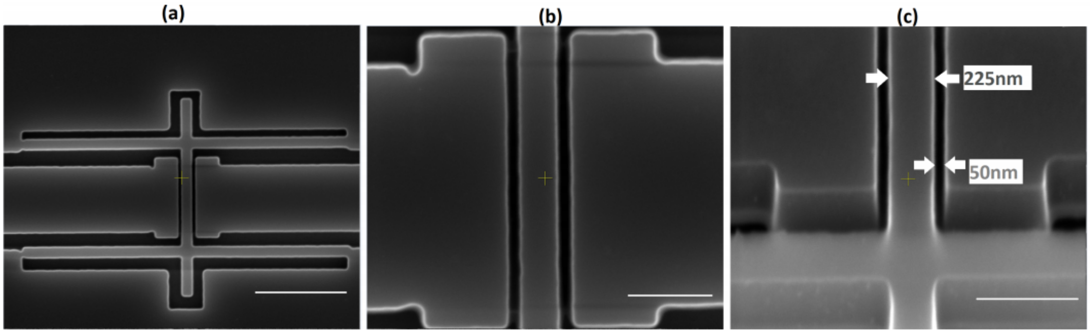

FIGURE 4.12: An example of prototype device, (a) scale bar is 2 μm, (b)(c) scale bar is 500 nm.

4.6 Conclusion

In conclusion, this chapter introduces the fundamental concepts related to microsystems fabrication technology, which include resist coating, mask creation, thin film deposition, and etching. The detail process flows and recipes, which are used to fabricate various devices from microscale to nanoscale, have also been proposed and discussed intensively. The devices fabricated from these processes have been utilized in a wide range of applications, such as micro energy harvesting, impedimetric based nano-biosensor and ultra-sensitive single molecule detection.

Chapter 5

Microsystems for Energy Harvesting

5.1 Introduction

There is a significant research effort focused on producing new higher efficiency and power density mechanical energy harvesting systems. Many small-scale prototypes have been demonstrated and there is great potential that these concepts may in the future be realized for large-scale energy harvesting. To date, the three most widely investigated mechanical energy harvesting methods are based on: piezoelectric [111, 115–118], triboelectric [110, 119, 120], and electrostatic [37, 38, 43, 121] principles. Piezoelectric and triboelectric generators are the most popular, with piezoelectric generators achieving power densities of $160Wm^{-2}$ [111] whilst triboelectric generators with power densities of $500Wm^{-2}$ [122] have been demonstrated.

Notwithstanding the exciting progress, there are some major drawbacks that have hindered the progress of electrostatic generators. These include the requirement for high bias voltages, some as high as many hundreds of volts [40–42], complex electrical circuits and high voltage device insulation required for safety in practical applications.The efficiency of the devices can also be limited as they can usually only harvest vibrational or kinetic energy along a single axes of motion. The vibration frequencies required to achieve acceptable power harvesting are very high, usually in the order of hundreds of

Hz to KHz [49–51], which makes them less than ideal for environmental power harvesting. In order to overcome these limitations, a new and highly innovative electrostatic harvesting liquid electrode device was proposed in T. Krupenkin and J. A. Taylor [123]. Unfortunately, the proposed liquid metal electrode was constructed from mercury, which is a highly toxic material with extensive evidence outlining mercury's deleterious effects on human health and the environment.

Here a new type of electrostatic generator is proposed. The proposed device utilizes a movable liquid electrolytic dielectric to create capacitance change. It not only takes advantage of the difference of dielectric constant of water versus air but also uses the free ions to generate a significantly larger capacitance change due to the formation of a Helmholtz double layer capacitor.

The ionic liquid electrolytic dielectric offers many desirable attributes. These include a flexible conformal material that is biocompatible, is abundant (seawater) and most importantly has a larger dielectric constant, much higher than air, resulting in higher energy harvesting capability. In addition, the device performance is further improved by facilitating the sliding motion of the ionic fluid over the electrode surface. This is done by depositing a thin layer TiO_2 over the electrode surface to increase surface hydrophobicity. The proposed device has significant advantages over traditional electrostatic devices in terms of cost, simplicity of fabrication, no requirement for any specific high cost packaging or vacuum shielding, and is environmentally friendly. Importantly, the prototype device possesses a very high surface charge density per conversion cycle of 3.8 mC/m^2 and achieves a figure of merit exceeding 10000 $\frac{10^8 \mu W}{(mm^2 Hz V^2)}$, which is two orders of magnitude greater than previously reported devices.

This chapter discusses the design, fabrication and characterization of an ionic liquid dielectric power harvesting generator device. Potential applications of this device are described, including harvesting energy from droplets (raindrops), hydro-power or water waves.

5.2 Principle of operation

Traditionally, electrostatic micro generator devices achieve changing capacitance by varying the gap or overlap area between two parallel plates of the capacitor. As shown in

Figure 5.1(a), the capacitance is maximized when the gap is smallest. In Figure 5.1(b), when an external mechanical force is applied, the gap between the plates is increased resulting in reduced capacitance. If the voltage applied to the two terminals of the variable capacitor is fixed (by external sources such as a battery, a pre-charged capacitor or other active circuitry), the change in capacitance during this transition will generate an electric current as indicated in Figure 5.1(c).

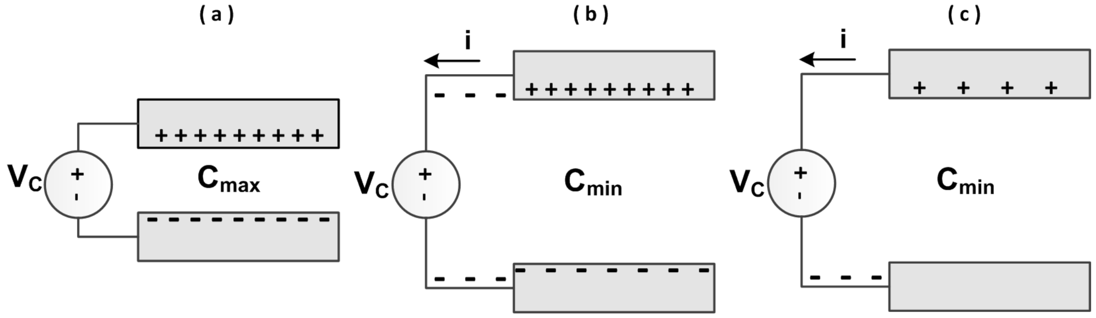

FIGURE 5.1: : Principle operation of a typical gap changing variable capacitor: (a) represents the situation when the gap is minimal and capacitance is maximal, (b)(c) describe the situtation when the gap is maximal and capacitance is reduced to the minimal value, electrons are transferred to maintain constant voltage and hence current is generated.

The total amount of energy produced over a cycle is equal to [2]

$$E_C = \frac{1}{2}V_C^2 \times (C_{MAX} - C_{MIN}). \tag{5.1}$$

Traditional microsystems structures used to create variable capacitor are shown in Figure 5.2. The detailed explanation of these structures can be found in Chapter 2. Based on equation 5.1, to increase the energy produced per cycle, a higher bias voltage or larger change in variable capacitance is required. In practice, it is difficult to achieve significant change in capacitance of these traditional variable capacitor due to the limitation in displacement of the solid parts. Therefore to increase generated power, higher bias voltages (V_C), up to 1000 V [41], are employed. This introduces many challenges in the electronic circuitry to manage such a high voltage. In addition, the fabrication process of these structures are relatively complex because it involves wet etching and releasing of suspended structures.

(a) In-plane overlap varying **(b) In-plane gap closing**

(c) In-plane variable surface **(d) Out-of-plane gap closing**

FIGURE 5.2: : Traditional microsystems structures used to create variable capacitor: (a) in-plane overlap varying, (b) in-plane gap closing, (c) in-plane variable surface and (d) out-of-plane gap closing. Adapted from [2].

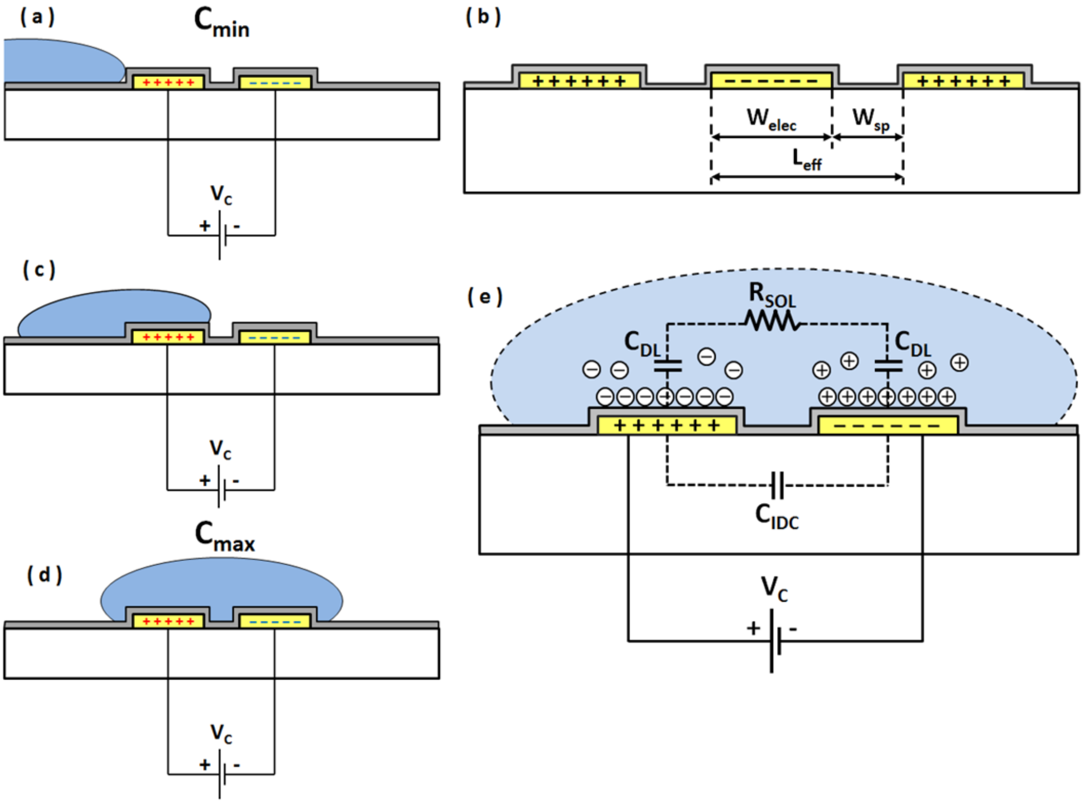

FIGURE 5.3: Principle operation of proposed device (yellow layer represents interdigitated metal fingers and grey layer represents oxide layer, (a)(c)(d) represents droplet (blue color) movement on hydrophobic surface during transition state,(b) indicates factors which affect geometric capacitance, (e) shows the double layer effect and its equivalent electrical model.

The new type of EMPG device proposed here is based on a lateral defined IDE capacitor structure and liquid dielectric. This device, while still based on the principle of variable capacitance, utilizes the displacement of a liquid dielectric rather than solid electrodes. The principle of operation of this device is described in Figure 5.3. Figure 5.3(b) shows the main factors affecting geometric capacitance of the device; these include electrode length, width, spacing between electrodes, dielectric constant of substrate and medium above the electrodes. Analytical expression relating these geometric parameters to capacitance can be found in Van Gerwen, P. et al. [4]. The addition of a hydrophobic oxide surface over the electrodes facilitates droplet motion. As can be seen from Figure 5.3(a) and (c), when the droplet is not over the surface of the electrodes, the capacitance is only due the interdigital capacitance. This corresponds to the minimum capacitance value C_{MIN}. Figure 5.3(d) illustrates the situation when a droplet is fully covering the electrode area. At this stage, the device capacitance is at its maximum value C_{MAX}. This change in capacitance is due to two factors. Firstly, the dielectric constant of the medium on top of the electrodes has increased significantly. For pure water at low frequency, its dielectric constant is approximately 78 times higher than that of the air [124]. Secondly, water droplets with dissolved salt (NaCl) contain charged ions. These ions accumulate at the interface of the metal electrodes and liquid electrolyte when a potential difference is applied. These layers of accumulated charge create an electrical double layer, which results in a significant, orders of magnitude, change in capacitance. Under a potential difference between two electrodes, positive ions are accumulated at the surface of negative electrode and negative ions are accumulated at the surface of positive electrode simultaneously. This capacitance due to charge separation can be modeled as a parallel plate capacitor with very small gap. An estimate of this capacitance can be obtained by [125]:

$$C_{DL} = \frac{S\epsilon_0\epsilon_r}{d} \tag{5.2}$$

where S is the area of electrodes that interface with the solution and d is the effective thickness of the double layer . This dielectric layer thickness is referred as the Debye length. The major factors that affect the Debye length are ion concentration, ion charge and temperature. For a specific ion at a certain temperature, a higher ion concentration will result in a smaller Debye length. Figure 5.3(e) shows the schematic concept of this double layer effect and its equivalent electrical model. In this model, R_{SOL} represents the series equivalent resistance of the double layer. This equivalent resistor also depends on ion concentration of the electrolyte, device geometry, and temperature [125].

5.3 Method

5.3.1 Device fabrication

The fabrication process of the proposed liquid electrolyte EMPG involved the following steps: Glass slides (Sail Brand) were used as the substrate layer and a quartz wafer was used to produce a mask. A thin film (100 nm) of chromium (Cr) was deposited on the glass slides and on the quartz wafer by electron beam evaporator (Intevac Nanochrome II model). The lithographic features on the Cr coated quartz mask were produced using laser ablation (SUSS SLP300 model).

To pattern the interdigital capacitor with a finger width of 50 μm and a finger gap of 10 μm, AZ1512HS resist was deposited on the slides, spun at 3000 rpm for 1 minute, resulting in a resist thickness of approximately 1.5 μm. The resist was exposed using the Cr coated quartz masks to UV light of 356 nm wavelength and power of 30 $mWcm^{-2}$ for an exposure time of 15 seconds. After exposure, the sample was developed for 90 seconds using AZ712 : H_2O (3 : 2) developer and then rinsed with deionized water and dried using a nitrogen stream. The slide was then wet etched using a Cr etchant to define the metal interdigital structure. The sample was then cleaned with acetone in an ultrasonic bath, rinsed with IPA and then dried with a nitrogen stream. In order to create the isolation between the metal fingers and the liquid dielectric, a layer of oxide was deposited. Kapton tape was used to cover the metal pads. A 10 nm layer of titanium dioxide (TiO_2) was deposited using atomic layer deposition (ALD) system (Fiji F200 Cambridge Nanotech). TiO_2 was chosen instead of conventional SiO_2 due to its inherit hydrophobicity [126]. An image of the fabricated device is shown in Figure 5.4. As can be seen from Figure 5.4(c), the edges of the fabricated devices are quite rough. This is because the mask was fabricated in house using our laser ablation system. Generally, at this resolution, if a commercial mask were used, one would expect a much sharper and cleaner edges.

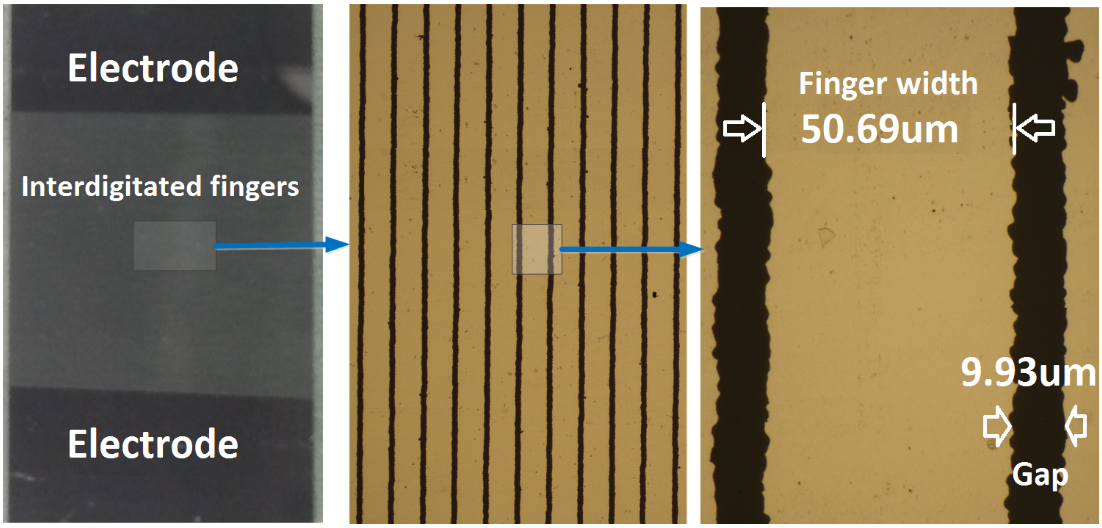

FIGURE 5.4: Image of a device after fabrication, (a) shows the device at large scale, (b) and (c) represent the interdigited finger with dimensions.

5.3.2 Measurement setup

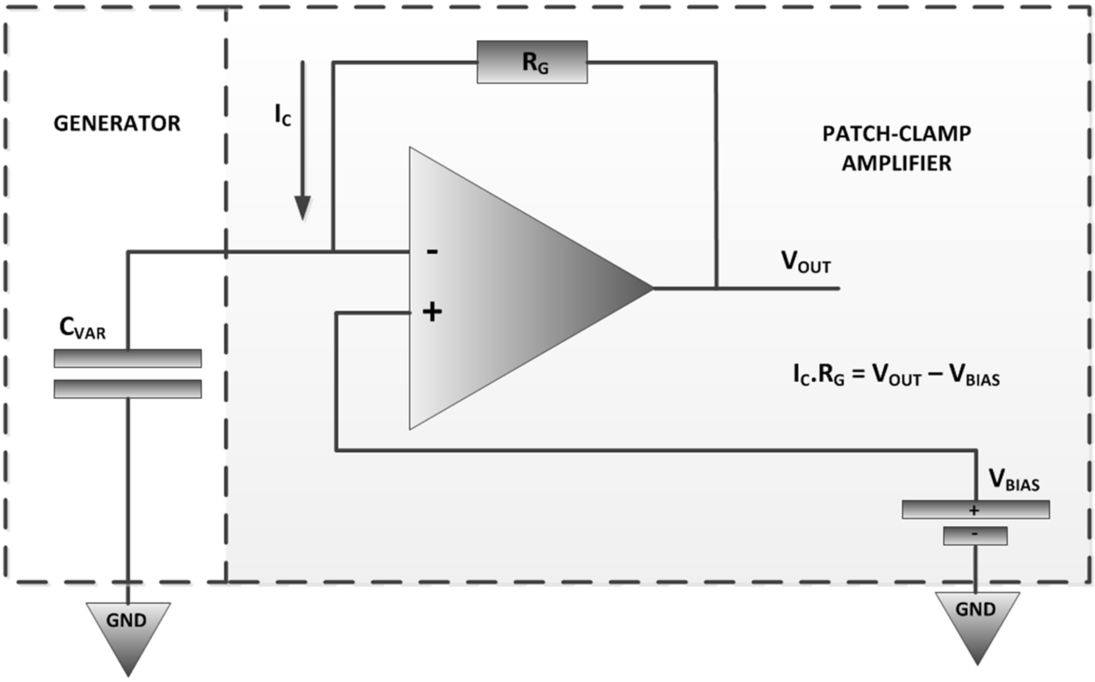

FIGURE 5.5: Constant voltage measurement setup: V_{BIAS} set a constant voltage between 2 terminals of the variable capacitor C_{VAR}, generated current I_C is converted to output voltage V_{OUT} by resistor R_G.

Figure 5.5 shows the schematic of a constant voltage measurement setup for our proposed devices. Voltage across two terminals of the variable capacitor C_{VAR} was fixed at V_{BIAS} by using a voltage-clamp amplifier circuit. The charge stored on this variable capacitor is equal to:

$$Q = C_{VAR}(t)V_{BIAS}. \tag{5.3}$$

Varying capacitance whilst keeping V_{BIAS} fixed results in the generation of current I_C. This current is measured using a trans-impedance amplifier which converts it to voltage using a resistor R_G.

5.4 Result and discussion

5.4.1 Constant voltage measurement using a patch clamp amplifier

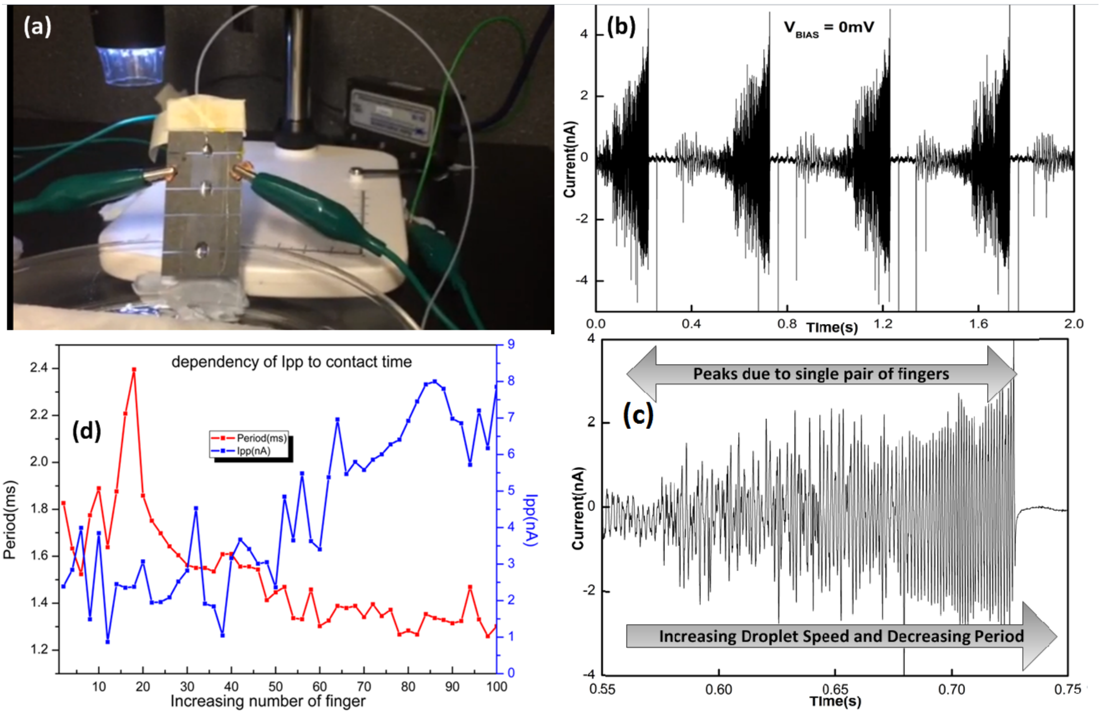

Figure 5.6: Measurement setup for sliding water droplet. (a) a typical test setup, (b) current generated when a droplet passing through the device at 0 mV bias voltage, (c) a closer look at the current generated, (d) the dependency of peak current on contact time.

Figure 5.6(a) illustrates a test setup used to verify the functionality of the device. The device was fixed at an angle of approximately 60^o. A Kd Scientific micro pump was used to generate small droplets of 18 MΩ water. The patch clamp amplifier (MultiClamp 700B model) was used to clamp the voltage and to monitor the generated current. As can be observed from Figure 5.6(b), current is generated when the droplet slides over the device and there is negligible current generated after droplet had passed over the effective area of the device. Figure 5.6(c) represents a magnified section of the output current which illustrates the current generated when the droplet was passing through each of the 50 μm pairs of fingers. The magnitude of peak current is increased as the droplet's speed is increased. As droplets travel across the fingers, the peak current generated is plotted in Figure 5.6(d). This graph indicates a strong inversely proportional relationship between the droplet sliding period and the amplitude of generated current. It is consistent with the equation that defines the generated current due to capacitance change, which is equal to:

$$I(t) = \frac{dQ}{dt} = V\frac{dC}{dt}. \tag{5.4}$$

The effect of bias voltage on device performance was also investigated by varying the bias voltage whilst other test conditions, such as droplet size and droplet speed, were kept constant. The measurements were performed for three different bias voltages (0 mV, 80 mV and 160 mV). The measurements are shown in Figure 5.7. As the bias voltage was increased, there was an increase in peak current generated, confirming that the magnitude of current generated depends on the bias voltage. From equation 5.4, one would expect the peak current is increased linearly as the bias voltage is increased. However, it is not the case since the capacitance (which is dominantly contributed from double layer effect) is nonlinearly dependent on bias voltage. In addition, as the bias voltage is increased, the effect of charge trapping on the oxide layer also becomes more significant.

5.4.2 A potential application of the device in large scale environmentally friendly energy harvesting

A promising application of the proposed device is harvesting energy from liquid droplets. Liquid droplets are abundant in our environment. They can be freely available such as rain drops or can be easily formed in a marine environment by exploiting water waves or from a prefilled water reservoir. The concept of how water droplets are formed for practical applications is outlined in Figure 5.8 (b) and (c).

Figure 5.8(a) indicates details of an experimental setup for harvesting energy from the droplets. The energy harvesting device was placed at a distance of 450 mm below the

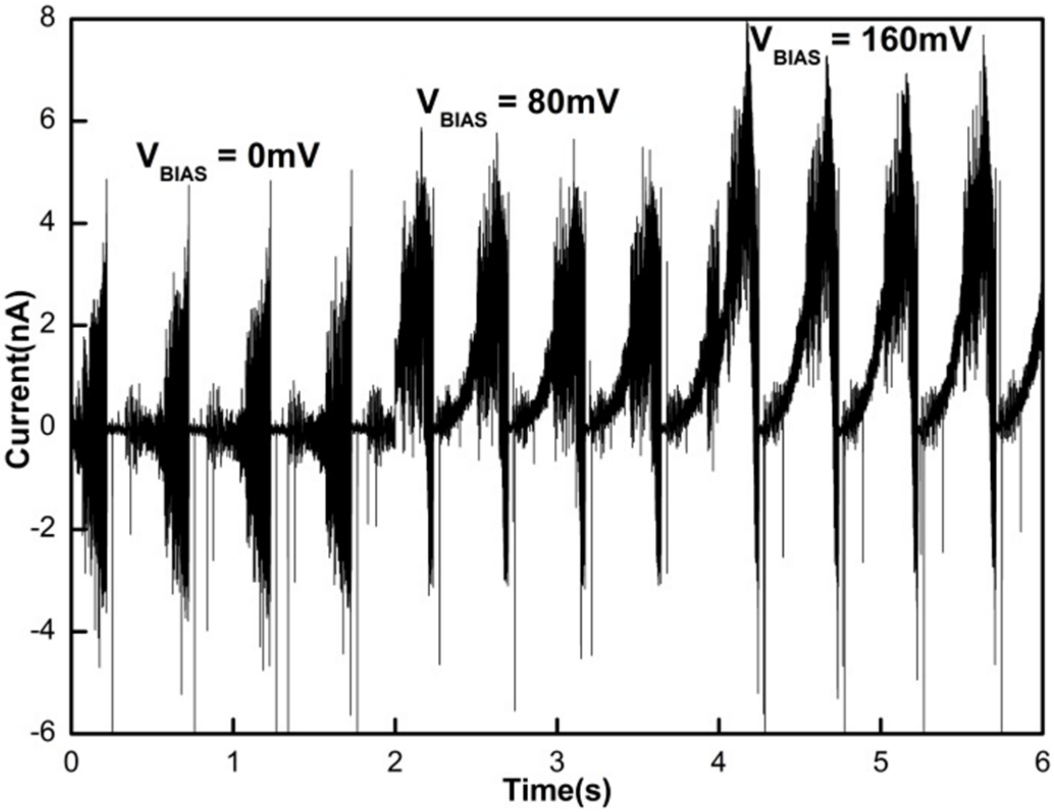

Figure 5.7: Dependency of output current on bias voltage. Peak current is lowest at 0 mV bias voltage and it is increased at 80 mV and 160 mV bias voltage.

drop generating tube. The bias voltage was set to be at 1.2 V. The gain-setting resistor was selected to be 1.8 $M\Omega$. A micro pump was used to generate droplets. The flow rate was 6 mL per minute with an average of 6 droplets per second resulting in a drop volume of 16.7 μL. The droplet formed a circular contact surface with the device. The diameter of the droplet was found to be 3 mm, hence the effective surface area is approximately 7 mm^2.

Figure 5.9 summarizes the experimental results. The generated current is shown in Figure 5.8(a). Current generated from milliQ water droplets, which have very low ion concentration, and droplets with 500 mM NaCl, which have similar concentration to seawater, are overlaid on the same graph for comparison. Current generated varies significantly depending on ion concentration. The peak current observed was approximately 2 μA for the 500 mM NaCl droplets. Figure 8(d) shows the corresponding current density per surface area of the device. The peak current density of approximately 250 mA/m^2 is achieved for a 17 μL droplet of 500 mM NaCl. Comparison is shown in table 5.1.

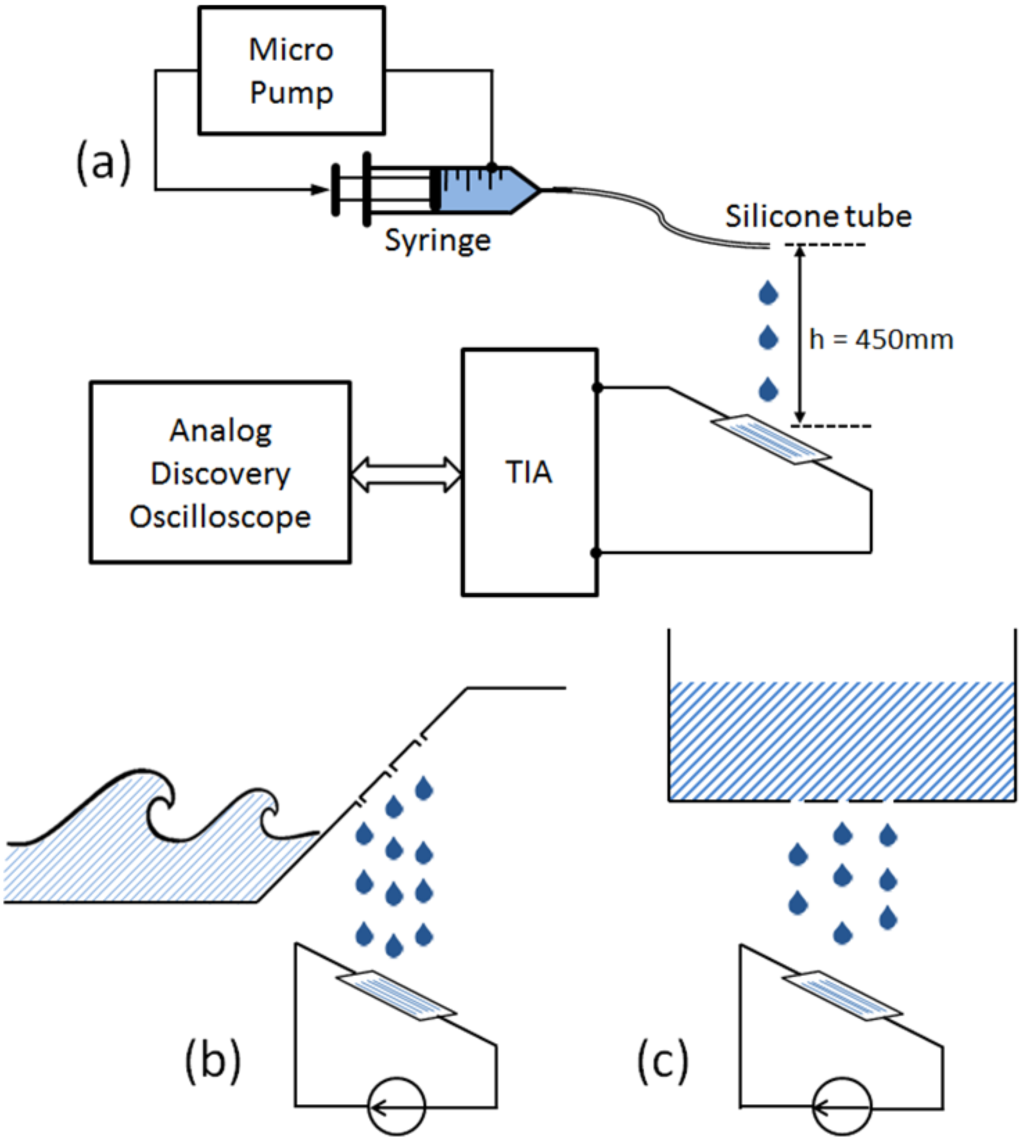

FIGURE 5.8: (a) Measurement setup for a potential application of the device and concepts of generating droplets from water wave (b) and from a water reservoir (c).

To estimate average energy and power generated, the charge generated over 10 s was integrated. This result is shown in Figure 5.9 (c). The average charge generated for milliQ and NaCl solution (500 mM) were 55 nC and 160 nC per second respectively. For droplets with 500 mM NaCl the equivalent surface charge density per conversion cycle is $(160nC)/(6 \times 7mm^2) = 3.8mC/m^2$. And the peak power density is 357 mWm^{-2} when operated at a bias voltage of 1.2 V. Although the output power (Figure 5.9(b)) is lower compared to other electro-static generator devices it is important to emphasize that a much lower operating voltage is used here. To evaluate and compare device performance the figure of merit (FOM) proposed by Basset, P. et al [51] is used. This FOM is defined as:

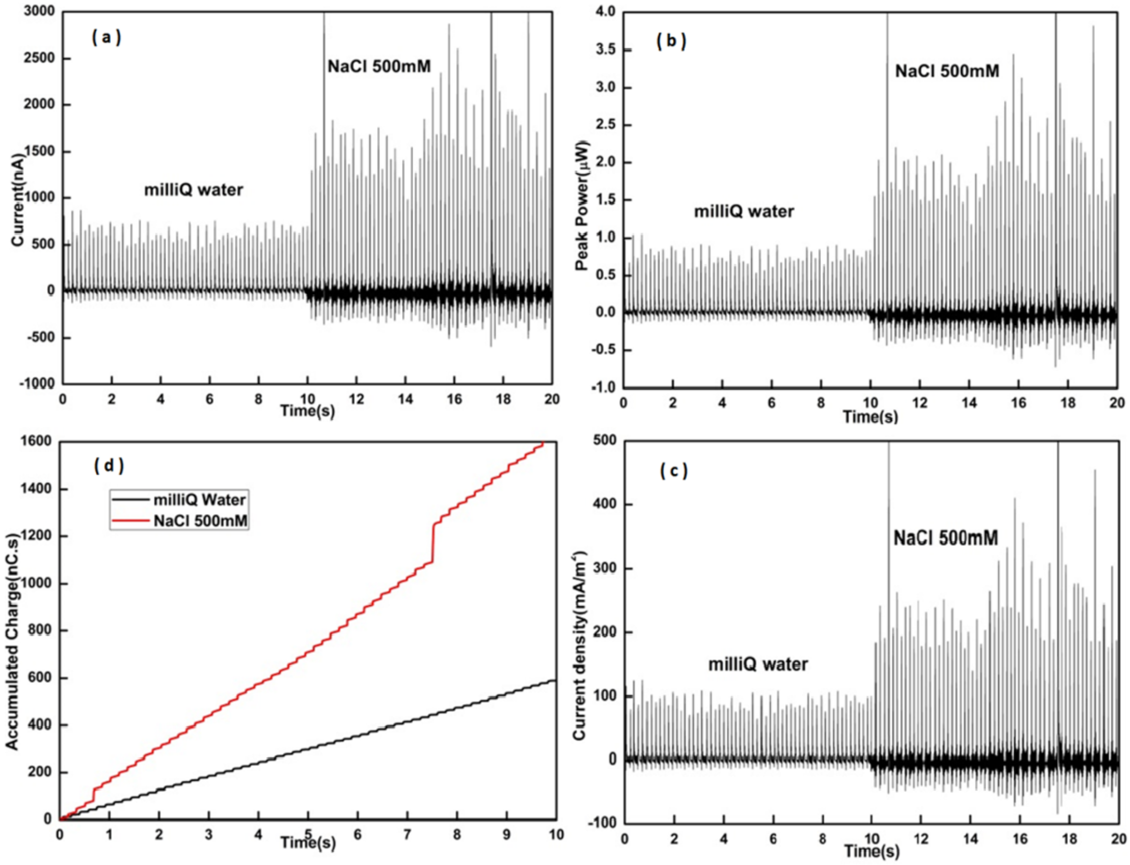

FIGURE 5.9: (a) Peak current (in nA) generated from two different types of droplets (milliQ water and NaCl), discontinuity at 0.5 s and 8 s on NaCl charge curve is due to some abnormal spikes of current generated (b) Peak power (in μW) associated with current generated (c) Current density (in mA/m^2) (d) Accumulated charge generated over 10 s (in nC).

Reference	Year	Current Density (mA/m^2)
Moon et al [127]	2013	6.4
Kwon et al [112](drop)	2014	328.9
Kwon et al [112](pushing/releasing)	2014	81.3
Lin et al [110]	2015	26.3
Lin et al [128]	2014	15.0
Cheng et al [129]	2015	31.8
This work	2015	250

TABLE 5.1: Current density of this work in comparison to previous works that harvest energy from water droplet

$$FOM = \frac{P}{V_C^2 \times f \times S} \tag{5.5}$$

where P is the converted power (in μW), V_C is the maximum voltage applied to the variable capacitor (in V), f is operating frequency (in Hz) and S is device area (in mm^2).

The results, shown in table 5.2, indicate that our proposed electrostatic generator has a two orders of magnitude improvement over previous devices.

Reference	Year	f(Hz)	S(mm^2)	V_c(V)	P(μW)	FOM ($\frac{10^8 \mu W}{(mm^2 Hz V^2)}$)
Despesse et al [121]	2005	50	1800	120	1050	81.02
Yen et al [49]	2006	1560	4356	6	9.74	3.98
Tsutsumino et al [41]	2006	20	200	950	37.7	1.04
Ma et al [130]	2007	4100	25.9	15	0.065	0.27
Suzuki et al [131]	2008	37	234	450	0.28	0.02
Basset et al [51]	2008	250	66	8	0.061	5.78
Hoffmann et al [50]	2008	1460	30	50	3.8	3.47
This work ($500mMNaCl$)	2015	6	200	1.2	0.192	11111.11
This work (milliQ water)	2015	6	200	1.2	0.066	3819.44

Table 5.2: Figure of merit of this work compared to some previous works on electrostatic generator devices

5.5 Factors that affect the performance of the proposed EMPG

Our device possesses very high surface charge density per conversion cycle and there is a great potential for boosting the output power. Here we discuss on some key factors that affect the amount of energy produced and how output power can be improved.

Electrolyte concentration

Equation 5.1 describes the principal factors that govern the amount of energy produced by a constant voltage electrostatic generator. At a certain bias voltage V_{BIAS}, the produced energy is directly proportional to the capacitance change. From the model shown in Figure 5.3(e), this capacitance change depends on geometric capacitance C_{IDC}, double layer capacitance C_{DL} and its equivalent series resistance R_{SOL}. While electrolyte concentration has minimal effect on the geometric capacitance, it substantially affects C_{DL} and R_{SOL}. Hence a higher concentration electrolyte will create a larger overall capacitance change due to a decrease in R_{SOL} and an increase in C_{DL}.

Bias voltage

From Equation 5.1, the amount of energy produced is directly proportional to V_{BIAS}^2. Hence, an increase in V_{BIAS} will significantly improve the output power of the proposed device. If the bias voltage is increased to 24 V, which is 20 times higher than our test condition, the output power could increase by 400 times. However, a higher bias voltage requires a thicker insulation layer which will reduce the change in capacitance. To increase the bias voltage of the device while still maintaining the total capacitance change, a low dielectric constant and higher breakdown voltage material can be used.

Structural dimension and surface area of the device

Reducing electrode and gap dimensions and increasing the total surface area of the device will also significantly increase the capacitance change, which leads to an increase in the output power. Currently, the prototype device has finger width of 50 μm and electrode gap of 10 μm. These dimensions can be further reduced without increasing the complexity and the cost of fabrication process. Shim et.al [132] recently has reported a cheap and reliable technique to produce large area interdigital capacitors with finger gap less than 500 nm using conventional lithography process. If the device dimensions can be reduced to 2.5 μm finger width and 0.5 μm gap, the capacitance due to its geometry could be improved by 20 times. In addition, the fabrication process can be slightly modified to increase the total surface area of the device. Prior to deposition of metal on substrate, nano-imprinting can be used to increase nanoscale surfaces roughness. Using nano-imprint technology, nano structures with resolution smaller than 10 nm has been reported [133]. Assuming a nano-imprint mould with a pattern of 50 nm square and 100nm height is deployed. For every 1 μm^2 area, there will be 100 nano patterns and therefore the new total surface area will be $(1 + 100 \times 0.05 \times 0.10 \times 4 \times 100 = 3\mu m^2)$, which is equivalent to a three times increase in the total surface area. Both the geometric capacitance (C_{IDC}) and double layer capacitance (C_{DL}) of the equivalent model described in Figure 5.3(e) are dependent on the surface area of the device. Therefore, the total equivalent capacitance of the device will be significantly increased because of an escalation of the total surface area.

Contact time

By using nano-imprint to predefine surface roughness, the droplet contact angle will also be increased, and the droplet sliding angle will be decreased [134] [135]. This will lead to shorter contact time of the droplet on the device surface and hence the generated current will be increased.

Optimal load value

Further experimentation was carried out to investigate the effect of load on the power generated. Matching between the load and the device impedance will produce maximum output power. In this experiment, the load resistor was varied from 110 KΩ to 3.9 MΩ. MilliQ water (18 MΩ) droplets were used for this experiment, with a drip rate of approximately 7 droplets per second and bias voltage, applied on variable capacitor, was set at 2 V. Figure 5.10 summarizes the test results. Figure 5.10(a) represents the total amount of charge generated over period of 5 seconds. Figure 5.10(b) shows the estimated average power generated from this generated charge. This result highlights that the output power of the device is load dependent. The output power for varying loads can differ by a factor of 5 times. Therefore, by carefully optimizing the load conditions, the output power of this generator can be substantially improved.

5.6 Conclusion

This chapter demonstrates a great potential of the new type of EMPG device. This device converts mechanical energy into electrical energy by utilizing movable ionic liquid electrolyte as the dielectric. It offers many advantages over traditional electrostatic generators. It exhibits large capacitance change due to the electrical double layer effect formed by ion separation and voltages applied at the electrodes and high dielectric constant of water. The achieved surface charge density and current density are favorable when compared to previously reported electrostatic generators. The fabrication process of this device only involves conventional lithography step, which is cheap, scalable to macro size and does not require any high cost packaging or vacuum shielding. A peak

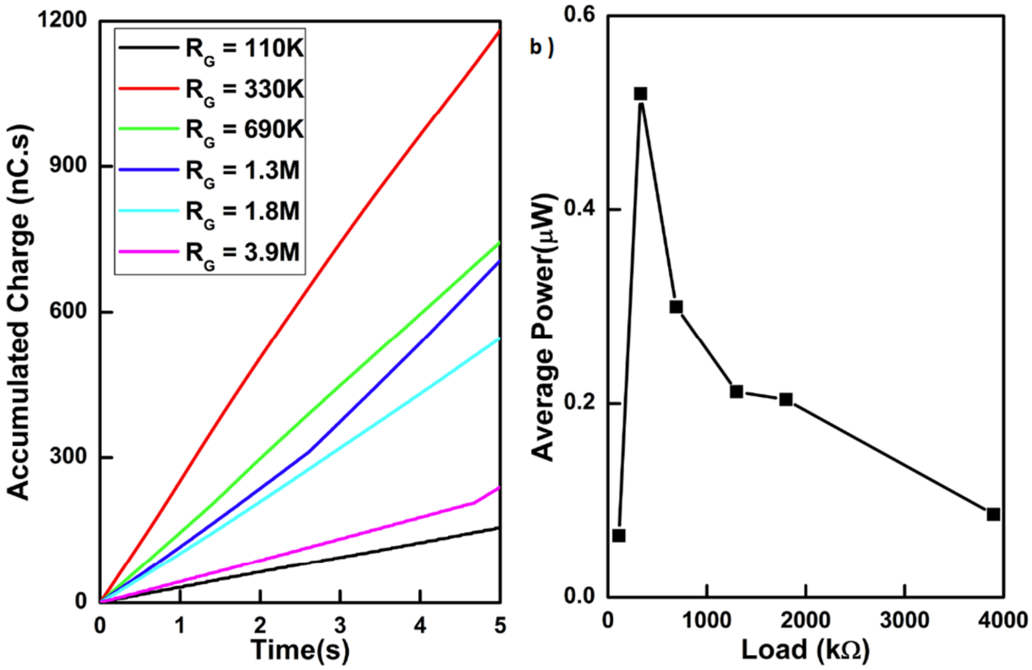

FIGURE 5.10: Load dependency of the device (a) Accumulated charge over 5 seconds per different load (b) Average power generated for milliQ water droplet at different load condition with $V_C = 2.0$ V.

current density of 250 mA/m^2 and FOM more than 10000 $\frac{10^8 \mu W}{(mm^2 Hz V^2)}$ have been demonstrated for a prototype with electrode width and gap of 50 μm and 10 μm respectively operating at 1.2 V and a droplet dropping rate of 6 Hz. The experiment demonstrates a novel concept of an electrostatic generator device that can be used to harvest many widely available sources of (ionic) saline water droplets.

Chapter 6

Nanoscale IDE Sensor for Glioma Detection

6.1 Introduction

The development of miniaturized biosensors using microsystems technology has increased significantly recently. Among many different detection methods, which have been discussed in Chapter 2, the impedemetric detection technique based on nanoscale IDE structure is widely adopted due to its simplicity in fabrication, integration and high sensitivity. This chapter discusses the application of such systems to detect glial fibrillary acidic protein (GFAB) antibodies.

A glioma is a tumour that is produced from glial cells of human brain and nervous system. It is known as the most common primary brain tumour. Its early detection is still a challenge. Autoantibodies against GFAP have shown the highest differential expression compared to other glioma expressed antibodies. Today, imaging-based methods are used for disease detection and treatment management [31]. Imaging based methods are time-consuming, expensive, and not conducive to large scale screening which is necessary to assist with early stage diagnosis [31] and in the day to day management of patients receiving treatment. A low cost, fast and easy to use method for screening and ongoing management is required. GFAP and Interleukin 6 (IL-6) expression has been widely detected in glioma patients [33, 34, 136, 137]. It has been reported that GFAP antibodies can be used as a biomarker for early detection glioma, since tumours elicit an antibody response before clinical signs manifest and express in low-grade gliomas even those with undetectable GFAP proteins [31].

Research utilizing laboratory based techniques such as western blot and enzyme-linked immunosorbent assay techniques to detect GFAP antibodies have been previously reported [31, 138]. To date, point of care biosensors, which can accurately quantitate concentrations of GFAP antibodies, have not been reported. In this chapter, an immunoassay based dielectric biosensor is developed to provide fast, easy to use, low-cost and real-time detection of GFAP antigen-antibody binding. The proposed sensor can be used to characterize GFAP antibody concentrations in patient samples.

Dielectric sensors detect concentrations of molecules by measuring changes in the impedance of the sensors [139, 140] and have the additional advantage that they permit compact sensors to be implemented as part of integrated on-chip systems [141, 142]. Planar interdigital dielectric sensors have demonstrated a high sensitivity to target molecules [35, 143–152]. Recent studies on both label (gold nano-particles) and label free detection of antigen-antibody binding using interdigital dielectric sensors have shown a detection limit of 10 pg/ml [143] and 25 pg/ml [35], respectively (Table 6.1).

Target Analyte	**Limit of Detection**	**Reference**
Hepatitis B surface antigen	10 pg/ml	[143]
C Reactive Protein, $TNF\alpha$, IL6	25 pg/ml	[35]
C Reactive Protein	100 ng/ml	[146]
IL6, CEA, hEGFR	20 pg/ml	[147]
C Reactive Protein	25 ng/ml	[148]
Hevein allergenic protein	10 ng/ml	[149]
Anti-HRP, Anti-Hep B	100 pg/ml	[150]
Goat anti-bovine IgG Ab	10 ng/ml	[151]
ST2 antigen	40 pg/ml	[152]
GFAP antibody	2.9 pg/ml	This work

Table 6.1: Comparison of the limits of detection of various IDE impedimetric biosensors.

Here, a wideband measurement technique utilizing an interdigital coplanar waveguide sensor (ID-CPW), which consists of a coplanar waveguide (CPW) and interdigital electrodes (IDE), is proposed. An equivalent circuit model for the sensor is derived, which is decomposed into a capacitive and resistive component. The wideband measurement coupled with the model based capacitance estimation allows for greater detection sensitivity. To demonstrate the sensor's performance, the proposed sensing system is used to detect antibodies against an intermediate filament protein expressed in astrocytes cells in the central nervous system, GFAP [138] . The total astrocytic protein extracted from human foetal astrocytes was immobilized on the sensor surface. The GFAP antibodies at varying concentrations were introduced to verify the binding of GFAP antibodies to astrocytic protein and the detection performance of the sensor. The proposed method also uses secondary antibodies to increase the sensitivity of the sensor at lower concentrations (< 5 pg/mL) of primary antibodies (GFAP antibodies) via amplification of the initial primary binding event by secondary antibody conjugation.

This study demonstrates that GFAP bonded ID-CPW is highly sensitive in detecting anti-GFAP antibodies to a concentration of 2.9 pg/mL, equal to or exceeding the limits of conventional immunoassay techniques. Here, the capacitance change resulting from antigen-antibody binding is measured in both dry and wet environments. An important point of differentiation in our approach is that high excitation frequencies (1-25 GHz) were used to measure changes in sensor capacitance. The high frequency excitation was chosen such as to counteract the large capacitances observed at lower frequencies because of Helmholtz layer formation and electrode polarization.

This chapter describes the design and optimization of ID-CPW using electromagnetic software, a model to obtain the impedance of interdigital electrodes, and the fabrication process of the sensors. The protocol for functionalizing the sensor surface and protein immobilization is also included. The experimental measurement setup and the results are intensively discussed. The chapter concludes with summary remark to highlight key achievements of this study.

6.2 Design and fabrication of ID-CPW

6.2.1 Design of the ID-CPW using Electromagnetic (EM) Simulator

The ID-CPW, shown in Figure 6.1(a), comprises of a CPW and IDE. The substrate was chosen as Si, and a layer of SiO_2 was evaporated on. The dimensions were miniaturized so that the sensor was suitable for implementation as a system on a chip. The relative dimensions of the CPW were designed to match the characteristic impedance of 50 Ω. The thicknesses of the Si substrate, SiO_2 and metal layer (Cr/Au) were 1 mm, 100 nm and 50 nm, respectively. The length of the CPW was 200 μm, the width of the IDE was

200 nm, gap between electrodes was 500 nm, length of the electrode was 50 μm and the number of electrodes was 99. Verification of the design parameters was performed using a full wave simulation, Ansoft's HFSS.

6.2.2 Model of the ID-CPW

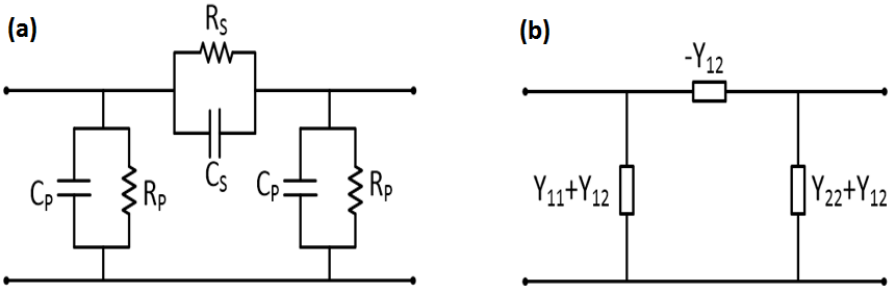

FIGURE 6.1: Lumped circuit model of ID-CPW. The capacitance and resistance of the IDE are C_s and R_s. The parasitic capacitance and resistance of the sensor are C_{pi} and R_{pi}, where i = 1 and 2. The admittance parameters are given by Y.

A model for the ID-CPW is shown in Figure 6.1. The parasitic capacitance and resistance of the sensor are C_{pi} and R_{pi}, where i=1 and 2. The capacitance and resistance of the IDE are denoted by C_s and R_s. The parameters can be estimated from [153],

$$C_s = -Imag(Y_{12})/\omega \tag{6.1}$$

and

$$R_s = -1/Real(Y_{12}) \tag{6.2}$$

where ω is the frequency in rad/s, $Imag(Y_{12})$ and $Real(Y_{12})$ are the imaginary and real parts of Y_{12} transfer admittance parameter. The parasitic elements can be calculated from

$$C_{pi} = Imag(Y_{ii} + Y_{12})/\omega \tag{6.3}$$

and

$$R_{pi} = 1/Real(Y_{ii} + Y_{12}) \tag{6.4}$$

where i=1 and 2. Since $Y_{11} \approx Y_{22}$, $C_p = C_{p1} = C_{p2}$ and $Rp = R_{p1} = R_{p2}$.

6.2.3 Fabrication Process of the ID-CPW

The dimensions of the fabricated ID-CPW are listed in Table 6.2. Images of these devices after fabrication can be seen from Figure 6.2. The details of the fabrication process of the ID-CPW device can be found in Chapter 4. A brief summary of the fabrication steps are as following:

- A 100 nm layer of SiO_2 was deposited on p-type high resistance Si wafer using plasma-enhanced chemical vapour deposition (PECVD).
- A layer of PMMA A2 positive e-beam resist was spin coated at 1000 rpm to form a 100 nm thick layer.
- The spin-coated wafer was baked at 170^oC for 5 min.
- Then e-beam lithography was used to pattern ID-CPW.
- The e-beam resist was developed for 1 min using MIBK : IPA for 1:3 ratio.
- After development, a 5 nm of Cr layer was evaporated, followed by a 45 nm layer of Au, and e-beam resist was removed using acetone.
- The sensors were cut from the wafer using a diode pumped solid state laser.

Parameters	**Value**	**Unit**
CPW length	200	μm
Electrode length	50	μm
Electrode width	200	nm
Gap between electrodes	500	nm
Electrode material	Au	NA
Electrode thickness	50	nm
Number of electrodes	99	NA
Oxide material	SiO_2	NA
Oxide thickness	100	nm
Substrate material	Si	NA
Substrate thickness	1000	μm

Table 6.2: Paremeters of fabricated ID-CPW devices.

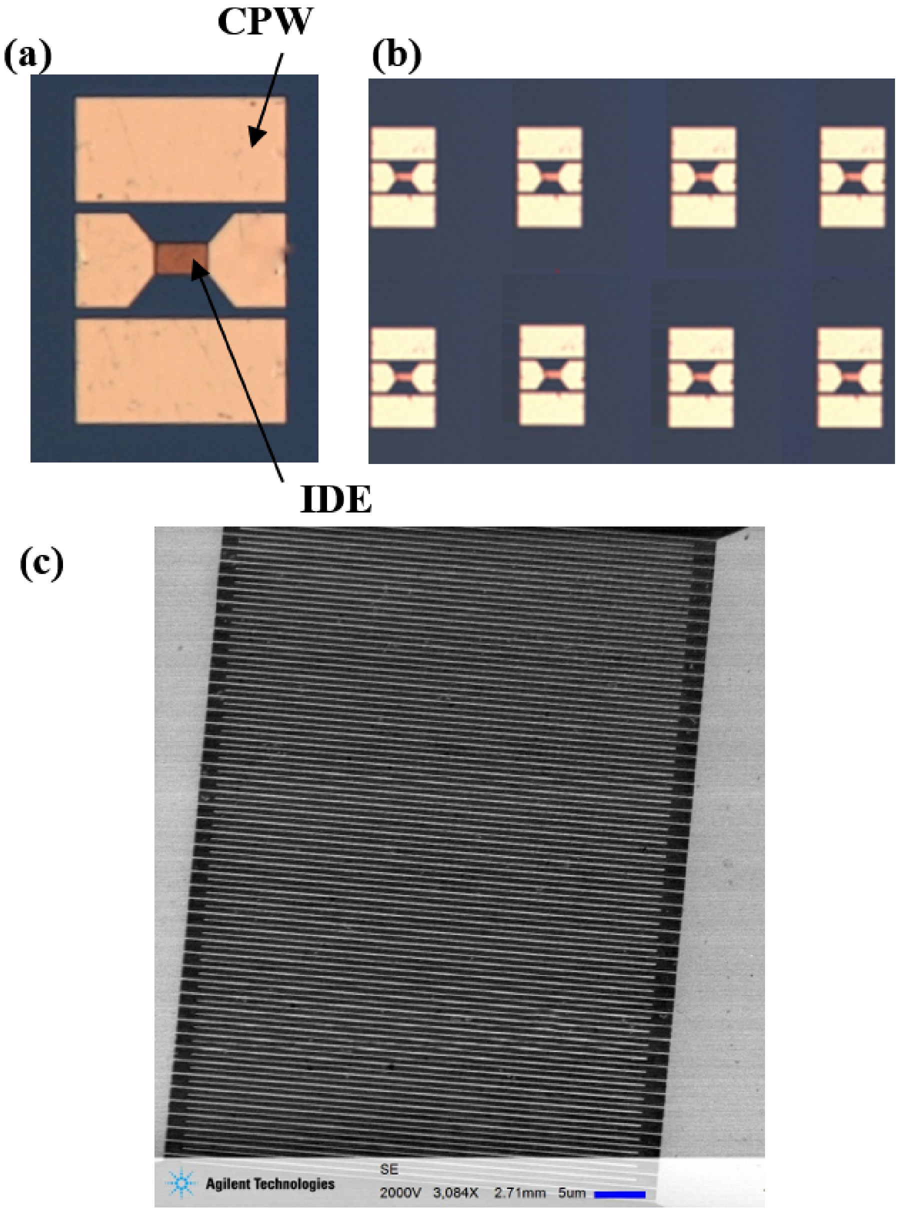

FIGURE 6.2: CPW-IDC devices after fabrication:(a) The ID-CPW consists of a CPW and IDEs. (b) The fabricated ID-CPW sensors on the chip. (c) Scanning electron microscope image of the fabricated IDE.

6.3 Functionalization of sensor surface

Materials

3-Aminopropyltriethoxysilane (APTES), glutaraldehyde (25%) and ethanolamine were purchased from Sigma-Aldrich. Astrocytic protein lysates were extracted from human foetal astrocytes that were derived from foetal brain tissue collected from consenting patients undergoing second trimester (14-18 weeks gestation) terminations at Marie Stopes Clinic, Croydon. This was carried out under ethical approval from the Human Research Ethics Committee (HREC No. 1135373) at the University of Melbourne. The cultures were prepared as described by Trillo-Pazos et al., [154]. Protein was extracted using RIPA (Sigma Aldrich, USA) lysis buffer under standard conditions with protein concentration assayed using bicinchoninic acid (BCA) analysis (BioRad, USA). Polyclonal rabbit anti-GFAP (50 kDa) was purchased from Dako and a secondary Alexa Fluor-488 goat anti-rabbit IgG was purchased from Life Technologies.

Functionalization protocol and immobilization of antigen

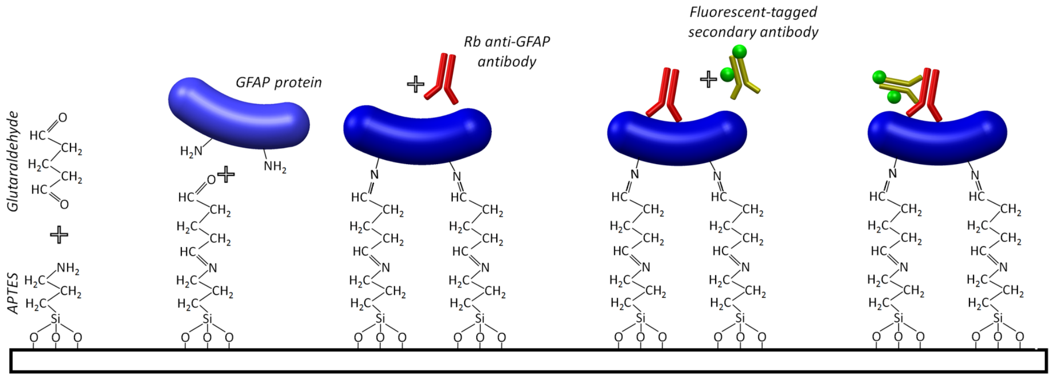

FIGURE 6.3: The functionalization protocol of the sensor surface, immobilizing antigens and antibody binding. The sensors are incubated with 2% APTES in ethanol followed by 2.5% Glutaraldehyde in water. Then the protein is immobilized on the sensor surfaces by incubating astrocytes protein overnight. Then, GFAP antibody is incubated for an hour followed by secondary antibody for an hour.

The immobilization of protein/antigen on the sensor surface is similar to the protocol reported in [155] and can be visually described in Figure 6.3. This process involved the following steps:

- The sensors were initially cleaned using acetone, isopropanol, water and dried using N_2 gas.
- The sensors were then plasma cleaned for 3 minutes at 50 W power at a 40 sccm gas flow comprising of 75% Ar and 25% O_2.
- The sensors were dipped in 2% APTES in ethanol for 1 hour and washed 3 times for 15 minutes using 100% ethanol.
- The sensors were then dipped in 2.5% glutaraldehyde in water for 2 hours and then washed 3 times for 15 minutes using Milli-Q water.
- The astrocytic protein (77 μg/mL) in phosphate buffered saline (PBS) was added to the sensors and incubated for 30 minutes in room temperature and overnight in the refrigerator(4°C), They were washed 3 times for 15 minutes with 1X PBS.
- The sensors were then dipped in 1% ethanolamine and 1% goat serum in water for 1 hour and then washed using Milli-Q water.
- Primary antibody diluted in PBS (2.9 pg/mL, 2.9 ng/mL, 2.9 μg/mL) was added to the sensors for 1 hour followed by 1X PBS wash for 15 minutes.
- Finally secondary antibody in PBS (4 μg/mL) was added and incubated for 1 hour and washed using 1X PBS for 15 minutes.

Figure 6.4 shows the concept discription of sensor after immobilization of antigens and antibodies.

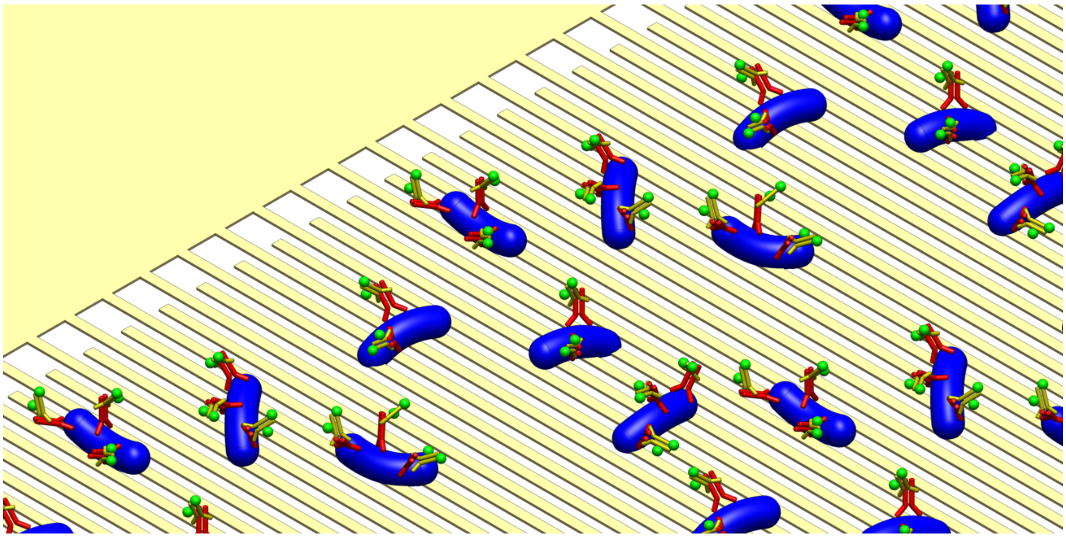

Figure 6.4: The IDEs after immobilization of antigens, GFAP antibodies and secondary antibodies.

6.4 Method

6.4.1 Electrical measurement setup and calibration

The electrical measurements were performed using the vector network analyzer (VNA) at room temperature (25°C) in the 1-25 GHz frequency range. The measurement set-up is shown in Figure 6.5. The short-open-load de-embedding scheme was used for VNA calibration. The S parameters were measured after the microwave probe contact was established with the on wafer ID-CPW. The Y parameters were calculated from the measured S parameters [156] and the average value was obtained from five measurements. The capacitance and resistance of the IDEs and parasitic effects were obtained using Equation 6.1 to 6.4.

6.4.2 Fluorescence measurements

In addition to electrical measurements, fluorescence measurements were undertaken using an inverted fluorescent microscope (Zeiss, BioImaging Station). Reflected light illumination and the filter for Alexa Fluor-488 dye were selected. Exposure time was set to 3 seconds and the ZEN imaging software was used to capture and analyze the images.

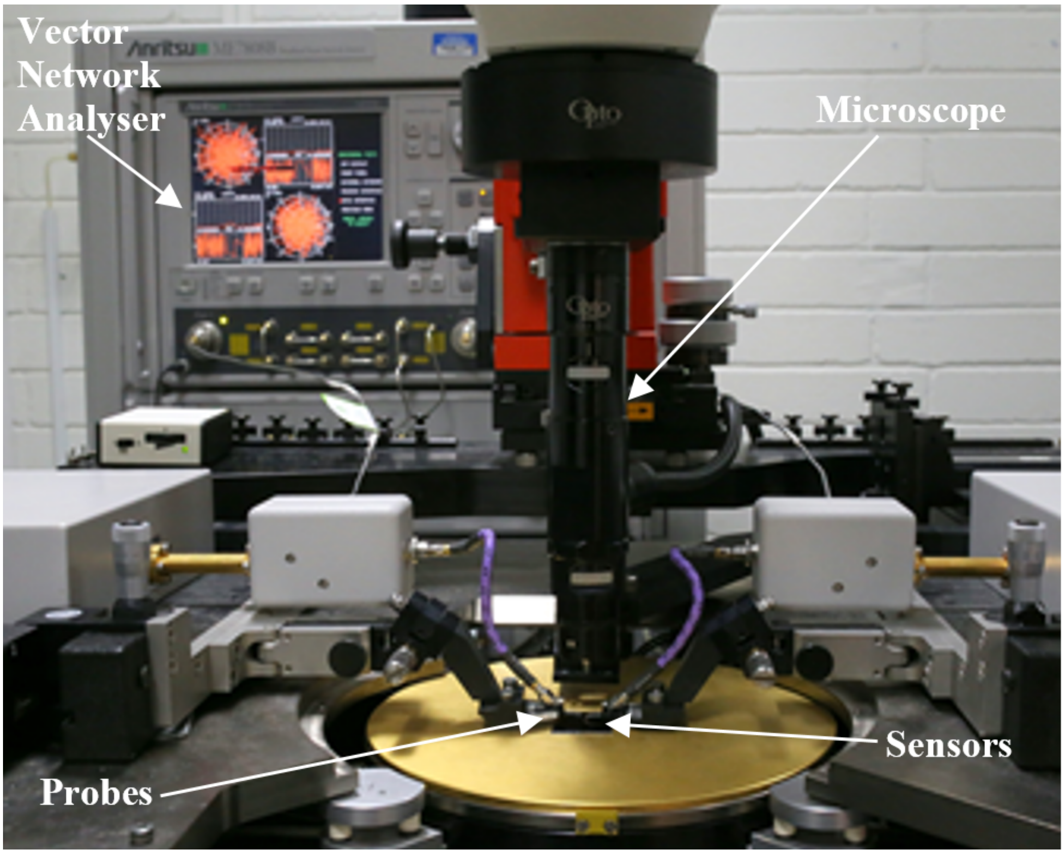

Figure 6.5: Experimental set-up for measurements of S parameters.

6.5 Result and discussion

6.5.1 Optimization of the functionalization protocol

The binding of GFAP antibody to the astrocytic protein immobilized on the SiO_2 surface with various duration of plasma treatments was studied. The surface was plasma cleaned either for 1 minute or 3 minutes and then functionalized using the protocol described above. The fluorescence measurements are shown in Figure 6.6. The concentration of GFAP antibody was 2.9 μg/mL. The fluorescence intensity of the negative control (GFAP antibody was not incubated) is significantly lower when compared to the experiment under positive control with the greatest ability to differentiate positive and negative control experiments being when the surface was plasma treated for 3 minutes.

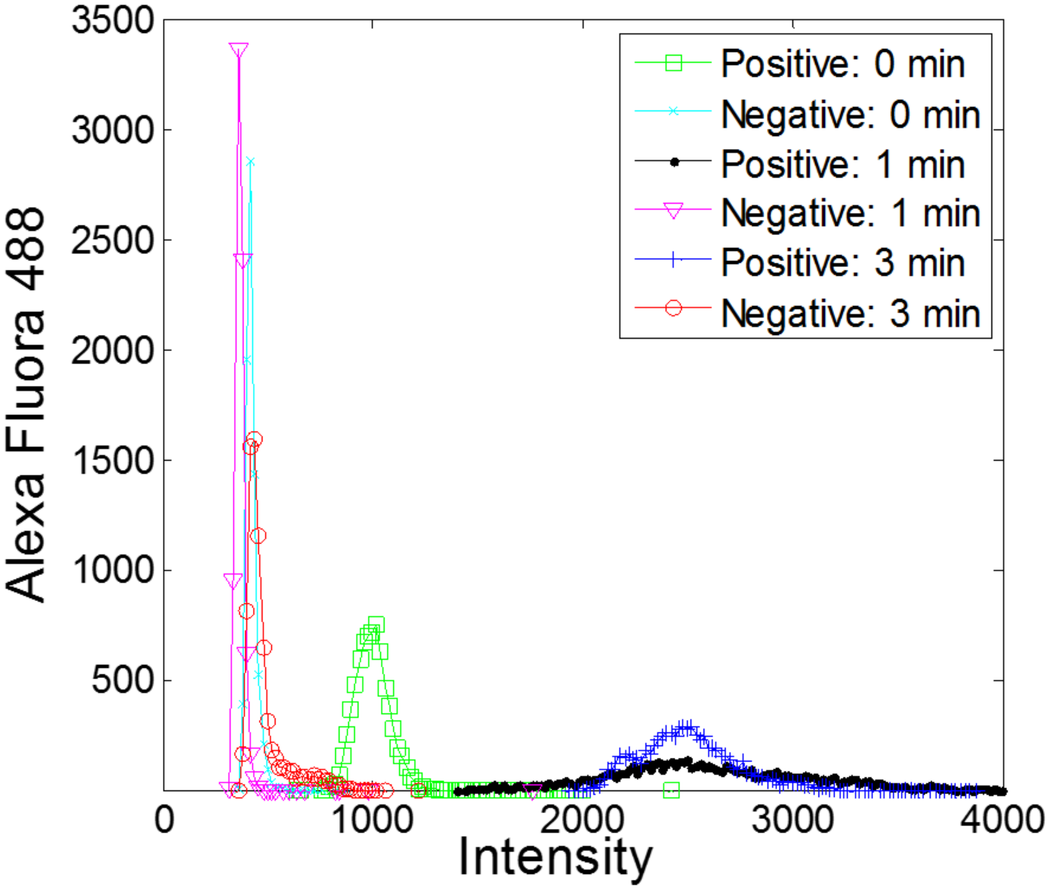

FIGURE 6.6: Fluorescence measurement of SiO_2 surfaces with different plasma treatments. The negative control was not incubated with GFAP antibodies. The concentration of GFAP antibody in positive control was 2.9 μg/mL.

6.5.2 Detection of GFAP antibody binding to GFAP: measurements in dry environment

The S parameters, of a single chip containing 8 ID-CPW sensors shown in Figure 6.1(b), were measured using a VNA. The capacitance of the IDEs, C_s, was calculated using equation 6.1. The variation of C_s with frequency is plotted in Figure 6.7. The sensors were functionalized and astrocytic protein was immobilized as described in a previous section. The positive control sensors were incubated with both GFAP antibodies and secondary antibodies whereas the negative controls were not incubated with the GFAP antibody. Fluorescence microscopy images of positive and negative control sensors are shown in Figure 6.8.

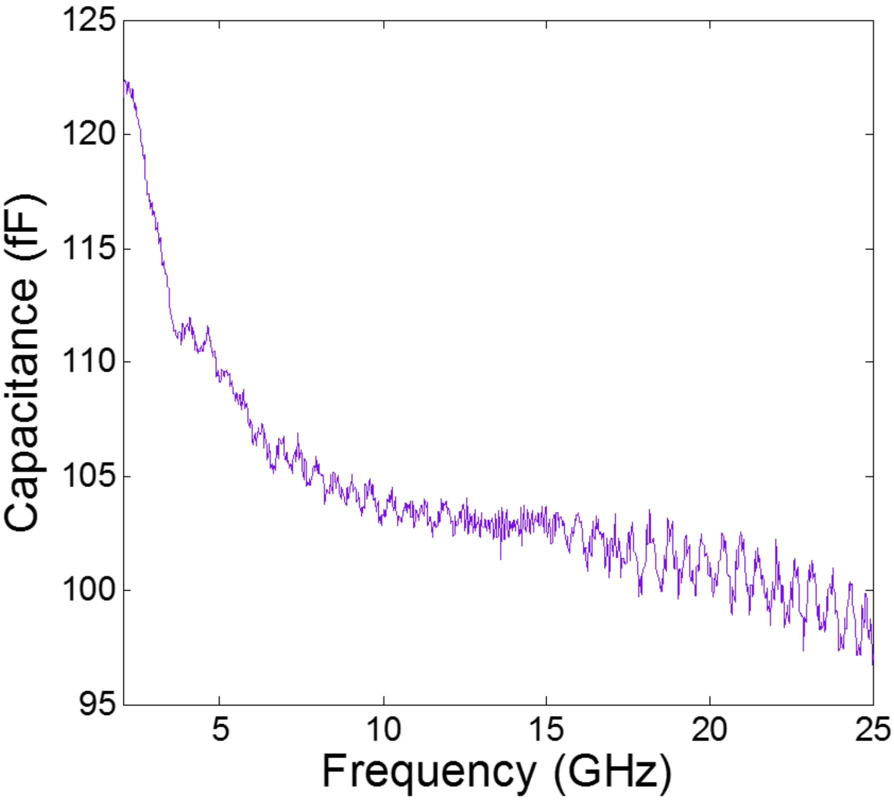

FIGURE 6.7: Variation of capacitance of IDEs with frequency. The length of the electrode is 50 μm, electrode width of IDE is 200 nm and the gap between electrodes is 500 nm.

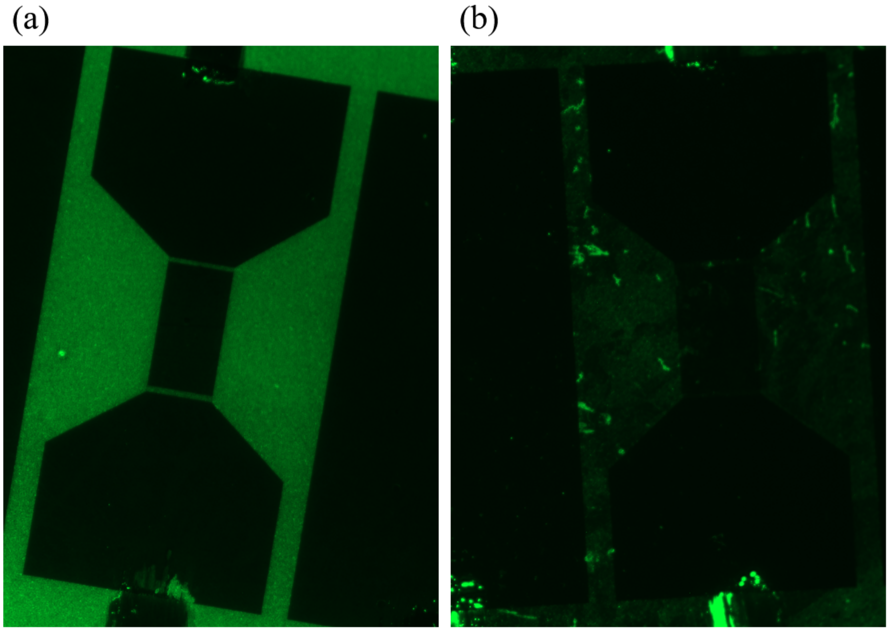

FIGURE 6.8: Fluorescence microcopy images of (a) positive and (b) negative control sensors. Here, the GFAP antibody and secondary antibody concentrations were 2.9 μg/mL and 4 μg/mL. The negative control sensors were not incubated with GFAP antibody.

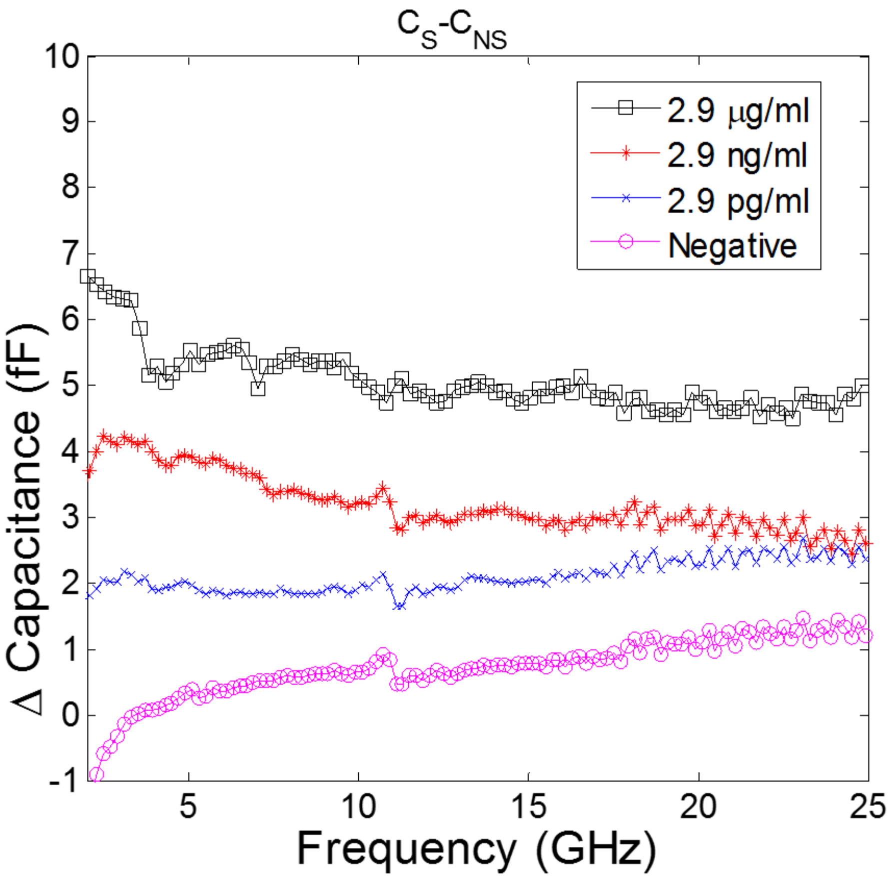

FIGURE 6.9: The changes in capacitance of IDEs after secondary antibody incubation with respect to an empty sensor. The measurements were carried out in a dry environment.

The S parameters of the sensors were measured before functionalization and post incubation with secondary antibodies. The sensors were left to dry in air (dry environment) before the electrical analysis and the measurements of secondary antibodies were carried out under dark light. The concentrations of primary antibodies tested were 2.9 pg/mL, 2.9 ng/mL and 2.9 μg/mL with the secondary antibody concentration at 4 μg/mL. The change in capacitance ($\Delta C = C_S - C_{NS}$) and resistance ($\Delta R = R_S - R_{NS}$) of the IDEs, that is the capacitance and resistance of the sensor after secondary antibody incubation (C_S, R_S) with respect to an empty sensor (C_{NS}, R_{NS}) for varying concentration of primary antibody are shown in Figure 6.9 and Figure 6.10. Our results show the ability of ID-CPW immunosensors to detect antibody levels to a concentration of 2.9 pg/mL in a dry environment. The results confirm the successful binding of GFAP antibodies to inter-digital electrodes functionalized with astrocytic protein. Furthermore, the model based capacitance estimation method suggests that the parasitic capacitance, observed at lower frequencies, does not adversely affect our ability to detect antigen-antibody binding as it is possible to differentiate the capacitance due to antibody binding to the IDE from the parasitic capacitance.

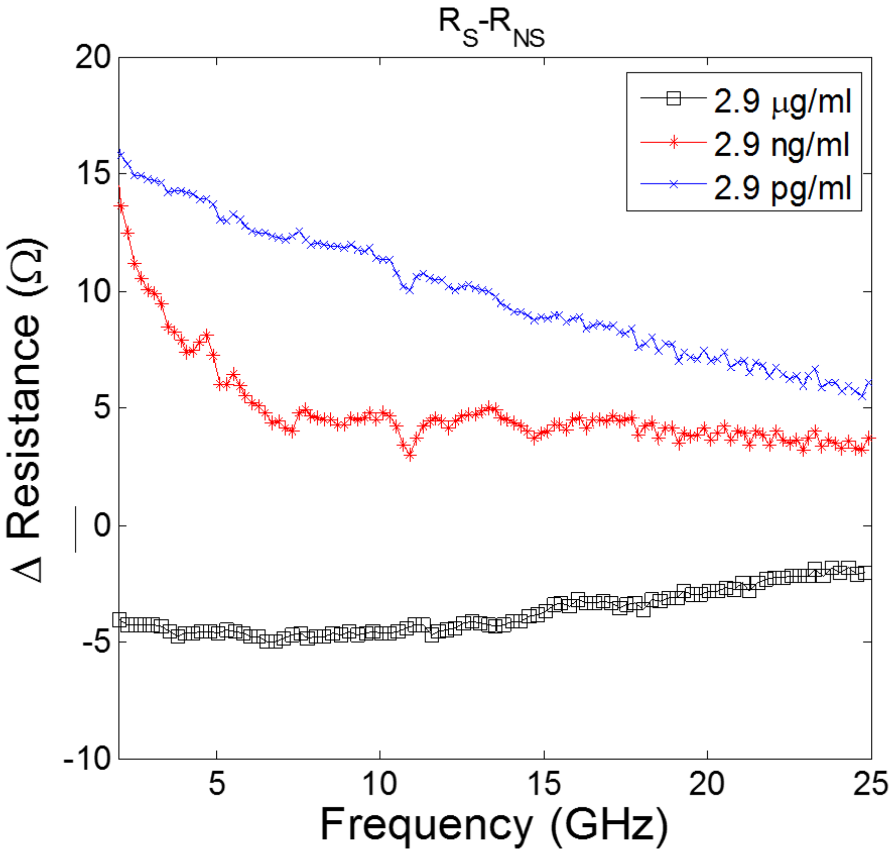

FIGURE 6.10: The changes in resistance of IDEs after secondary antibody incubation with respect to an empty sensor. The measurements were carried out in a dry environment.

As the dielectric constant of the sensor (Si/SiO$_2$/Air) is approximately constant with the frequency, the change in capacitance in the dry environment does not vary significantly with the frequency. We observed that ΔC increases and ΔR decreases with the increasing GFAP antibody concentration. The physical mechanism underlying this observed decrease in resistance with increasing concentration of antibody can be attributed to the fact that GFAP antigens and GFAP antibodies are biomolecular dipoles [157] [158].

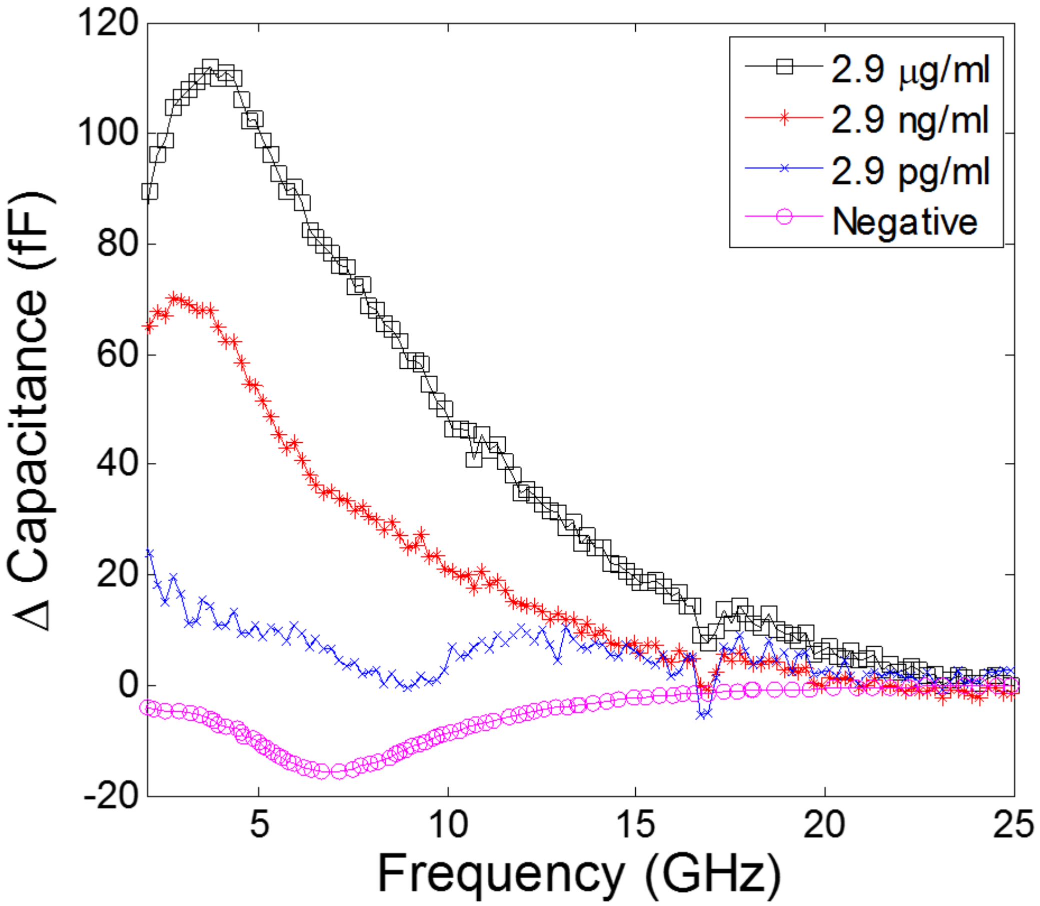

FIGURE 6.11: The change in capacitance of IDE after secondary antibody incubation with respect to an empty sensor. The measurements were carried out in wet environment by adding PBS.

6.5.3 Detection of GFAP antibody binding to GFAP: measurements in wet environment

Antigen-antibody binding in a wet environment was performed in 1X PBS. The empty sensor with PBS (1 μL) was measured before functionalization and post secondary antibody incubation in PBS. The capacitance change, ΔC, as a function of frequency for varying concentration of anti-GFAP primary antibody is shown in Figure 6.11. Since the dielectric constant of water is frequency dependent, decreasing with increasing frequency and becoming constant at very high frequencies, the change in capacitance in the wet environment exhibits a frequency dependence.

Measurements indicate that the capacitance change of the IDE in the wet environment is larger when compared to the dry environment. In the wet environment, PBS has free ions, and at low excitation frequencies the charge on the electrodes attracts chemical species with opposite polarity. An electrical double layer, known as a Helmholtz layer, forms at the sensor-PBS interface which increases the overall capacitance. In our experiments, as the measurements were performed at high frequencies, the large capacitance due to Helmholtz layer formation and electrode polarization did not manifest themselves. This is because the impedance contributed from capacitance is inversely proportional to frequency ($Z_C = 1/(j2\pi fC)$).

Our results show that the change in capacitance at frequencies greater than 20 GHz is independent of GFAP antibody concentration. Thus, the proposed model cannot be used to determine GFAP antibody concentrations at frequencies greater than 20 GHz in wet environments.

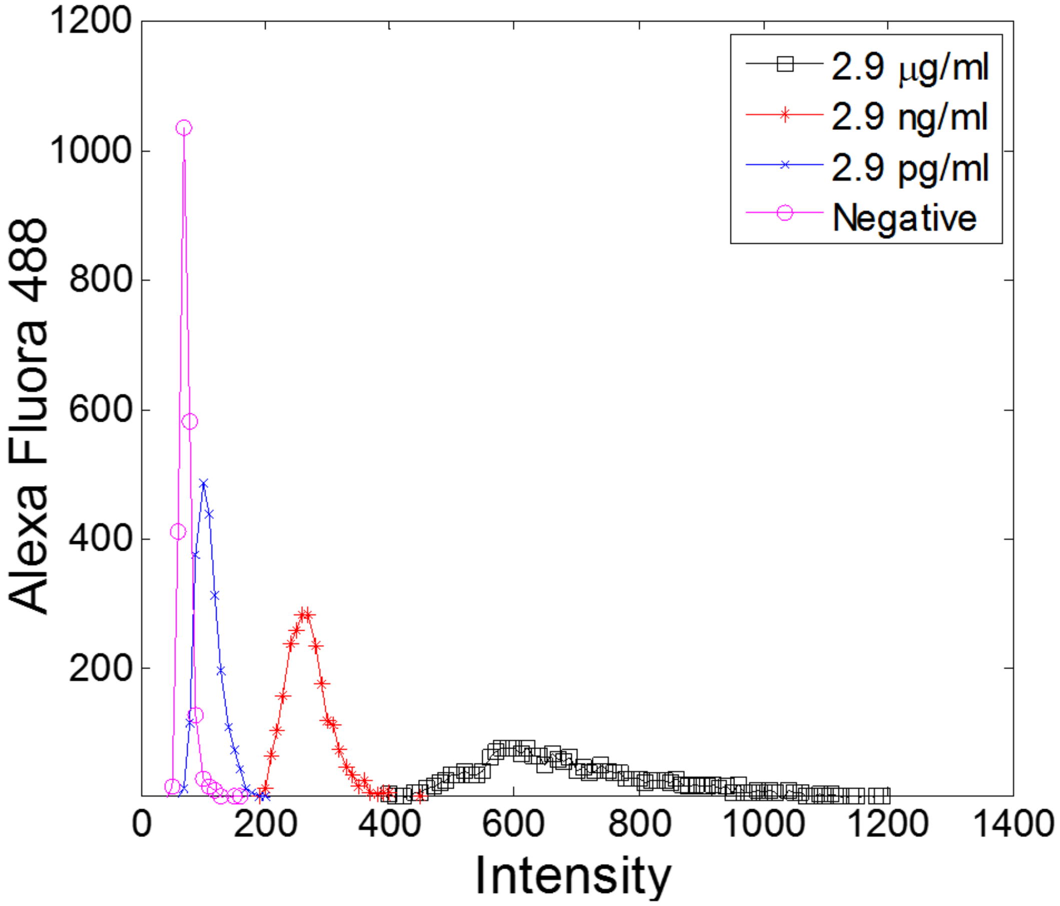

FIGURE 6.12: The fluorescence measurements of positive and negative controls. The negative control was not incubated with GFAP antibodies.

Fluorescence measurements were used to validate the electrical measurements of antigen-antibody binding. Figure 6.12 shows the fluorescence intensity for varying concentration of anti-GFAP primary antibodies, where the intensity decreased with decreasing antibody concentration. The observed fluorescence intensity of these positive controls was larger than that of the negative controls. The fluorescence intensity of the negative control and the samples with 2.9 pg/mL concentration of GFAP antibody exhibited significant overlap indicating that the fluorescence method was close to its detection limit. In contrast, the electrical measurements of the proposed sensor, at the same concentration, were clearly differentiable, supporting the notion that the designed sensor had increased sensitivity compared to state of the art fluorescence measurements.

Enzyme-linked immunosorbent assay (ELISA) measurements have found the serum GFAP levels in glioblastoma patients (median: 180 pg/mL, range: 0-5.6 ng/mL) are significantly higher when compared to those of non-glioblastoma tumor patients (median: 0 ng/mL, range: 0-24 pg/mL) [33]. Likewise the relative antibody levels have been shown to increase with grade of tumor [31]. The results presented in this chapter show that the proposed sensors can be used to detect antibodies against GFAP to concentrations as low as 2.9 pg/mL, with a corresponding capacitance change of 2 fF in the dry environment and 20 fF in the wet environment, for a turnaround time of 3 hours. These levels indicate that the proposed sensor sensitivity is sufficient to monitor GFAP antibodies levels in patients with glioma.

6.6 Conclusion

This chapter demonstrates a low cost and highly sensitive immunosensor for the detection of GFAP antibodies. The results show that the proposed immunosensor is able to detect antibodies against GFAP down to a clinically relevant concentration of 2.9 pg/mL. Measurements indicate an increased sensitivity compared to state-of-the-art optical detection methods.

Chapter 7

Conclusion and Outlook

7.1 Conclusion

In summary, this thesis has investigated the applications of microsystems in the areas of energy harvesting and biological sensing.

Chapter 3 presents simulation works on different types of IDE structures to investigate their potential applications. CoventorWare, a commercial microsystems simulation package, is used to perform these simulations. For microscale IDE structure, which is targeted for energy harvesting application, simulation result indicates a significant increase in device capacitance when water is utilized as dielectric rather than air. This suggests a great potential for applying this type of variable capacitor in electrostatic based mirco power generator. For nanoscale IDE structure, which is targeted for nanometers size biomolecules detection, the simulation is carried to investigate the admittance (or impedance) response of the sensor over a wide range of frequency, from 1 to 20 GHz. The simulation result suggests a good response of a nanoscale IDE sensor to a 20 nm sensitive layer of polymer. The capacitance change is almost 20% over the entire frequency range and conductance change is significant when the frequency is over 100 MHz. The result indicates a potential for applying such sensing system for detecting nanoscale analyte.

Chapter 4 introduces fundamental techniques used in microstytems fabrication. These include resist and spin coating, mask creation and exposure, material deposition and etching. In this thesis, these techniques are applied to fabricate various devices. Examples of these devices consist of microscale IDE capacitor for electrostatic micro power generator, nanoscale IDE capacitor for antigen/antibody detection and nanoscale resonator for ultrahigh sensitive mass sensing.

Chapter 5 demonstrates the application of microscale IDE structure in energy harvesting. Unlike tradition electrostatic micro power generators, which produce variable captivators based on movement of solid metal electrodes of the device, here the liquid ionic solution is utilized to obtain significant change in device capacitance. This immense capacitance change is not only due to the high relative dielectric constant of water, but also substantially due to the double layer capacitor effect. Other notable advantages of this novel type of generator are the simplicity of fabrication, low cost, and low operational constraints (low biased voltage and vibrational frequency). The prototype devices, which operate at 1.2 V biased voltage with the rate of 6 liquid droplets per second, have shown an order of magnitude improvement in FOM compared to previous works.

Chapter 6 demonstrates the application of nanoscale IDE structure for the detection of antibodies. GFAB antibody has been reported to have the highest differential expression to glioma, a tumour that is originated from glial cells. This chapter demonstrates a proof of concept of a sensing system that involves a nanoscale IDE structure with pre-functionalized protein, which can capture GFAB antibody. The sensor measurement is carried out in both PBS solution and in air using a VNA over the frequency range from 1 to 25 GHz. The results show that the sensor can be used to detect GFAB antibody with very low concentration, down to 2.9 picograms per milliliter. This is comparable to the high-end optical methods. This concept can be widely adapted to detect other types of antibodies or nanoscale analytes.

7.2 Future work

7.2.1 Future work on EMPG device

A proposal for a new configuration of the EMPG can be seen from Figure 7.1. This new arrangement will improve the performance of the device and eliminate the requirement of external biased source of the EMPG.

Firstly, the variable capacitors can be fabricated on a flexible substrate, as shown in Figure 7.1(a). By using a commercial mask, the finger width and the gap between fingers can be reduced to less than 2 μm without significant increase in fabrication cost. These dimensions are substantially smaller compared to the fabricated prototypes, which have the finger width of 50 μm and the gap between fingers of 10 μm. Hence, the capacitance of the device is expected to substantially intensify. This results in increasing output power. Furthermore, the use of flexible substrate allows the devices to be rolled to form a cylindrical structure that utilized all the surface of the device to harvest energy. This will lead to an improvement in power density.

In addition, the need to provide a biased source for an EMPG can be eliminated. Figure 7.1(b) shows a circuitry, proposed by de Queiroz and Domingues [9], which can be implemented to collect energy from an EMPG without an external biased source. The key components of this arrangement are the two variable capacitors that have their capacitance changes complement each other (i.e. $\mathrm{C_a}$ is minimum when $\mathrm{C_b}$ is maximum and vice versa). The critical condition for this configuration to be realized is the ratio of capacitance, $\mathrm{C_{max}} : \mathrm{C_{min}}$, must be greater than 1.618. Another significant advantage of this circuitry is it allows a direct charging of battery with energy converted from an EMPG. This is desirable in many practical applications.

In summary, the novel EMPG proposed in this thesis can be further enhanced in terms of performance and usability. The new configuration of the EMPG proposed here can be used to harvest ambient mechanical energy from many scenarios such as human body movement, car movement, rotational parts etc.

7.2.2 Future work on nanoscale biosensor device

The concept of nanoscale biosensor presented in this thesis can be further developed into a low cost portable unit that can be used at point of care or in general clinic. Figure 7.2 shows the concept of the future system, which includes two key components: a sensing cartridge and an electronic unit.

The sensing cartridge is a one-off disposable unit, which includes built-in microfluidics and sensing elements. The microfluidic system comprises of sample inlet/outlet, microfluidic channels with sample processing unit and sensing chamber. The sample-processing unit performs pre-processing tasks such as filtering and separating unwanted objects in order to enhance the sensors' sensitivity and selectivity. The sensing chamber

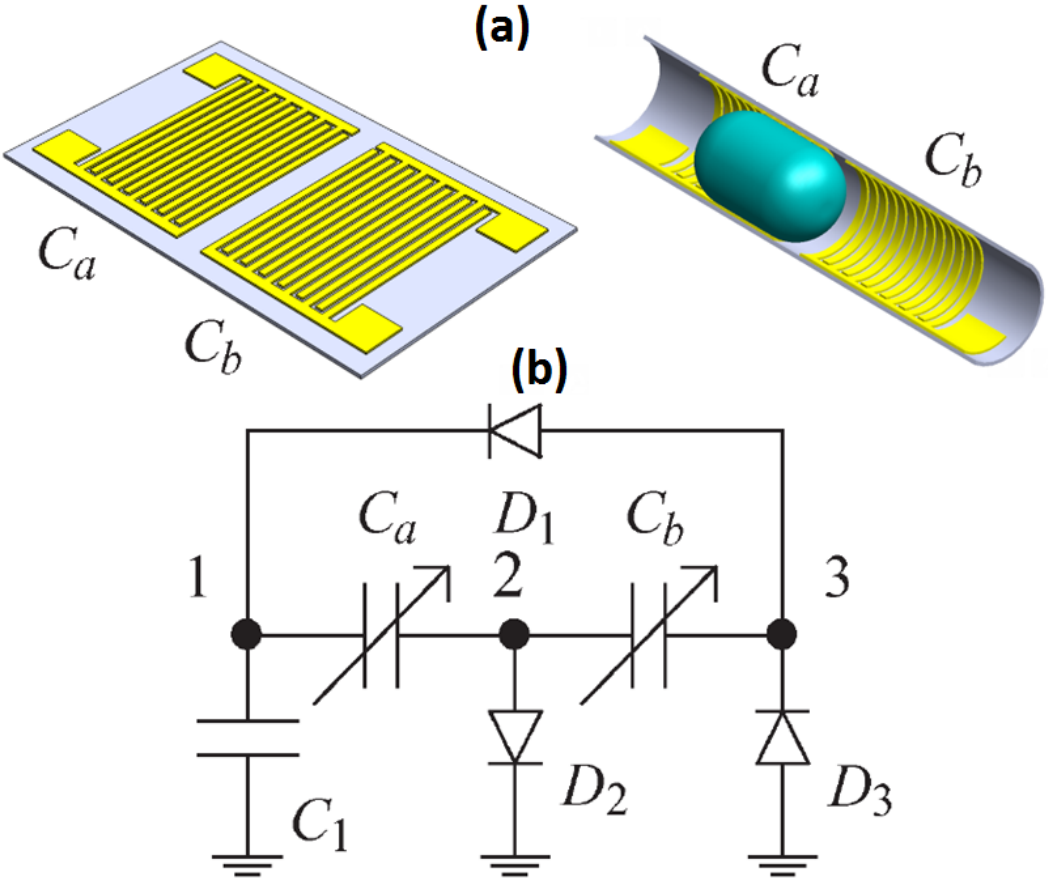

FIGURE 7.1: (a) A proposed configuration of the EMPG device, which includes two identical variable capacitors fabricated on a flexible substrate. The substrate is rolled to form a shielded cylindrical structure with a liquid droplet trapped. (b) A circuit proposed by de Queiroz and Domingues [9]. Under shaking or vibration, the droplet will move and form two complementary variable capacitors, C_a and C_b. The energy converted can be collected to charge the super capacitor C_1 or a battery using the proposed circuit.

is where the sensor array resides. These sensing elements are pre-functionalized so that they target and capture specific analytes. Initially, an external micro pump may be required to facilitate the flows of the sample along the fluidic channel. Potentially, the micropump can also be integrated into the sensing cartridge. The electrical connection from the sensor array to the electronic unit can be realized using a slide-in connector.

The electronic unit is a reusable component. It consists of five key blocks, namely, a microcontroller (uC), a readout circuit, an input unit (buttons), a display (OLED) and a battery management module. The microcontroller is the heart of the electronics. It receives user commands via buttons, controls the sensing measurement unit, the battery management module as well as the OLED display. The most critical part of the electronic unit is the readout circuit that includes a VNA which is capable of performing impedance measurement. The measurement output data from the VNA is captured and further processed by the microcontroller before being displayed on the OLED screen. The sensing system demonstrated in this thesis can operates at frequency lower than 1 GHz. Hence, this readout block can be either implemented on-chip or constructed from discrete electronic components. The power supply for the entire detection system is provided from a single rechargeable battery pack, which can be recharged from a standard USB connector.

The proposed sensing platform is generic and can be applied to various applications. It is not only limited to the detection of various antibodies/antigens, but can also be used to detect other analytes such as bacteria.

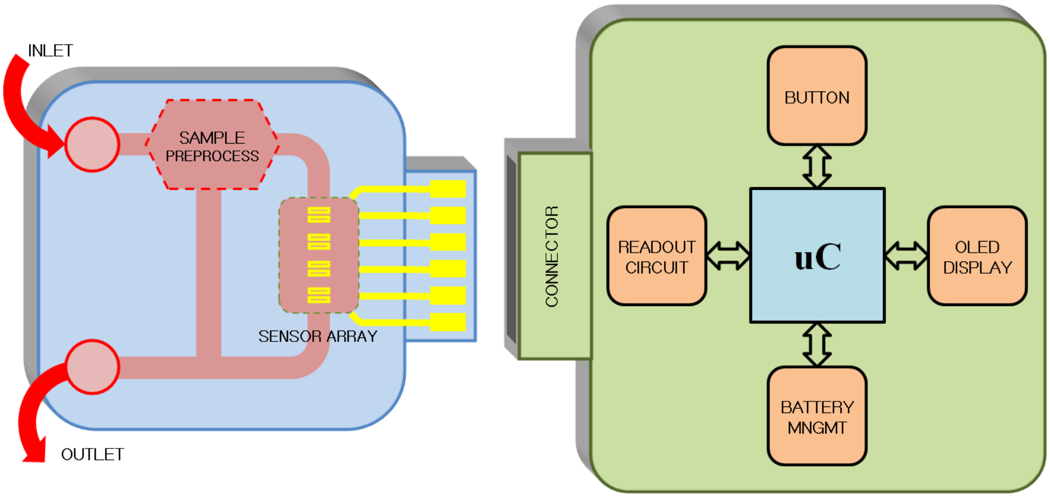

FIGURE 7.2: Concept of a future sensing system, which includes a disposable sensing cartridge and a reusable electronic unit.

Bibliography

[1] R. Colin Johnson. Mems market: Ups and upstarts, 2015. URL http://www.eetimes.com/document.asp?doc_id=1328333.

[2] B. Ahmed Seddik S. Boisseau, G. Despesse. *Electrostatic Conversion for Vibration Energy Harvesting*. Intech, 2012.

[3] Tuan Vo-Dinh. Biosensors and Biochips. In *BioMEMS and Biomedical Nanotechnology*, pages 1–20. Springer US, 2006. ISBN 978-0-387-25566-8 978-0-387-25845-4.

[4] Peter Van Gerwen, Wim Laureyn, Wim Laureys, Guido Huyberechts, Maaike Op De Beeck, Kris Baert, Jan Suls, Willy Sansen, P. Jacobs, Lou Hermans, and Robert Mertens. Nanoscaled interdigitated electrode arrays for biochemical sensors. *Sensors and Actuators B: Chemical*, 49(1–2):73–80, June 1998.

[5] W Laureyn, D Nelis, P Van Gerwen, K Baert, L Hermans, R Magnée, J. J Pireaux, and G Maes. Nanoscaled interdigitated titanium electrodes for impedimetric biosensing. *Sensors and Actuators B: Chemical*, 68(1–3):360–370, 2000. ISSN 0925-4005. doi: 10.1016/S0925-4005(00)00489-5.

[6] Rui Igreja and C. J. Dias. Analytical evaluation of the interdigital electrodes capacitance for a multi-layered structure. *Sensors and Actuators A: Physical*, 112 (2–3):291–301, 2004. ISSN 0924-4247. doi: 10.1016/j.sna.2004.01.040.

[7] Rui Igreja and C. J. Dias. Extension to the analytical model of the interdigital electrodes capacitance for a multi-layered structure. *Sensors and Actuators A: Physical*, 172(2):392–399, 2011. ISSN 0924-4247. doi: 10.1016/j.sna.2011.09.033.

[8] Sunipa Roy and Chandan Sarkar. *MEMS and Nanotechnology for Gas Sensors*. CRC Press, 2015. ISBN 978-1-4987-0012-2 978-1-4987-0013-9.

[9] A.C.M. de Queiroz and M. Domingues. The Doubler of Electricity Used as Battery Charger. *IEEE Transactions on Circuits and Systems II: Express Briefs*, 58(12): 797–801, 2011. ISSN 1549-7747.

[10] Stephen D. Senturia. *MICROSYSTEM DESIGN*. Kluwer Academic Publishers, 2002.

[11] S. Meninger, J. O. Mur-Miranda, R. Amirtharajah, A. Chandrakasan, and J. H. Lang. Vibration-to-electric energy conversion. *IEEE Transactions on Very Large Scale Integration (VLSI) Systems*, 9(1):64–76, 2001. ISSN 1063-8210. doi: 10.1109/92.920820.

[12] Wendong Zhang Shengbo Sang and Yuan Zhao. Review on the design art of biosensors. *State of the Art in Biosensors - General Aspects, Intech*, 2013. doi: DOI:10.5772/52257.

[13] Shyam Aravamudhan, Arun Kumar, Shyam Mohapatra, and Shekhar Bhansali. Sensitive estimation of total cholesterol in blood using Au nanowires based microfluidic platform. *Biosensors and Bioelectronics*, 22(9–10):2289–2294, 2007. ISSN 0956-5663. doi: 10.1016/j.bios.2006.11.027.

[14] D. S. Ferreira, T. S. Monteiro, and G. Minas. Spectroscopy microsystem for the detection of early cancer. In *Bioengineering (ENBENG), 2012 IEEE 2nd Portuguese Meeting in*, pages 1–4, 2012. doi: 10.1109/ENBENG.2012.6331371.

[15] K. Takahashi, R. Ozawa, H. Oyama, M. Futagawa, F. Dasai, M. Ishida, and K. Sawada. A CMOS-MEMS-based label-free protein sensor for high-sensitive and compact system. In *Electron Devices Meeting (IEDM), 2012 IEEE International*, pages 24.6.1–24.6.4, 2012. doi: 10.1109/IEDM.2012.6479097.

[16] Andreas Hierlemann and Henry Baltes. CMOS-based chemical microsensors. *Analyst*, 128(1):15–28, 2003. ISSN 1364-5528. doi: 10.1039/B208563C.

[17] Oda Stoevesandt, Michael J. Taussig, and Mingyue He. Protein microarrays: high-throughput tools for proteomics. *Expert Review of Proteomics*, 6(2):145–157, 2009. ISSN 1478-9450. doi: 10.1586/epr.09.2.

[18] Yonghao Zhang and Pinar Ozdemir. Microfluidic DNA amplification—A review. *Analytica Chimica Acta*, 638(2):115–125, 2009. ISSN 0003-2670. doi: 10.1016/j.aca.2009.02.038.

[19] Nicholas M. Toriello, Chung N. Liu, and Richard A. Mathies. Multichannel Reverse Transcription-Polymerase Chain Reaction Microdevice for Rapid Gene Expression and Biomarker Analysis. *Analytical Chemistry*, 78(23):7997–8003, 2006. ISSN 0003-2700. doi: 10.1021/ac061058k.

[20] Venkatachalam Chokkalingam, Jurjen Tel, Florian Wimmers, Xin Liu, Sergey Semenov, Julian Thiele, Carl G. Figdor, and Wilhelm T. S. Huck. Probing cellular heterogeneity in cytokine-secreting immune cells using droplet-based microfluidics. *Lab on a Chip*, 13(24):4740–4744, 2013. ISSN 1473-0189. doi: 10.1039/C3LC50945A.

[21] Rafael Gómez-Sjöberg, Anne A. Leyrat, Dana M. Pirone, Christopher S. Chen, and Stephen R. Quake. Versatile, Fully Automated, Microfluidic Cell Culture System. *Analytical Chemistry*, 79(22):8557–8563, 2007. ISSN 0003-2700. doi: 10.1021/ac071311w.

[22] Nobuyuki Futai, Wei Gu, Jonathan W. Song, and Shuichi Takayama. Handheld recirculation system and customized media for microfluidic cell culture. *Lab on a Chip*, 6(1):149–154, 2006. ISSN 1473-0189. doi: 10.1039/B510901A.

[23] S. N. Bhatia, U. J. Balis, M. L. Yarmush, and M. Toner. Probing heterotypic cell interactions: Hepatocyte function in microfabricated co-cultures. *Journal of Biomaterials Science, Polymer Edition*, 9(11):1137–1160, 1998. ISSN 0920-5063. doi: 10.1163/156856298X00695.

[24] Dongeun Huh, Benjamin D. Matthews, Akiko Mammoto, Martín Montoya-Zavala, Hong Yuan Hsin, and Donald E. Ingber. Reconstituting Organ-Level Lung Functions on a Chip. *Science*, 328(5986):1662–1668, 2010. ISSN 0036-8075, 1095-9203. doi: 10.1126/science.1188302.

[25] Ronalee Lo, Po-Ying Li, Saloomeh Saati, Rajat Agrawal, Mark S. Humayun, and Ellis Meng. A refillable microfabricated drug delivery device for treatment of ocular diseases. *Lab on a Chip*, 8(7):1027–1030, 2008. ISSN 1473-0189. doi: 10.1039/B804690E.

[26] E. E. Nuxoll and R. A. Siegel. BioMEMS devices for drug delivery. *IEEE Engineering in Medicine and Biology Magazine*, 28(1):31–39, 2009. ISSN 0739-5175. doi: 10.1109/MEMB.2008.931014.

[27] K. J. REBELLO. Applications of MEMS in surgery. *Proceedings of the IEEE*, 92 (1):43–55, 2004. ISSN 0018-9219. doi: 10.1109/JPROC.2003.820536.

[28] Jonathan Viventi, Dae-Hyeong Kim, Joshua D. Moss, Yun-Soung Kim, Justin A. Blanco, Nicholas Annetta, Andrew Hicks, Jianliang Xiao, Younggang Huang, David J. Callans, John A. Rogers, and Brian Litt. A Conformal, Bio-Interfaced Class of Silicon Electronics for Mapping Cardiac Electrophysiology. *Science Translational Medicine*, 2(24):24ra22–24ra22, 2010. ISSN 1946-6234, 1946-6242. doi: 10.1126/scitranslmed.3000738.

[29] Leigh R. Hochberg, Mijail D. Serruya, Gerhard M. Friehs, Jon A. Mukand, Maryam Saleh, Abraham H. Caplan, Almut Branner, David Chen, Richard D. Penn, and John P. Donoghue. Neuronal ensemble control of prosthetic devices by a human with tetraplegia. *Nature*, 442(7099):164–171, 2006. ISSN 0028-0836. doi: 10.1038/nature04970.

[30] György Buzsáki. Large-scale recording of neuronal ensembles. *Nature Neuroscience*, 7(5):446–451, 2004. ISSN 1097-6256. doi: 10.1038/nn1233.

[31] Ping Wei, Wei Zhang, Liu-Song Yang, Hai-Shi Zhang, Xiao-En Xu, Ying-Hua Jiang, Feng-Ping Huang, and Qian Shi. Serum GFAP autoantibody as an ELISA-detectable glioma marker. *Tumor Biology*, 34(4):2283–2292, 2013. ISSN 1010-4283, 1423-0380. doi: 10.1007/s13277-013-0770-7.

[32] T. Brommeland, L. Rosengren, S. Fridlund, R. Hennig, and V. Isaksen. Serum levels of glial fibrillary acidic protein correlate to tumour volume of high-grade gliomas. *Acta Neurologica Scandinavica*, 116(6):380–384, 2007. ISSN 1600-0404. doi: 10.1111/j.1600-0404.2007.00889.x.

[33] C. S. Jung, C. Foerch, A. Schänzer, A. Heck, K. H. Plate, V. Seifert, H. Steinmetz, A. Raabe, and M. Sitzer. Serum GFAP is a diagnostic marker for glioblastoma multiforme. *Brain*, 130(12):3336–3341, 2007. ISSN 0006-8950, 1460-2156. doi: 10.1093/brain/awm263.

[34] J. Middeldorp and E. M. Hol. GFAP in health and disease. *Progress in Neurobiology*, 93(3):421–443, 2011. ISSN 0301-0082. doi: 10.1016/j.pneurobio.2011.01.005.

[35] Anjum Qureshi, Javed H. Niazi, Saravan Kallempudi, and Yasar Gurbuz. Label-free capacitive biosensor for sensitive detection of multiple biomarkers using gold interdigitated capacitor arrays. *Biosensors and Bioelectronics*, 25(10):2318–2323, 2010. ISSN 0956-5663. doi: 10.1016/j.bios.2010.03.018.

[36] S. P. Beeby, M. J. Tudor, and N. M. White. Energy harvesting vibration sources for microsystems applications. *Measurement Science and Technology*, 17(12):R175, 2006. ISSN 0957-0233. doi: 10.1088/0957-0233/17/12/R01.

[37] Oleg D. Jefimenko and David K. Walker. Electrostatic Current Generator Having a Disk Electret as an Active Element. *IEEE Transactions on Industry Applications*, IA-14(6):537–540, 1978.

[38] Yasufusa Tada. Experimental Characteristics of Electret Generator, Using Polymer Film Electrets. *Japanese Journal of Applied Physics*, 31(3R):846, 1992.

[39] J. Boland, Yuan-Heng Chao, Y. Suzuki, and Y. C. Tai. Micro electret power generator. In *IEEE The Sixteenth Annual International Conference on Micro Electro Mechanical Systems, 2003. MEMS-03 Kyoto*, pages 538–541, 2003. doi: 10.1109/MEMSYS.2003.1189805.

[40] J.S. Boland, J.D.M. Messenger, K.W. Lo, and Y.C. Tai. Arrayed liquid rotor electret power generator systems. In *18th IEEE International Conference on Micro Electro Mechanical Systems, 2005. MEMS 2005*, pages 618–621, 2005.

[41] T. Tsutsumino, Y. Suzuki, N. Kasagi, and Y. Sakane. Seismic Power Generator Using High-Performance Polymer Electret. In *19th IEEE International Conference on Micro Electro Mechanical Systems, 2006. MEMS 2006 Istanbul*, pages 98–101, 2006.

[42] Hsi-wen Lo, Rus Whang, and Yu-Chong Tai. A simple micro electret power generator. In *IEEE 20th International Conference on Micro Electro Mechanical Systems, 2007. MEMS*, pages 859–862, 2007.

[43] Yoshihiko Sakane, Yuji Suzuki, and Nobuhide Kasagi. The development of a high-performance perfluorinated polymer electret and its application to micro power

generation. *Journal of Micromechanics and Microengineering*, 18(10):104011, 2008.

[44] M. Edamoto, Y. Suzuki, N. Kasagi, K. Kashiwagi, Y. Morizawa, T. Yokoyama, T. Seki, and M. Oba. Low-Resonant-Frequency Micro Electret Generator for Energy Harvesting Application. In *IEEE 22nd International Conference on Micro Electro Mechanical Systems, 2009. MEMS 2009*, pages 1059–1062, 2009. doi: 10.1109/MEMSYS.2009.4805569.

[45] S. Boisseau, G. Despesse, T. Ricart, E. Defay, and A. Sylvestre. Cantilever-based electret energy harvesters. *Smart Materials and Structures*, 20(10):105013, 2011. ISSN 0964-1726, 1361-665X. doi: 10.1088/0964-1726/20/10/105013.

[46] R. Tashiro, N. Kabei, K. Katayama, E. Tsuboi, and K. Tsuchiya. Development of an electrostatic generator for a cardiac pacemaker that harnesses the ventricular wall motion. *Journal of Artificial Organs*, 5(4):0239–0245, 2002. ISSN 1434-7229. doi: 10.1007/s100470200045.

[47] P. D. Mitcheson, T. C. Green, E. M. Yeatman, and A. S. Holmes. Architectures for vibration-driven micropower generators. *Journal of Microelectromechanical Systems*, 13(3):429–440, 2004. ISSN 1057-7157. doi: 10.1109/JMEMS.2004.830151.

[48] Ghislain Despesse, Thomas Jager, Chaillout Jean-Jacques, Jean-Michel Léger, Andrea Vassilev, Skandar Basrour, and Benoit Charlot. Fabrication and characterization of high damping electrostatic micro devices for vibration energy scavenging. *Proc. Design, Test, Integration and Packaging of MEMS and MOEMS*, pages 386–390, 2005.

[49] B.C. Yen and Jeffrey H. Lang. A variable-capacitance vibration-to-electric energy harvester. *IEEE Transactions on Circuits and Systems I: Regular Papers*, 53(2): 288–295, February 2006.

[50] Daniel Hoffmann, Bernd Folkmer, and Yiannos Manoli. Fabrication, characterization and modelling of electrostatic micro-generators. *Journal of Micromechanics and Microengineering*, 19(9):094001, September 2009.

[51] P. Basset, D. Galayko, A. Mahmood Paracha, F. Marty, A. Dudka, and T. Bourouina. A batch-fabricated and electret-free silicon electrostatic vibration energy harvester. *Journal of Micromechanics and Microengineering*, 19(11): 115025, 2009.

[52] Xudong Fan, Ian M. White, Siyka I. Shopova, Hongying Zhu, Jonathan D. Suter, and Yuze Sun. Sensitive optical biosensors for unlabeled targets: A review. *Analytica Chimica Acta*, 620(1–2):8–26, 2008. ISSN 0003-2670. doi: 10.1016/j.aca.2008.05.022.

[53] F. C. Chien, C. Y. Lin, J. N. Yih, K. L. Lee, C. W. Chang, P. K. Wei, C. C. Sun, and S. J. Chen. Coupled waveguide–surface plasmon resonance biosensor with subwavelength grating. *Biosensors and Bioelectronics*, 22(11):2737–2742, 2007. ISSN 0956-5663. doi: 10.1016/j.bios.2006.11.021.

[54] Akihiro Suzuki, Jun Kondoh, Yoshikazu Matsui, Showko Shiokawa, and Kazuyasu Suzuki. Development of novel optical waveguide surface plasmon resonance (SPR) sensor with dual light emitting diodes. *Sensors and Actuators B: Chemical*, 106 (1):383–387, 2005. ISSN 0925-4005. doi: 10.1016/j.snb.2004.08.021.

[55] Wing-Cheung Law, Przemyslaw Markowicz, Ken-Tye Yong, Indrajit Roy, Alexander Baev, Sergiy Patskovsky, Andrei V. Kabashin, Ho-Pui Ho, and Paras N. Prasad. Wide dynamic range phase-sensitive surface plasmon resonance biosensor based on measuring the modulation harmonics. *Biosensors and Bioelectronics*, 23 (5):627–632, 2007. ISSN 0956-5663. doi: 10.1016/j.bios.2007.07.015.

[56] Allen D. Taylor, Qiuming Yu, Shengfu Chen, Jiří Homola, and Shaoyi Jiang. Comparison of E. coli O157:H7 preparation methods used for detection with surface plasmon resonance sensor. *Sensors and Actuators B: Chemical*, 107(1):202–208, 2005. ISSN 0925-4005. doi: 10.1016/j.snb.2004.11.097.

[57] M. Weisser, G. Tovar, S. Mittler-Neher, W. Knoll, F. Brosinger, H. Freimuth, M. Lacher, and W. Ehrfeld. Specific bio-recognition reactions observed with an integrated Mach–Zehnder interferometer. *Biosensors and Bioelectronics*, 14(4): 405–411, 1999. ISSN 0956-5663. doi: 10.1016/S0956-5663(98)00124-9.

[58] Dmitry A. Markov, Kelly Swinney, and Darryl J. Bornhop. Label-Free Molecular Interaction Determinations with Nanoscale Interferometry. *Journal of the*

American Chemical Society, 126(50):16659–16664, 2004. ISSN 0002-7863. doi: 10.1021/ja047820m.

[59] Darryl J. Bornhop, Joey C. Latham, Amanda Kussrow, Dmitry A. Markov, Richard D. Jones, and Henrik S. Sørensen. Free-Solution, Label-Free Molecular Interactions Studied by Back-Scattering Interferometry. *Science*, 317(5845): 1732–1736, 2007. ISSN 0036-8075, 1095-9203. doi: 10.1126/science.1146559.

[60] Mohammed Zourob, Stephan Mohr, Bernard J. Treves Brown, Peter R. Fielden, Martin B. McDonnell, and Nicholas J. Goddard. An Integrated Metal Clad Leaky Waveguide Sensor for Detection of Bacteria. *Analytical Chemistry*, 77(1):232–242, 2005. ISSN 0003-2700. doi: 10.1021/ac049627g.

[61] N. Skivesen, R. Horvath, S. Thinggaard, N. B. Larsen, and H. C. Pedersen. Deep-probe metal-clad waveguide biosensors. *Biosensors and Bioelectronics*, 22(7):1282–1288, 2007. ISSN 0956-5663. doi: 10.1016/j.bios.2006.05.025.

[62] Yi Wang, Honggen Li, Zhuangqi Cao, Tianyi Yu, Qishun Shen, and Ying He. Oscillating wave sensor based on the Goos–Hänchen effect. *Applied Physics Letters*, 92(6):061117, 2008. ISSN 0003-6951, 1077-3118. doi: 10.1063/1.2883929.

[63] A. Ramachandran, S. Wang, J. Clarke, S. J. Ja, D. Goad, L. Wald, E. M. Flood, E. Knobbe, J. V. Hryniewicz, S. T. Chu, D. Gill, W. Chen, O. King, and B. E. Little. A universal biosensing platform based on optical micro-ring resonators. *Biosensors and Bioelectronics*, 23(7):939–944, 2008. ISSN 0956-5663. doi: 10.1016/j.bios.2007.09.007.

[64] Hongying Zhu, Ian M. White, Jonathan D. Suter, Mohammed Zourob, and Xudong Fan. Opto-fluidic micro-ring resonator for sensitive label-free viral detection. *Analyst*, 133(3):356–360, 2008. ISSN 1364-5528. doi: 10.1039/B716834A.

[65] A. Yalcin, K. C. Popat, J. C. Aldridge, T. A. Desai, J. Hryniewicz, N. Chbouki, B. E. Little, Oliver King, V. Van, Sai Chu, D. Gill, M. Anthes-Washburn, M. S. Unlu, and B. B. Goldberg. Optical sensing of biomolecules using microring resonators. *IEEE Journal of Selected Topics in Quantum Electronics*, 12(1):148–155, 2006. ISSN 1077-260X. doi: 10.1109/JSTQE.2005.863003.

[66] Hidehisa Tazawa, Tomohiko Kanie, and Makoto Katayama. Fiber-optic coupler based refractive index sensor and its application to biosensing. *Applied Physics Letters*, 91(11):113901, 2007. ISSN 0003-6951, 1077-3118. doi: 10.1063/1.2783278.

[67] Tyson L. Lowder, John D. Gordon, Stephen M. Schultz, and Richard H. Selfridge. Volatile organic compound sensing using a surface-relief D-shaped fiber Bragg grating and a polydimethylsiloxane layer. *Optics Letters*, 32(17):2523, 2007. ISSN 0146-9592, 1539-4794. doi: 10.1364/OL.32.002523.

[68] Tao Wei, Yukun Han, Hai-Lung Tsai, and Hai Xiao. Miniaturized fiber inline Fabry-Perot interferometer fabricated with a femtosecond laser. *Optics Letters*, 33 (6):536, 2008. ISSN 0146-9592, 1539-4794. doi: 10.1364/OL.33.000536.

[69] Mindy R. Lee and Philippe M. Fauchet. Two-dimensional silicon photonic crystal based biosensing platform for protein detection. *Optics Express*, 15(8):4530, 2007. ISSN 1094-4087. doi: 10.1364/OE.15.004530.

[70] Lars Rindorf, Jesper B. Jensen, Martin Dufva, Lars Hagsholm Pedersen, Poul Erik Høiby, and Ole Bang. Photonic crystal fiber long-period gratings for biochemical sensing. *Optics Express*, 14(18):8224, 2006. ISSN 1094-4087. doi: 10.1364/OE.14.008224.

[71] Peter Y Li, Bo Lin, John Gerstenmaier, and Brian T Cunningham. A new method for label-free imaging of biomolecular interactions. *Sensors and Actuators B: Chemical*, 99(1):6–13, 2004. ISSN 0925-4005. doi: 10.1016/S0925-4005(03)00604-X.

[72] Niina J. Ronkainen, H. Brian Halsall, and William R. Heineman. Electrochemical biosensors. *Chemical Society Reviews*, 39(5):1747–1763, 2010. ISSN 1460-4744. doi: 10.1039/B714449K.

[73] Dorothee Grieshaber, Robert MacKenzie, Janos Vörös, and Erik Reimhult. Electrochemical Biosensors - Sensor Principles and Architectures. *Sensors (Basel, Switzerland)*, 8(3):1400–1458, 2008. ISSN 1424-8220.

[74] B. Stein, M. George, H. E. Gaub, and W. J. Parak. Extracellular measurements of averaged ionic currents with the light-addressable potentiometric sensor (LAPS). *Sensors and Actuators B: Chemical*, 98(2–3):299–304, 2004. ISSN 0925-4005. doi: 10.1016/j.snb.2003.10.034.

[75] Y. Mourzina, T. Yoshinobu, J. Schubert, H. Lüth, H. Iwasaki, and M. J. Schöning. Ion-selective light-addressable potentiometric sensor (LAPS) with chalcogenide thin film prepared by pulsed laser deposition. *Sensors and Actuators B: Chemical*, 80(2):136–140, 2001. ISSN 0925-4005. doi: 10.1016/S0925-4005(01)00906-6.

[76] Eric Bakker and Ernö Pretsch. Potentiometric sensors for trace-level analysis. *TrAC Trends in Analytical Chemistry*, 24(3):199–207, 2005. ISSN 0165-9936. doi: 10.1016/j.trac.2005.01.003.

[77] M Santandreu, S Alegret, and E Fàbregas. Determination of β-HCG using amperometric immunosensors based on a conducting immunocomposite. *Analytica Chimica Acta*, 396(2–3):181–188, 1999. ISSN 0003-2670. doi: 10.1016/S0003-2670(99)00436-5.

[78] Donghui Yu, Bertrand Blankert, Ede Bodoki, Soledad Bollo, Jean-Claude Viré, R. Sandulescu, Akira Nomura, and Jean-Michel Kauffmann. Amperometric biosensor based on horseradish peroxidase-immobilised magnetic microparticles. *Sensors and Actuators B: Chemical*, 113(2):749–754, 2006. ISSN 0925-4005. doi: 10.1016/j.snb.2005.07.026.

[79] Angelika Kueng, Christine Kranz, and Boris Mizaikoff. Amperometric ATP biosensor based on polymer entrapped enzymes. *Biosensors and Bioelectronics*, 19(10): 1301–1307, 2004. ISSN 0956-5663. doi: 10.1016/j.bios.2003.11.023.

[80] D. C. Cullen, R. S. Sethi, and C. R. Lowe. Multi-analyte miniature conductance biosensor. *Analytica Chimica Acta*, 231:33–40, 1990. ISSN 0003-2670. doi: 10.1016/S0003-2670(00)86394-1.

[81] Kaoru Yagiuda, Akihide Hemmi, Satoshi Ito, Yasukazu Asano, Yoshito Fushinuki, Chien-Yuan Chen, and Isao Karube. Development of a conductivity-based immunosensor for sensitive detection of methamphetamine (stimulant drug) in human urine. *Biosensors and Bioelectronics*, 11(8):703–707, 1996. ISSN 0956-5663. doi: 10.1016/0956-5663(96)85920-3.

[82] Celine Chouteau, Sergei Dzyadevych, Jean-Marc Chovelon, and Claude Durrieu. Development of novel conductometric biosensors based on immobilised whole cell Chlorella vulgaris microalgae. *Biosensors and Bioelectronics*, 19(9):1089–1096, 2004. ISSN 0956-5663. doi: 10.1016/j.bios.2003.10.012.

[83] Anja Boisen, Søren Dohn, Stephan Sylvest Keller, Silvan Schmid, and Maria Tenje. Cantilever-like micromechanical sensors. *Reports on Progress in Physics*, 74(3): 036101, 2011. ISSN 0034-4885. doi: 10.1088/0034-4885/74/3/036101.

[84] A. Gupta, D. Akin, and R. Bashir. Single virus particle mass detection using microresonators with nanoscale thickness. *Applied Physics Letters*, 84(11):1976–1978, 2004. ISSN 0003-6951, 1077-3118. doi: 10.1063/1.1667011.

[85] Angelica P. Davila, Jaesung Jang, Amit K. Gupta, Tom Walter, Arthur Aronson, and Rashid Bashir. Microresonator mass sensors for detection of Bacillus anthracis Sterne spores in air and water. *Biosensors and Bioelectronics*, 22(12):3028–3035, 2007. ISSN 0956-5663. doi: 10.1016/j.bios.2007.01.012.

[86] H. P Lang, M. K Baller, R Berger, Ch Gerber, J. K Gimzewski, F. M Battiston, P Fornaro, J. P Ramseyer, E Meyer, and H. J Güntherodt. An artificial nose based on a micromechanical cantilever array. *Analytica Chimica Acta*, 393(1–3):59–65, 1999. ISSN 0003-2670. doi: 10.1016/S0003-2670(99)00283-4.

[87] Si-Hyung "Shawn" Lim, Digvijay Raorane, Srinath Satyanarayana, and Arunava Majumdar. Nano-chemo-mechanical sensor array platform for high-throughput chemical analysis. *Sensors and Actuators B: Chemical*, 119(2):466–474, 2006. ISSN 0925-4005. doi: 10.1016/j.snb.2006.01.032.

[88] Maria Nordström, Dan A. Zauner, Montserrat Calleja, Jörg Hübner, and Anja Boisen. Integrated optical readout for miniaturization of cantilever-based sensor system. *Applied Physics Letters*, 91(10):103512, 2007. ISSN 0003-6951, 1077-3118. doi: 10.1063/1.2779851.

[89] E. Forsen, G. Abadal, S. Ghatnekar-Nilsson, J. Teva, J. Verd, R. Sandberg, W. Svendsen, F. Perez-Murano, J. Esteve, E. Figueras, F. Campabadal, L. Montelius, N. Barniol, and A. Boisen. Ultrasensitive mass sensor fully integrated with complementary metal-oxide-semiconductor circuitry. *Applied Physics Letters*, 87 (4):043507, 2005. ISSN 0003-6951, 1077-3118. doi: 10.1063/1.1999838.

[90] María Villarroya, Jaume Verd, Jordi Teva, Gabriel Abadal, Esko Forsen, Francesc Pérez Murano, Arantxa Uranga, Eduard Figueras, Josep Montserrat, Jaume Esteve, Anja Boisen, and Núria Barniol. System on chip mass sensor based

on polysilicon cantilevers arrays for multiple detection. *Sensors and Actuators A: Physical*, 132(1):154–164, 2006. ISSN 0924-4247. doi: 10.1016/j.sna.2006.04.002.

[91] S. Ghatnekar-Nilsson, I. Karlsson, A. Kvennefors, G. Luo, V. Zela, M. Arlelid, T. Parker, L. Montelius, and A. Litwin. A new multifunctional platform based on high aspect ratio interdigitated NEMS structures. *Nanotechnology*, 20(17):175502, 2009. ISSN 0957-4484. doi: 10.1088/0957-4484/20/17/175502.

[92] Byung Hak Cha, Sang-Myung Lee, Jae Chan Park, Kyo Seon Hwang, Sang Kyung Kim, Yoon-Sik Lee, Byeong-Kwon Ju, and Tae Song Kim. Detection of Hepatitis B Virus (HBV) DNA at femtomolar concentrations using a silica nanoparticle-enhanced microcantilever sensor. *Biosensors and Bioelectronics*, 25(1):130–135, 2009. ISSN 0956-5663. doi: 10.1016/j.bios.2009.06.015.

[93] A. N. Cleland, M. Pophristic, and I. Ferguson. Single-crystal aluminum nitride nanomechanical resonators. *Applied Physics Letters*, 79(13):2070–2072, 2001. ISSN 0003-6951, 1077-3118. doi: 10.1063/1.1396633.

[94] Sen Xu and Raj Mutharasan. Rapid and Sensitive Detection of Giardia lamblia Using a Piezoelectric Cantilever Biosensor in Finished and Source Waters. *Environmental Science & Technology*, 44(5):1736–1741, 2010. ISSN 0013-936X. doi: 10.1021/es9033843.

[95] Seonghwan Kim, Touhidur Rahman, Larry R. Senesac, Brian H. Davison, and Thomas Thundat. Piezoresistive cantilever array sensor for consolidated bioprocess monitoring. *Scanning*, 31(5):204–210, 2009. ISSN 1932-8745. doi: 10.1002/sca.20159.

[96] Haitao Yu, Xinxin Li, Xiaohua Gan, Yongjing Liu, Xiang Liu, Pengcheng Xu, Jungang Li, and Min Liu. Resonant-cantilever bio/chemical sensors with an integrated heater for both resonance exciting optimization and sensing repeatability enhancement. *Journal of Micromechanics and Microengineering*, 19(4):045023, 2009. ISSN 0960-1317. doi: 10.1088/0960-1317/19/4/045023.

[97] A Hierlemann, D Lange, C Hagleitner, N Kerness, A Koll, O Brand, and H Baltes. Application-specific sensor systems based on CMOS chemical microsensors. *Sensors and Actuators B: Chemical*, 70(1–3):2–11, 2000. ISSN 0925-4005. doi: 10.1016/S0925-4005(00)00546-3.

[98] Margarita Narducci, Eduard Figueras, María José Lopez, Isabel Gràcia, Joaquin Santander, Peter Ivanov, Luis Fonseca, and Carles Cané. Sensitivity improvement of a microcantilever based mass sensor. *Microelectronic Engineering*, 86(4–6): 1187–1189, 2009. ISSN 0167-9317. doi: 10.1016/j.mee.2009.01.022.

[99] O. A. Sadik, H. Xu, E. Gheorghiu, D. Andreescu, C. Balut, M. Gheorghiu, and D. Bratu. Differential Impedance Spectroscopy for Monitoring Protein Immobilization and Antibody Antigen Reactions. *Analytical Chemistry*, 74(13):3142–3150, 2002. ISSN 0003-2700. doi: 10.1021/ac0156722.

[100] S. M. Radke and E. C. Alocilja. Design and fabrication of a microimpedance biosensor for bacterial detection. *IEEE Sensors Journal*, 4(4):434–440, 2004. ISSN 1530-437X. doi: 10.1109/JSEN.2004.830300.

[101] Junya Suehiro, Akio Ohtsubo, Tetsuji Hatano, and Masanori Hara. Selective detection of bacteria by a dielectrophoretic impedance measurement method using an antibody-immobilized electrode chip. *Sensors and Actuators B: Chemical*, 119 (1):319–326, 2006. ISSN 0925-4005. doi: 10.1016/j.snb.2005.12.027.

[102] Manu Sebastian Mannoor, Teena James, Dentcho V. Ivanov, Les Beadling, and William Braunlin. Nanogap Dielectric Spectroscopy for Aptamer-Based Protein Detection. *Biophysical Journal*, 98(4):724–732, 2010. ISSN 0006-3495. doi: 10.1016/j.bpj.2009.10.042.

[103] R. Dev Das, A. Dey, S. Das, and C. RoyChaudhuri. Interdigitated Electrode-Less High-Performance Macroporous Silicon Structure as Impedance Biosensor for Bacteria Detection. *IEEE Sensors Journal*, 11(5):1242–1252, 2011. ISSN 1530-437X. doi: 10.1109/JSEN.2010.2087746.

[104] Xiaohui Tang, Denis Flandre, Jean-Pierre Raskin, Yannick Nizet, Luis Moreno-Hagelsieb, Rémi Pampin, and Laurent A. Francis. A new interdigitated array microelectrode-oxide-silicon sensor with label-free, high sensitivity and specificity for fast bacteria detection. *Sensors and Actuators B: Chemical*, 156(2):578–587, 2011. ISSN 0925-4005. doi: 10.1016/j.snb.2011.02.002.

[105] Shibajyoti Ghosh Dastider, Syed Barizuddin, Majed Dweik, and Mahmoud Almasri. A micromachined impedance biosensor for accurate and rapid detection of

E. coli O157:H7. *RSC Advances*, 3(48):26297–26306, 2013. ISSN 2046-2069. doi: 10.1039/C3RA44724C.

[106] Shibajyoti Ghosh Dastider, Syed Barizuddin, Nuh S. Yuksek, Majed Dweik, and Mahmoud F. Almasri. Efficient and Rapid Detection of Salmonella Using Microfluidic Impedance Based Sensing. *Journal of Sensors*, 2015:e293461, 2015. ISSN 1687-725X. doi: 10.1155/2015/293461.

[107] Chathurika D. Abeyrathne, Duc H. Huynh, Thomas W. Mcintire, Thanh C. Nguyen, Babak Nasr, Daniela Zantomio, Gursharan Chana, Iain Abbott, Peter Choong, Mike Catton, and Efstratios Skafidas. Lab on a chip sensor for rapid detection and antibiotic resistance determination of Staphylococcus aureus. *Analyst*, 141(6):1922–1929, 2016. ISSN 1364-5528. doi: 10.1039/C5AN02301G.

[108] G. D. Alley. Interdigital Capacitors and Their Application to Lumped-Element Microwave Integrated Circuits. *IEEE Transactions on Microwave Theory and Techniques*, 18(12):1028–1033, 1970. ISSN 0018-9480. doi: 10.1109/TMTT.1970.1127407.

[109] A. V. Mamishev, K. Sundara-Rajan, Fumin Yang, Yanqing Du, and M. Zahn. Interdigital sensors and transducers. *Proceedings of the IEEE*, 92(5):808–845, 2004. ISSN 0018-9219. doi: 10.1109/JPROC.2004.826603.

[110] Zong-Hong Lin, Gang Cheng, Xiuhan Li, Po-Kang Yang, Xiaonan Wen, and Zhong Lin Wang. A multi-layered interdigitative-electrodes-based triboelectric nanogenerator for harvesting hydropower. *Nano Energy*, 15:256–265, 2015.

[111] Kwi-Il Park, Jung Hwan Son, Geon-Tae Hwang, Chang Kyu Jeong, Jungho Ryu, Min Koo, Insung Choi, Seung Hyun Lee, Myunghwan Byun, Zhong Lin Wang, and Keon Jae Lee. Highly-Efficient, Flexible Piezoelectric PZT Thin Film Nanogenerator on Plastic Substrates. *Advanced Materials*, 26(16):2514–2520, 2014. ISSN 1521-4095. doi: 10.1002/adma.201305659.

[112] Soon-Hyung Kwon, Junwoo Park, Won Keun Kim, YoungJun Yang, Eungkyu Lee, Chul Jong Han, Si Yun Park, Jeongno Lee, and Youn Sang Kim. An effective energy harvesting method from a natural water motion active transducer. *Energy & Environmental Science*, 7(10):3279–3283, 2014.

[113] R. Esfandiari, D. W. Maki, and M. Siracusa. Design of Interdigitated Capacitors and Their Application to Gallium Arsenide Monolithic Filters. *IEEE Transactions on Microwave Theory and Techniques*, 31(1):57–64, 1983. ISSN 0018-9480. doi: 10.1109/TMTT.1983.1131429.

[114] S. S. Gevorgian, T. Martinsson, P. L. J. Linner, and E. L. Kollberg. CAD models for multilayered substrate interdigital capacitors. *IEEE Transactions on Microwave Theory and Techniques*, 44(6):896–904, 1996. ISSN 0018-9480. doi: 10.1109/22.506449.

[115] Chieh Chang, Van H. Tran, Junbo Wang, Yiin-Kuen Fuh, and Liwei Lin. Direct-Write Piezoelectric Polymeric Nanogenerator with High Energy Conversion Efficiency. *Nano Letters*, 10(2):726–731, feb 2010.

[116] Jixue Lei, Bing Yin, Yu Qiu, Heqiu Zhang, Yue Chang, Yingmin Luo, Yu Zhao, Jiuyu Ji, and Lizhong Hu. Flexible piezoelectric nanogenerator based on Cu2o–ZnO p–n junction for energy harvesting. *RSC Advances*, 5(73):59458–59462, jul 2015.

[117] Saqib Siddiqui, Do-Il Kim, Le Thai Duy, Minh Triet Nguyen, Shoaib Muhammad, Won-Sub Yoon, and Nae-Eung Lee. High-performance flexible lead-free nanocomposite piezoelectric nanogenerator for biomechanical energy harvesting and storage. *Nano Energy*, 15:177–185, jul 2015.

[118] Yanchao Mao, Ping Zhao, Geoffrey McConohy, Hao Yang, Yexiang Tong, and Xudong Wang. Sponge-Like Piezoelectric Polymer Films for Scalable and Integratable Nanogenerators and Self-Powered Electronic Systems. *Advanced Energy Materials*, 4(7), may 2014.

[119] Hulin Zhang, Ya Yang, Yuanjie Su, Jun Chen, Katherine Adams, Sangmin Lee, Chenguo Hu, and Zhong Lin Wang. Triboelectric Nanogenerator for Harvesting Vibration Energy in Full Space and as Self-Powered Acceleration Sensor. *Advanced Functional Materials*, 24(10):1401–1407, mar 2014.

[120] Zong-Hong Lin, Gang Cheng, Long Lin, Sangmin Lee, and Zhong Lin Wang. Water–Solid Surface Contact Electrification and its Use for Harvesting Liquid-Wave Energy. *Angewandte Chemie International Edition*, 52(48):12545–12549, nov 2013.

[121] G. Despesse, J. J. Chaillout, T. Jager, J. M. Léger, A. Vassilev, S. Basrour, and B. Charlot. High Damping Electrostatic System for Vibration Energy Scavenging. In *Proceedings of the 2005 Joint Conference on Smart Objects and Ambient Intelligence: Innovative Context-aware Services: Usages and Technologies*, sOc-EUSAI '05, pages 283–286, New York, NY, USA, 2005. ACM.

[122] Zhong Lin Wang, Jun Chen, and Long Lin. Progress in triboelectric nanogenerators as a new energy technology and self-powered sensors. *Energy & Environmental Science*, 8(8):2250–2282, 2015.

[123] Tom Krupenkin and J. Ashley Taylor. Reverse electrowetting as a new approach to high-power energy harvesting. *Nature Communications*, 2:448, August 2011.

[124] Chathurika D. Abeyrathne, Malka N. Halgamuge, Peter M. Farrell, and Efstratios Skafidas. Dielectric properties of liquid phase molecular clusters using the external field method: molecular dynamics study. *Physical Chemistry Chemical Physics*, 16(27):13943–13947, June 2014.

[125] H. Helmholtz. Ueber einige Gesetze der Vertheilung elektrischer Ströme in körperlichen Leitern mit Anwendung auf die thierisch-elektrischen Versuche. *Annalen der Physik*, 165(6):211–233, January 1853.

[126] A. M. More, J. L. Gunjakar, C. D. Lokhande, and Oh Shim Joo. Fabrication of hydrophobic surface of titanium dioxide films by successive ionic layer adsorption and reaction (SILAR) method. *Applied Surface Science*, 255(12):6067–6072, 2009.

[127] Jong Kyun Moon, Jaeki Jeong, Dongyun Lee, and Hyuk Kyu Pak. Electrical power generation by mechanically modulating electrical double layers. *Nature Communications*, 4:1487, February 2013.

[128] Zong-Hong Lin, Gang Cheng, Sangmin Lee, Ken C. Pradel, and Zhong Lin Wang. Harvesting Water Drop Energy by a Sequential Contact-Electrification and Electrostatic-Induction Process. *Advanced Materials*, 26(27):4690–4696, July 2014.

[129] Xiaoliang Cheng, Bo Meng, Mengdi Han, Haotian Chen, and Haixia Zhang. A high-efficiency transparent electrification-based generator for harvesting droplet energy. In *2015 Transducers - 2015 18th International Conference on Solid-State Sensors, Actuators and Microsystems (TRANSDUCERS)*, pages 62–65, 2015.

[130] Wei Ma, Ruiqing Zhu, L. Rufer, Y. Zohar, and Man Wong. An Integrated Floating-Electrode Electric Microgenerator. *Journal of Microelectromechanical Systems*, 16 (1):29–37, February 2007.

[131] Yuji Suzuki, Masato Edamoto, Nobuhide Kasagi, K Kashwagi, and Yoshitomi Morizawa. Micro electret energy harvesting device with analogue impedance conversion circuit. *Proc. PowerMEMS*, 8:7–10, 2008.

[132] Joon S. Shim, Michael J. Rust, and Chong H. Ahn. A large area nano-gap interdigitated electrode array on a polymer substrate as a disposable nano-biosensor. *Journal of Micromechanics and Microengineering*, 23(3):035002, March 2013. ISSN 0960-1317.

[133] Wen-Di Li, Wei Wu, and Richard Stanley Williams. Combined helium ion beam and nanoimprint lithography attains 4 nm half-pitch dense patterns. *Journal of Vacuum Science & Technology B*, 30(6):06F304, November 2012.

[134] Masashi Miwa, Akira Nakajima, Akira Fujishima, Kazuhito Hashimoto, and Toshiya Watanabe. Effects of the Surface Roughness on Sliding Angles of Water Droplets on Superhydrophobic Surfaces. *Langmuir*, 16(13):5754–5760, June 2000.

[135] Zen Yoshimitsu, Akira Nakajima, Toshiya Watanabe, and Kazuhito Hashimoto. Effects of Surface Structure on the Hydrophobicity and Sliding Behavior of Water Droplets. *Langmuir*, 18(15):5818–5822, July 2002.

[136] T. Brommeland, L. Rosengren, S. Fridlund, R. Hennig, and V. Isaksen. Serum levels of glial fibrillary acidic protein correlate to tumour volume of high-grade gliomas. *Acta Neurologica Scandinavica*, 116(6):380–384, 2007. ISSN 1600-0404.

[137] Erwin Van Meir, Yutaka Sawamura, Annie-Claire Diserens, Marie-France Hamou, and Nicolas de Tribolet. Human Glioblastoma Cells Release Interleukin 6 in Vivo and in Vitro. *Cancer Research*, 50(20):6683–6688, October 1990. ISSN 0008-5472, 1538-7445.

[138] Zhiqun Zhang, J. Susie Zoltewicz, Stefania Mondello, Kimberly J. Newsom, Zhihui Yang, Boxuan Yang, Firas Kobeissy, Joy Guingab, Olena Glushakova, Steven Robicsek, Shelley Heaton, Andras Buki, Julia Hannay, Mark S. Gold, Richard

Rubenstein, Xi-chun May Lu, Jitendra R. Dave, Kara Schmid, Frank Tortella, Claudia S. Robertson, and Kevin K. W. Wang. Human Traumatic Brain Injury Induces Autoantibody Response against Glial Fibrillary Acidic Protein and Its Breakdown Products. *PLOS ONE*, 9(3):e92698, 2014. ISSN 1932-6203. doi: 10.1371/journal.pone.0092698.

[139] C. D. Abeyrathne, M. N. Halgamuge, P. M. Farrell, and E. Skafidas. On the Utility of Dielectric Spectroscopy Techniques to Identify Compounds and Estimate Concentrations of Binary Mixtures. *IEEE Sensors Journal*, 14(2):538–546, 2014. ISSN 1530-437X. doi: 10.1109/JSEN.2013.2285279.

[140] C. D. Abeyrathne and E. Skafidas. Complex Permittivity Measurements in 1 #x2013;30 GHz Using a MEMS Probe. *Journal of Microelectromechanical Systems*, 24(4):976–981, 2015. ISSN 1057-7157. doi: 10.1109/JMEMS.2014.2360914.

[141] Chathurika D. Abeyrathne, Malka N. Halgamuge, Peter M. Farrell, and Efstratios Skafidas. Comparison of corrected calibration independent transmission coefficient method to estimate complex permittivity. *Sensors and Actuators A: Physical*, 189: 466–473, January 2013. ISSN 0924-4247. doi: 10.1016/j.sna.2012.10.019.

[142] C. D. Abeyrathne, M. N. Halgamuge, P. M. Farrell, and E. Skafidas. Performance Analysis of On-Chip Coplanar Waveguide for In Vivo Dielectric Analysis. *IEEE Transactions on Instrumentation and Measurement*, 62(3):641–647, 2013. ISSN 0018-9456. doi: 10.1109/TIM.2012.2218672.

[143] Hongming Liu, Yadong Yang, Ping Chen, and Zhaoyang Zhong. Enhanced conductometric immunoassay for hepatitis B surface antigen using double-codified nanogold particles as labels. *Biochemical Engineering Journal*, 45(2):107–112, 2009. ISSN 1369-703X. doi: 10.1016/j.bej.2009.03.002.

[144] P. Sanguino, T. Monteiro, F. Marques, C. J. Dias, R. Igreja, and R. Franco. Interdigitated Capacitive Immunosensors With PVDF Immobilization Layers. *IEEE Sensors Journal*, 14(4):1260–1265, 2014. ISSN 1530-437X. doi: 10.1109/JSEN.2013.2294435.

[145] C. W. Huang and M. S. C. Lu. Electrochemical Detection of the Neurotransmitter Dopamine by Nanoimprinted Interdigitated Electrodes and a CMOS Circuit With

Enhanced Collection Efficiency. *IEEE Sensors Journal*, 11(9):1826–1831, 2011. ISSN 1530-437X. doi: 10.1109/JSEN.2011.2105260.

[146] Kallempudi S. Saravan, Ozgur Gul, Huveyda Basaga, Ugur Sezerman, and Yasar Gurbuz. Label-Free Biosensors for the Detection and Quantification of Cardiovascular Risk Markers. *Sensor Letters*, 6(6):873–877, 2008. doi: 10.1166/sl.2008.521.

[147] Zeynep Altintas, Sreenivasa Saravan Kallempudi, and Yasar Gurbuz. Gold nanoparticle modified capacitive sensor platform for multiple marker detection. *Talanta*, 118:270–276, 2014. ISSN 0039-9140. doi: 10.1016/j.talanta.2013.10.030.

[148] Anjum Quershi, Yasar Gurbuz, Weng P. Kang, and Jimmy L. Davidson. A novel interdigitated capacitor based biosensor for detection of cardiovascular risk marker. *Biosensors and Bioelectronics*, 25(4):877–882, 2009. ISSN 0956-5663. doi: 10.1016/j.bios.2009.08.043.

[149] Chonlatid Sontimuang, Roongnapa Suedee, and Franz Dickert. Interdigitated capacitive biosensor based on molecularly imprinted polymer for rapid detection of Hev b1 latex allergen. *Analytical Biochemistry*, 410(2):224–233, 2011. ISSN 0003-2697. doi: 10.1016/j.ab.2010.11.043.

[150] Ha-Wook Jung, Young Wook Chang, Ga-yeon Lee, Sungbo Cho, Min-Jung Kang, and Jae-Chul Pyun. A capacitive biosensor based on an interdigitated electrode with nanoislands. *Analytica Chimica Acta*, 844:27–34, 2014. ISSN 0003-2670. doi: 10.1016/j.aca.2014.07.006.

[151] Shanshan Li, Haochen Cui, Quan Yuan, Jie Wu, Ashutosh Wadhwa, Shigetoshi Eda, and Hongyuan Jiang. AC electrokinetics-enhanced capacitive immunosensor for point-of-care serodiagnosis of infectious diseases. *Biosensors and Bioelectronics*, 51:437–443, 2014. ISSN 0956-5663. doi: 10.1016/j.bios.2013.08.016.

[152] Yi Wang, Wei Wang, Lina Yu, Liang Tu, Yinglong Feng, Todd Klein, and Jian-Ping Wang. Giant magnetoresistive-based biosensing probe station system for multiplex protein assays. *Biosensors and Bioelectronics*, 70:61–68, 2015. ISSN 0956-5663. doi: 10.1016/j.bios.2015.03.011.

[153] M. Naghed and I. Wolff. Equivalent capacitances of coplanar waveguide discontinuities and interdigitated capacitors using a three-dimensional finite difference

method. *IEEE Transactions on Microwave Theory and Techniques*, 38(12):1808–1815, 1990. ISSN 0018-9480. doi: 10.1109/22.64560.

[154] Gusta Trillo-Pazos, Elizabeth McFarlane-Abdulla, Iain C Campbell, Geoffrey J Pilkington, and Ian P Everall. Recombinant nef HIV-IIIB protein is toxic to human neurons in culture. *Brain Research*, 864(2):315–326, 2000. ISSN 0006-8993. doi: 10.1016/S0006-8993(00)02213-7.

[155] Babak Nasr, Gursharan Chana, Ting Ting Lee, Thanh Nguyen, Chathurika Abeyrathne, Giovanna M. D'Abaco, Mirella Dottori, and Efstratios Skafidas. Vertical Nanowire Electrode Arrays as Novel Electrochemical Label-Free Immunosensors. *Small*, 11(24):2862–2868, 2015. ISSN 1613-6829. doi: 10.1002/smll.201403540.

[156] David M.Pozar. *Microwave engineering.* John Wiley and Sons, 2009.

[157] E. Usdin and I. Hanin. *Biological Markers in Psychiatry and Neurology.* 1st ed. Oxford, U.K.: Pergamon, 1982.

[158] H. Kettenmann and B. R. Ransom. *Neuroglia.* 2nd ed. Oxford,U.K.: Oxford Univ. Press, 2005.

Author/s:
HUYNH, DUC HAU

Title:
Novel applications of static micro-scale interdigitated electrodes for energy harvesting and biosensing

Date:
2016

Persistent Link:
http://hdl.handle.net/11343/129170

File Description:
Novel Applications of Static Micro-Scale Interdigitated Electrodes for Energy Harvesting and Biosensing